SINGLE AND DOUBLE DROP IMPACTS ONTO DEEP AND THICK LIQUID LAYERS

ALFIO BISIGHINI

Thesis submitted for the degree of Doctor of Philosophy

Dottorato di ricerca in Tecnologie per l'Energia e l'Ambiente
Dipartimento di Ingegneria Industriale
Facoltà di Ingegneria
Università degli Studi di Bergamo

December 2009

Alfio Bisighini: *Single and double drop impacts onto deep and thick liquid layers,* PhD thesis, © December 2009

SUPERVISORS:
Prof. Gianpietro Elvio Cossali
Dr.-Ing. Ilia Roisman

LOCATION:
Bergamo

TIME FRAME:
December 2009

To my family.

Gutta cavat lapidem

— Ovidio, Epistulae ex Ponto, IV, 10, 5.

ABSTRACT

The present experimental and analytical study deals with single and double drop impacts onto a deep pool or liquid layers of finite thickness, with a general purpose of understanding the complex flows generated by spray impacts. The study is focused mainly on the observation of the evolution of the crater formed by the drop impacts and the description of the associated flow in the liquid layer.

A test rig for the high-speed-visualization of interface phenomena has been built and experimental investigations using high-speed-imaging and image processing have been performed.

Single drop impacts onto a deep pool have been studied in relation with the extensive existing literature. A new classification of the flow regimes has been suggested and a new "trampoline" regime has been detected and described. The phenomenon of the closure of the crown above the crater, typical of terminal speed impacts, has been obtained with unprecedented low impact parameters and it has been observed to be promoted by the sphericity of the impacting drop, while it does not take place if the drop is oblate.

A phenomenological investigation of double drop impacts onto a deep pool has been for the first time performed. The phenomena arising have been observed to be characterized by several interactions, which have been described and discussed. The two craters and the two jets ejected from the craters may merge each other. New complex hollow shapes of the crater or of the jet resulting from the merging may be produced and a new mechanism of bubble entrapment has been detected. A test case for the validation of numerical codes has also been proposed, since the simultaneous impact of two identical drops represents a new example of three dimensional free surface flow, instead of the axial symmetry typical of a single drop impact.

The influence of a finite value of the depth of the target liquid layer has been investigated in comparison with single drop impacts onto a deep pool, with particular attention on the crater evolution. The presence of the wall has been observed to reduce the velocity of penetration of the crater, but to do not significatively change its maximum depth, which is only reached later. For this reason the maximum crater depth of a deep pool impact has been chosen as reference parameter for the usual classification in thin films, thick films and deep pools of the depth of the

target liquid layers in relation with the parameters of the impacting drop. This choice has a more physical significance, since it accounts for the kinetic energy of the impacting drop instead of only its diameter.

The crater formed by the impact of a drop onto a deep pool has been characterized for several impact parameters. A new theoretical model for its evolution has been formulated. Potential flow theory has been used to model the flow around the crater as the velocity field given by a moving expanding sphere, whose equations of motion have been obtained through a balance of stresses at the crater interface and include the effects of inertia, gravity, surface tension and viscosity. Agreement with experimental data from the present study and from literature is rather good. A map of the predicted values of the maximum crater depth as a function of the impact parameters has been produced.

ACKNOWLEDGMENTS

I wish to express my sincere gratitude to prof. Gianpietro Elvio Cossali and to dr.-ing. Ilia Roisman for their great support during the development of the present study. A particular acknowledgement to prof. Cameron Tropea for his hospitality at Fachgebiet Strömungslehre und Aerodynamik of the Technische Universität Darmstadt. A special thank also to dr.-ing. Maurizio Santini, who introduced me to the high-speed-visualization of drop impacts.

CONTENTS

LIST OF FIGURES

LIST OF TABLES

1 INTRODUCTION

Subject

The present experimental and analytical study deals with single and double drop impacts onto a deep pool or a liquid layer of finite thickness, with a general purpose of understanding the complex flows generated by spray impacts. The study is focused mainly on the observation of the evolution of the crater formed by the drop impacts (see Figure 1) and the description of the associated flow in the liquid layer.

Research area

In an engineering frame, spray technologies have a high industrial significance and have attracted the attention of modelers in an effort to increase efficiencies and performances by predicting the outcome. However the present state-of-the-art of the modeling of spray impacts is still in an embryonal state, since the physics is not completely understood and no reliable tools have been yet developed able to predict typical film thickness, typical flow in the liquid layer, typical parameters of the secondary spray, etc.

Spray impact onto a wall with formation of a liquid film

When a spray impacts onto a rigid target it produces a liquid film, onto which the other drops impact. The wide diameter distribution of the drops forming a spray implies a wide distribution of the ratio between the film thickness and the various drop diameters, meaning a great or attenuate effect of the wall on the impact phenomena.

Research approach

Due to the rather high complexity of the physical mechanism involved and to the great number of drops forming a spray, Figure 2a, the path through a better understanding of the implied

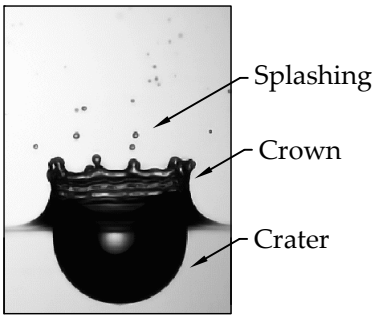

Figure 1: Drop impact onto a deep pool with formation of a crater below the target surface and a wave with a shape similar to a crown above the target surface. The term "splashing" refers to the formation of secondary droplets.

phenomena has first to start from the study of a single drop impact onto a dry surface, (b), onto a thick film, (c), and onto a deep pool (a film with a depth sufficiently high that the impact is not influenced by the bottom wall), (d). Then, since the impact of a spray can hardly be modeled as a simple superposition of single drop impacts, the study of double (or multiple) drop impacts, (e), is a necessary second step to a proper extrapolation of the results to a real case.

Motivation

While most of the existing related literature deals with the splashing phenomena of single drop impacts or impingements of polydisperse sprays, the submerged part of the impacts, i. e. the the evolution of the crater (see Figure 1), have been still not fully investigated, despite of its importance. In fact, it influences both the over and under surface phenomena, the film dynamics and also the convective heat transfer in case of non isothermal impacts. In addition, the present work is aimed to fill the gap in the literature about the study of double drop impacts onto a deep pool.

Methods

Experimental investigations have been performed on single and double drop impacts onto deep pools and onto thick films, using high speed imaging and image processing. For this purpose, a test rig has been built and a procedure to record high speed images of the impacts has been developed. A new theoretical model for the evolution of the crater formed by the impact of a drop onto a deep pool has been formulated and validated against the experimental data, showing a rather good agreement.

Places

Data have been collected at the University of Bergamo (Italy) and partially processed and analyzed at the Technische Universität Darmstadt (Germany) during a visiting period of eight months, in which the theoretical model has also been developed. The choice of the team from TUD was motivated by their well-known activities in the fields of drop and spray impacts and in particular by their experience in theoretical modeling of the related phenomena.

1.1 HISTORICAL ORIGINS

The first studies on drop impacts were performed in the 19th century by Reynolds (1875, 1881), Thomson and Newall (1885), and Worthington (1883), an English physics professor who, regardless from technical applications, spent about 30 years, on the study of this subject, being the first to perform a systematic investigation. He initially used sketches instead of films to record his observation, but later, with the help of contemporaries Lord Rayleigh and industrial scientist C.V. Boys, he used powerful sparks from Leyden jars to create the necessary brief exposure

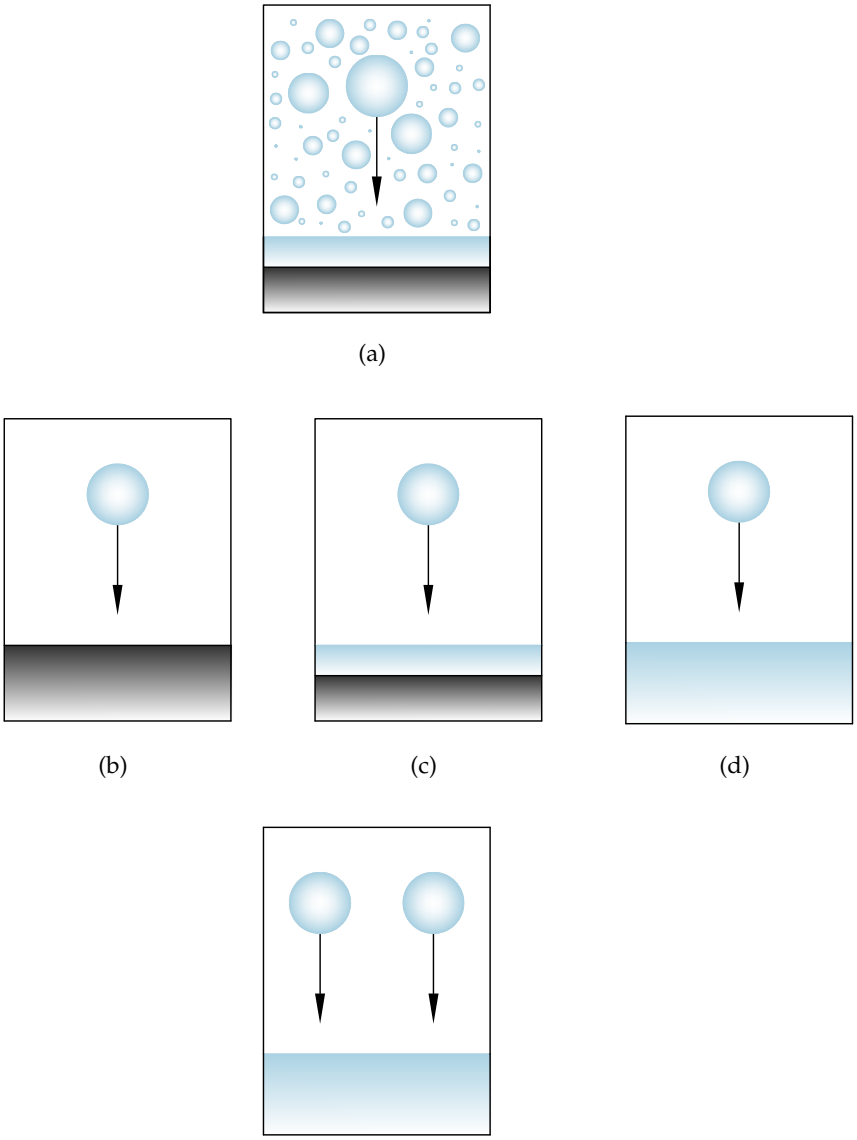

Figure 2: Sketches of spray and drop impacts. (a) Spray impact onto a wall. (b) Single drop impact onto a dry surface. (c) Single drop impact onto a liquid film of finite thickness. (d) Single drop impact onto a deep pool. (e) Double drop impact onto a deep pool.

time for the first high speed photographs. In 1894 his studies were presented in a lecture at the Royal Institution entitled "The splash of a drop and allied phenomena" and were reprinted in the "Romance of science" series by the Society for Promoting Christian Knowledge. The success of the lecture and of the first images shown at the end (taken with the help of his friend R.S. Cole), led to a long photographic investigation presented in two papers published in the Philosophical Transactions of the Royal Society of London (Worthington and Cole, 1897, 1900). To show his result to a more general public, two magazine articles were published on Pearson's magazine, which has also been notable as the first British periodical to publish a crossword puzzle, in February 1922. Later, in 1908 he published "A study of splashes" (Worthington, 1908), a book collecting all his unbelievable pictures that was also presented in an article of Nature (Boys, 1908) and of The New York Times 1908. The following excerpt from the introduction gives evidence of the enthusiasm of Worthington for his observations and of his wish to share them:

> *If the present volume is so fortunate as to find many readers among the general public, as the author hopes it may, especially among the young whose eyes are still quick to observe, and whose minds are eager, it will be on account of admiration for the exquisite beauty of some of the forms assumed, of surprise at the revelation of so much where so little was expected, and because of the peculiar fascination that is always felt in following any gradually changing natural phenomenon, in which the sequence of events can, partly at any rate, be anticipated and understood.*

There was no dependable way of looking to drop splashes before of Worthington age, so he absolutely is the pioneer in the field of drop impacts. After Worthington the person whose name is generally associated with photographs of splashes is Edgerton and Killian (1954), who has been a professor at MIT for 58 years and probably did more than anyone to popularize high-speed photography, which become widely used in fluid dynamic investigations. Phenomena of drop impacts have been widely investigated during all the last century, in connections with a wide range of technical applications, natural researches and academical studies.

1.2 APPLICATIONS

Technical applications

Phenomena of drop impacts are presently of interest because their relation to various engineering applications and industrial processes, particularly in the field of spray technologies, like

spray coating (Mehdi-Nejad et al., 2003), cooling and painting or in internal combustion engines with direct fuel injection (Sivakumar and Tropea, 2002), where the fuel is sprayed into engine cylinders in the form of small droplets, which splash on the inner walls of the cylinders, possibly creating a liquid film. Other field of interest are ink-jet printing, aircraft and wind turbine icing, electronic-component welding, anti-firing systems (Manzello and Yang, 2002), gas injection during metallurgical processes (Liow et al., 1994), polymer encapsulation processes (Deng et al., 2009), nebulizers for medical uses and many others.

Natural implications

Drop impacts have also a significant role in many natural processes including soil erosion by rain (Ellison, 1944, Ghadiri, 2004), transport of bacteria and dispersal of fungus spores (Fitt and Shaw, 1989), crater formed by meteorite impacts (Gault and Moore, 1965), surface renewals and wave damping by rainfall on the sea (Reynolds, 1875, Craeye and Schlussel, 1998), spread behavior of pesticides, atmospheric and oceanographic detection and characterization of rain over the oceans by remote acoustic sensors (Prosperetti and Oguz, 1993). Among all these natural phenomena in which drop impacts are involved, it is highlighted here the great number of way of air entrapment into the target liquid by drop impacts, with a great and large-scale relevance in aeration of the surface layers of lakes, seas, and oceans and implications that range from the trophism of planktonic organisms at the beginning of the food chain to the absorption of carbon dioxide CO_2 (Morton and Cresswell, 1992).

Academical relevance

The involvement of several physical mechanisms also makes it an attractive academic problem of fundamental fluid mechanical interest, since impacting drops provide an example of a unsteady free surface flow governed by inertial, gravitational, viscous and surface tension effects. The approaches that have been adopted to describe the complexity of this subject consist mainly on experiments and numerical simulations, while spare theoretical models appeared in literature, often based on energy balances. Understanding the accompanying physical phenomena is of utmost importance in providing test cases for the validation of numerical codes and in formulating reliable boundary conditions for spray simulations. Moreover, the developed methodologies, thanks to their generality, appear to be transferable to other application fields.

Other applications

Finally, two non strictly scientific fields are the criminal forensics, where the bloodstain pattern analysis (BPA) can be of significance in reconstructing crimes, and in artistic photography, where pictures of drop impacts like those in the portfolio of Martin Waugh can only cause amazement and are widely used in advertising.

Governing equations

If the temperature and the liquid of the impacting drop and of the target pool are equal, the flow of the target fluid resulting from the impact is only governed by the conservation of mass and momentum:

$$\rho_t + \nabla \cdot \rho \boldsymbol{u} = 0\,, \tag{1.1a}$$

$$\rho \boldsymbol{u}_t + \rho\,(\boldsymbol{u} \cdot \nabla)\,\boldsymbol{u} = \nabla \cdot \boldsymbol{T} + \rho \boldsymbol{f}\,, \tag{1.1b}$$

where t is the time, ρ is the density, $\boldsymbol{u}$ is the velocity field, $\boldsymbol{f}$ is a volume force and $\boldsymbol{T}$ is the stress tensor, which, for Newtonian fluids, can be expressed as:

$$\boldsymbol{T} = -p\boldsymbol{I} + \mu\left[\nabla \boldsymbol{u} + (\nabla \boldsymbol{u})^T\right] + \lambda \boldsymbol{I} \nabla \cdot \boldsymbol{u}\,, \tag{1.2}$$

where p is the pressure, $\boldsymbol{I}$ is the identity tensor, μ is the dynamic viscosity and λ the second viscosity. Using the Stokes assumption[1] ($\lambda + \frac{2}{3}\mu = 0$), Equation 1.1 reduce to the well known Navier-Stokes equations, which, for a incompressible flow where gravity $\boldsymbol{g}$ is the only volume force, may be written as:

$$\nabla \cdot \boldsymbol{u} = 0\,, \tag{1.3a}$$

$$\rho \boldsymbol{u}_t + \rho\,(\boldsymbol{u} \cdot \nabla)\,\boldsymbol{u} = -\nabla p + \mu \nabla^2 \boldsymbol{u} + \rho \boldsymbol{g}\,. \tag{1.3b}$$

Compressibility effects may have a role only in the very early stage of the drop impact and has been neglected in the present study.

Boundary conditions

At the liquid gas interface (Figure 3) the kinematic and the balance of stresses boundary conditions have to be satisfied. Neglecting evaporation:

$$\boldsymbol{u} \cdot \boldsymbol{n} = \boldsymbol{u}_s \cdot \boldsymbol{n}\,, \tag{1.4a}$$

$$\boldsymbol{n} \cdot \boldsymbol{T}_{gas} - \boldsymbol{n} \cdot \boldsymbol{T}_{liq} = \sigma \boldsymbol{n}\,(\nabla \cdot \boldsymbol{n}) - \nabla_s \sigma\,, \tag{1.4b}$$

where $\boldsymbol{n}$ is the unit vector normal to the interface and pointing outward, from the liquid to the gas phase, $\boldsymbol{u}_s$ is the velocity of the interface, σ is the surface tension and $\nabla \cdot \boldsymbol{n} = \kappa$ is the curvature of the interface. Since viscosity of the gas phase is in general almost one hundred times lower than viscosity of the liquid phase, the first addend in the *rhs* of Equation 1.4 may be neglected if velocity gradients in the gas phase are not too high. In addition, since the gradient of the surface tension is usually related to a gradient of temperature (Marangoni stresses), the last term is null when temperature is constant. Thus boundary conditions on the free surface reduce to:

$$\boldsymbol{u} \cdot \boldsymbol{n} = \boldsymbol{u}_s \cdot \boldsymbol{n}\,, \tag{1.5a}$$

$$-\boldsymbol{n} \cdot \left(-p\boldsymbol{I} + \mu\left[\nabla \boldsymbol{u} + (\nabla \boldsymbol{u})^T\right]\right) = \alpha\,\kappa\,\boldsymbol{n}\,. \tag{1.5b}$$

1 The Stokes assumption would be unnecessary for incompressible flows.

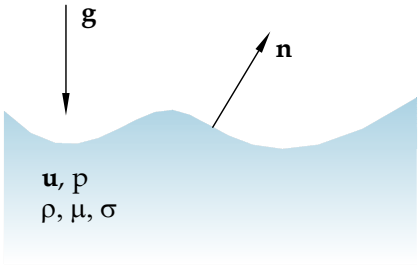

Figure 3: Free surface flow.

Equation 1.5a implies that the interface behaves like a material surface, since it is defined by the property that fluid does not cross it. Equation 1.5b implies a jump in the normal stresses against a curved interface due to surface tension and a null tangential component of the gradient of the velocity field.

Dimensional analysis

According to the Buckingham Π theorem, three dimensionless numbers allow a complete description of the problem. Taking the drop diameter[2] D as the reference length, the impact velocity V as the reference velocity (Figure 4) and the quantity ρV^2 as the reference for the reduced pressure $p_d = p - \rho g z$ (the axis z has the same direction and sense of the gravity field $\boldsymbol{g}$), Equation 1.3 and Equation 1.5 may be written as:

$$\nabla \cdot \tilde{\mathbf{u}} = 0\,, \tag{1.6a}$$

$$\tilde{\mathbf{u}}_\tau + (\tilde{\mathbf{u}} \cdot \nabla)\,\tilde{\mathbf{u}} + \nabla \tilde{p}_d - \frac{1}{Re}\Delta \tilde{\mathbf{u}} = 0\,, \tag{1.6b}$$

$$\tilde{\mathbf{u}} \cdot \mathbf{n} = \tilde{\mathbf{u}}_s \cdot \mathbf{n}\,, \tag{1.6c}$$

$$\tilde{p}_d + \frac{1}{Fr}\tilde{z} - \frac{1}{Re}\mathbf{n}\left[\nabla \tilde{\mathbf{u}} + (\nabla \tilde{\mathbf{u}})^T\right]\mathbf{n} = \frac{\kappa}{We}\,, \tag{1.6d}$$

where the tilde has been used to denote the new dimensionless unknowns,

$$\tau = \frac{tV}{D}\,, \tag{1.7}$$

is the dimensionless time and Re, Fr, We are the Reynolds, Froude and Weber numbers:

$$We = \frac{\rho V^2 D}{\sigma}\,, \tag{1.8a}$$

$$Fr = \frac{V^2}{gD}\,, \tag{1.8b}$$

$$Re = \frac{\rho V D}{\mu}\,, \tag{1.8c}$$

describing the ratio between the characteristics time of inertia, viscosity, gravity and capillary effects. Equation 1.6 can completely describe the flow arisen from the impact of a drop onto

2 Few authors, e.g. Elmore et al. (2001), have used the radius R instead of the diameter D as the characteristic length.

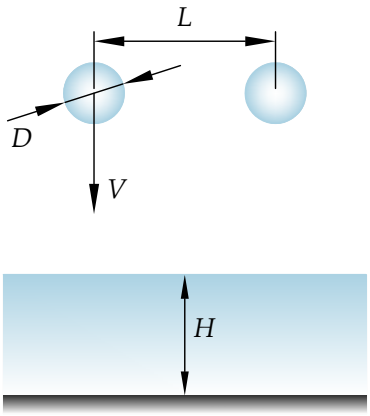

Figure 4: Dimensional impact parameters.

a semi-infinite liquid layer (the fluid may be assumed to be at rest at infinity). Reynolds, Weber and Froude numbers are the most chosen in literature, but some other dimensionless numbers, which can be obtained as a combination of them, like Bond, Capillary and Ohnesorge numbers, may also be useful:

$$Bo = \frac{We}{Fr} = \frac{\rho g D^2}{\sigma}, \tag{1.8d}$$

$$Ca = \frac{We}{Re} = \frac{\mu U}{\sigma}, \tag{1.8e}$$

$$Oh = \frac{\sqrt{We}}{Re} = \frac{\mu}{\sqrt{\rho D \sigma}}. \tag{1.8f}$$

Single drop impacts onto a deep pool

In the end, neglecting the influence of the surrounding air, only two parameters, in addition to the physical properties of the fluid (ρ, μ, σ), are needed to completely describe a spherical drop impacting vertically onto a semi-infinite target of the same liquid and temperature in normal gravity conditions, i. e. drop diameter D and impact velocity V, which all turns into three dimensionless numbers. Since direct solutions of Equation 1.6 have hardly ever be obtained (Yarin and Weiss, 1995, Roisman, 2009), dimensional analysis has been the main tool to describe the phenomena arising from the drop impacts.

Single drop impacts onto a thick film

If the target liquid is a thick layer instead of a deep pool, an additional parameter H is needed to define the depth (Figure 4), which is non-dimensionalized with the drop diameter:

$$\tilde{H} = \frac{H}{D}. \tag{1.9}$$

The liquid films are usually classified as:

DEEP POOLS: the depth is so greater that the impact is not influenced by the bottom wall.

THICK FILMS: the impact phenomena resents of the presence of the wall, but only few time after the impact. Sometimes this class is known as shallow pool.

THIN FILMS: the depth is so smaller that the impact phenomena are immediately strongly influenced by the pool bottom.

Obviously these distinctions are not well defined, but they are useful to put in order the wide survey from a morphological point of view. In the present study only impacts onto deep pools and thick films have been considered.

Double drop impacts onto a deep pool

For an impact of two drops the number of parameters needed to completely define the impact conditions would be more than double respect to a single impact, since in addition to those of each drop, other parameters are necessary to define the relative position in space and in time. However in the present study, as a first step, only the simultaneous impact of two identical drops at the same impact velocity is considered, thus the additional parameters to the drop diameter D, velocity V and film thickness H is the horizontal distance L of the two drops (Figure 4), which is considered between the two drop centers and is non-dimensionalized with the drop diameter:

$$\tilde{L} = \frac{L}{D}\,. \tag{1.10}$$

1.4 THESIS OUTLINE

Single and double drop impacts onto a deep pool and thick liquid films have been investigated by means of a digital high speed camera and image processing. Particular attention was paid to the crater and a theoretical model for its evolution has been formulated. The present thesis is articulated on the following sections:

- Chapter 2 explains the experimental setup, with a description of the components forming the test rig and the problems faced up during its development, a working-out of the procedure of image acquisition and an explanation of the main issues of image processing.
- Chapter 3 deals with single drop impacts onto a deep pool. A literary review is presented. A new classification of the impact regimes is proposed. Thanks to the experimental observations, new details have been added and a new impact regime has been detected and described.
- Chapter 4 illustrates a phenomenological investigation on double drop impacts onto a deep pool, with a comparison

with single drop impacts and a description of the similarities and of the new features observed.

- Chapter 5 reports an experimental investigation on the influence of the depth of the target liquid layer on the crater evolution. The usual classification of target films is analyzed and a new reference parameter is suggested.
- Chapter 6 presents the formulation of a theoretical model for the crater evolution and its validation against experimental data.
- Chapter 7 resumes the results of the present study, giving some suggestions on possible future works.

2

EXPERIMENTAL SETUP

Subject

The vertical impact of millimetric drops on liquid layers of the same liquid has been studied by means of a digital high-speed camera and image processing. Distilled water was mainly used as a working liquid and, in few cases, acetic acid. The impact velocity was varied by changing the falling height. All the experiments were performed under normal atmospheric and gravity conditions. Due to the high intensity illumination, the target fluid reached an equilibrium temperature of about 30 °C, at which physical properties have been used and reported in Table 1.

Experimental apparatus

An had-hoc experimental apparatus has been built, allowing enough flexibility to perform investigations on single or double impacts onto deep or thick layers and to record images from a lateral side, from below and from the intermediate angles. It may be divided into three main systems:

- drop generation;
- target pool;
- image acquisition.

Components, sketched in Figure 5, have been assembled on a test rig, built using ITEM and self-made components. A dripper (3), fed by a reservoir (4), generated one or two drops which fell onto a target pool (1), placed on a level platform. Particular care was taken to prevent dust deposition on the target liquid, whose container was connected to a level pool (2) mounted on a vertical micrometric stage. A vertical movable platform might be immersed in the target pool to regulate its depth. High intensity light was generated with a lamp (6) and diffused with an etched glass (7). Images were recorded with an high speed camera (8) mounted on a tilt, rotating and movable micrometric stage. The components were controlled and synchronized detecting the falling drops with a light sensor (5) and using a delay circuit (9),

	ρ (kg/m^3)	μ (kg/ms)	σ (N/m)
Water	996	0.80×10^{-3}	71.22×10^{-3}
Acetic acid	1040	1.04×10^{-3}	26.63×10^{-3}

Table 1: Values of density ρ, viscosity μ and superficial tension σ for the used fluids at the reference temperature $T = 30\,°C$.

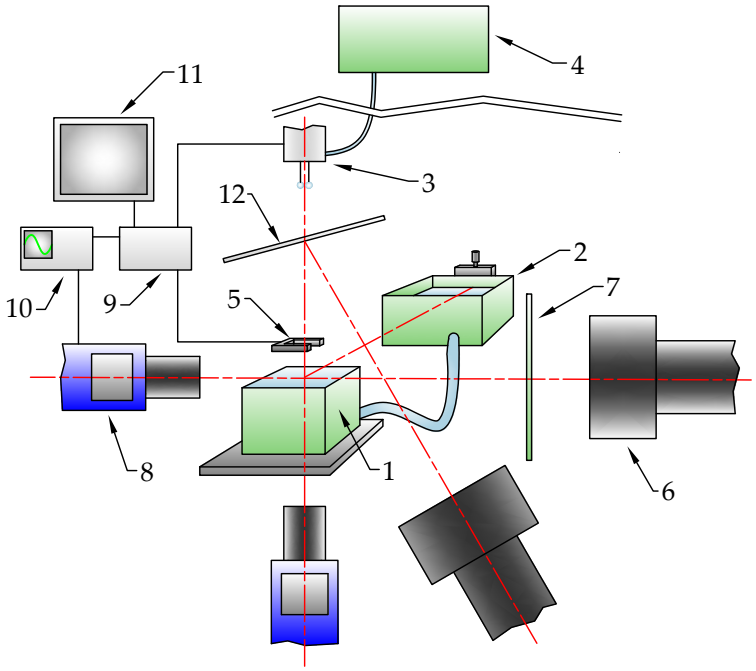

Figure 5: Experimental setup. The target pool (1) is placed on a level platform and it is connected to a level pool (2) mounted on a vertical micrometric stage. A vertical movable platform may be immersed in the target pool to regulate its depth. Falling drops, produced with a dripper (3), fed by a reservoir (4), are detected by a light sensor (5). A lamp (6) generates the light, diffused by an etched glass (7), needed to record high speed images on a camera (8) mounted on a tilt, rotating and movable micrometric stage. The components are controlled and synchronized with electronic cards (9), a wave generator (10) and a graphical user interface (11). When images were taken from below, light was reflected and diffused with an aluminium plate (12)

a wave generator (10) and a graphical user interface (11). When images were taken from below, light was reflected and diffused with an aluminium plate (12). The test rig built for the present study have been developed having focus on the impact of millimetric drops onto deep and thick liquid layers, however its application may be extended, with less complications, to the study of drop impacts onto thin liquid films, dry solid surfaces or other interface phenomena.

Due to superficial tension effects, the manipulation of small quantities of liquid is not easy. It has influenced the two main tasks of the performed experimental investigation, i. e. the generation of drops and the observation of the interface phenomena when the drops impact against the target liquid. Particular attentions were paid in the setup of the acquisition system, in order to get images sharp enough to permit an extensive image processing and to capture characteristics features.

Gauge	d_{ext} (mm)	d_{int} (mm)	s (mm)	V (µL/mm)
33	0.21	0.11	0.05	0.010
32	0.24	0.11	0.05	0.010
31	0.26	0.13	0.06	0.013
30	0.31	0.16	0.08	0.020
28	0.36	0.18	0.09	0.025

Table 2: Gauge index.

2.1 DROP GENERATION

Needles

Drops can be generated in different ways. In general the main tool is a needle. Different types of needles exist on the market, they are generally classified by their point type and by their gauge. For the present purposes the tip of the needle has to be blunt, since, for symmetry reasons, a not flat head induces a lateral momentum in the drops, when they are detached. Table 2 reports an extract of a gauge index list from HAMILTON. The main parameter is the external diameter, which influence the adhesion force of the drop on the needle.

Drop growth and detachment

As shown in Figure 6, when a pendant drop is generated on the tip of a vertical needle, its contact line moves to the external line of the section of the needle, where it remains pinned until the gravity force of the drop overpasses the vertical component of the surface tension force, which depends on the external diameter and on the contact angle θ and can be estimated:

$$F_\sigma = \frac{1}{2}\int_0^{2\pi} \sigma d_{ext} \sin\theta \, d\alpha = \pi\sigma d_{ext} \sin\theta. \tag{2.1}$$

Successively a more and more reduced section is formed just below the needle, till the detachment, as described by Zhang and Basaranb (1995). Sometimes, if the needle is very thin, the contact line of the drop can overcome the discontinuity of the external edge of the nose and go up on the stem. In these cases a covering with hydrophobic material like teflon may avoid the problem.

Gravity detachment

The use of gravity is the simpler way to produce drops, but has some limitations. First, the size of the drop is strictly dependent from the needle and different needles have to be used to produce drops of different diameters. Second, the instant of detachment cannot be controlled. Third, the gravity force ($\sim D^3$) reduces faster than capillary force ($\sim D$) when size decrease,

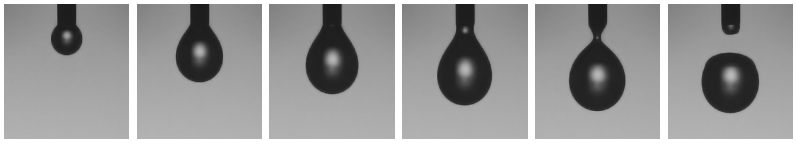

(a) (b) (c) (d) (e) (f)

Figure 6: Detachment of a drop from a needle because of gravity.

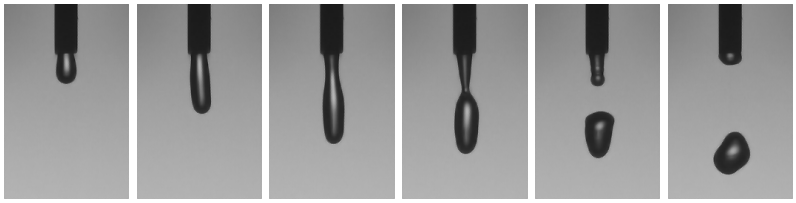

(a) (b) (c) (d) (e) (f)

Figure 7: Ejection of a drop from a needle.

Inertial detachment

thus there is a lower limit to the production of drop using standard needles of about 1.5 mm of diameter. These limitations can be overcome moving the needle in the positive vertical direction with an impulsive acceleration. This adds an inertial force to the drop in a suitable instant of time, allowing to detach drops of different sizes from the same needle and to obtain smaller drops. Further, the control of the instant of detachment permits to simultaneously detach drops from different needles, as will be discussed in Section 2.1.1.

Ejection detachment

A third way to detach drops from the tip of a needle is the ejection of a small amount of liquid, as shown in Figure 7. This method, typical of the inkjet printers, allows to obtain micrometric drops using, for example, piezoelectric generators Lee (2002), but can be used also in the millimetric region, where it permits to detach drops of different sizes from a same needle and at a desiderated instant, as will be discussed Section 2.1.1.

Break of a free jet

Another method is the break of a free liquid jet with induced Plateau-Rayleigh instabilities (Chandrasekhar, 1981), as shown in Figure 8, obtaining the impact of a stream of small drops instead of a single drop, which can be used, for example, to study drop impacts onto thin liquid layers (Yarin and Weiss, 1995).

Other methods

Several other methods may be found or invented, depending on the purposes or on the needs. For example in the impact of a millimetric drop onto a deep pool in the jetting regime (very simple to obtain), a crater is generated in the target liquid, from which a jet rise up during the receding phase. From the tip of the jet one drop may detach, rising up further and than falling down again onto the pool, generating a second impact of a smaller drop at low velocity, which would be more difficult to obtain

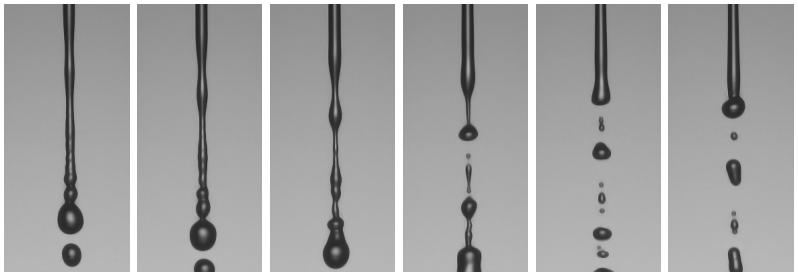

(a) (b) (c) (d) (e) (f)

Figure 8: Rupture of a jet in small drops because of Reyleigh-Plateau instabilities.

directly.

Drop deformations

All the methods may differ also for the initial deformation of the drops, in the early stage after the detachment. The shape of a falling drop is mainly influenced by a competition between surface tension and the aerodynamic drag. For small drops and low velocities the former prevails and the shape is absolutely close to that of a sphere. This is the case of the present work. After a drop is detached aerodynamic drag quickly acts to dump the oscillations generated during the detachment and the drop impacts onto the target surface as a sphere. If the falling time is very small (low velocity impacts), drops should be generated with a soft method, causing as small as possible oscillations in the drop. Aerodynamics drag takes more influence increasing drop sizes and falling velocity and it may result in a deformation of the drops or even in their fragmentation, as shown by a recent study of Villermaux and Bossa (2009).

2.1.1 *Double drop detachment*

To obtain a simultaneous impact of two or more drops two conditions are mandatory:

- The size of the drops has to be exactly the same (if the drops are detached from the same height with zero initial velocity). The falling velocity of an object does not depend on its size (and mass) only in the vacuum. In normal atmospheric conditions a little difference in sizes corresponds in different aerodynamic drags, preventing drops to simultaneously reach the target surface.
- The drops have to be detached at exactly the same instant of time. Small discrepancies may be caused by micrometric differences in the tip of the needles, where drops are pending, or by differences of the drop sizes, preventing the drops to simultaneously reach the target surface.

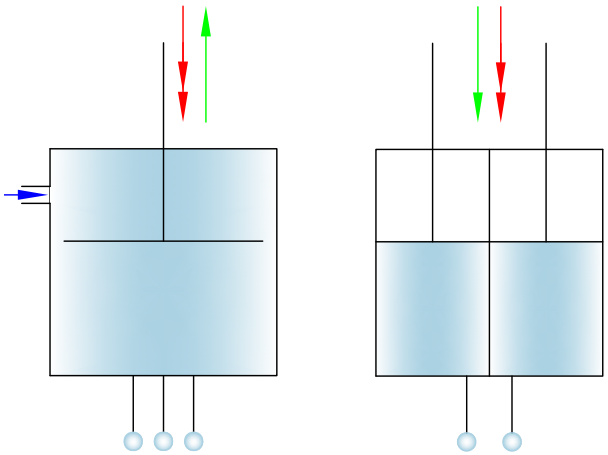

Figure 9: Sketch of the used (a) and of the suggested (b) dripper.

Dripper

In the present study simultaneous impacts of drops have been mainly achieved with a dripper, sketched in Figure 9a, previously developed at the University of Bergamo (Mancino, 2002). It is formed by a piston-cylinder system with three needles on the other face. The head of the piston is not sealed and the cylinder is full of liquid. The drops are continuously formed by gravity on the tip of the needles, while the cylinder is fed by a flow from a liquid reservoir. The detachment of the drops is obtained through an impulsive little movement of the piston. Its motion is given by a computer-controlled magnetic actuator and its stroke is regulated by a micrometric screw. After each impulse the piston goes back to the initial position. As shown in Figure 10, the impulsive movement of the piston causes the ejection of a small amount of liquid from the needles, giving to the pendant drops a vertical downward momentum, which in the end causes their simultaneous detachment. The dripper operates as a continuous system: the flow rate generates drops that are periodically detached by the impulse of the piston. Adjusting the frequency of the impulses of the piston and the flow rate it is possible to generate drops of different diameters.

The dripper has a very efficient way to detach drops at the same instant of time, but it has a few week points:

- equality of drop sizes;
- repeatability of drop sizes;
- choice of the drop diameters;
- choice of the instant of detachment.

Equality of drop sizes depends on growing velocity of each drop. At each instant of time the drops formed at the top of the needles have a size depending on the flow rate inside each needle. If

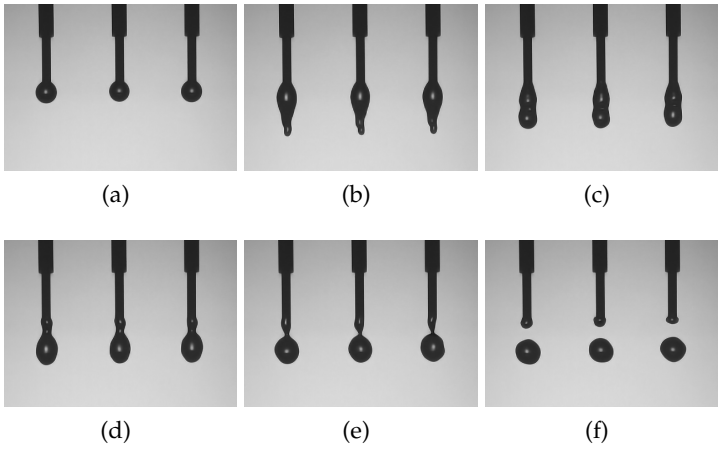

Figure 10: Detachment of drops from the dripper.

there are some discrepancies in the geometry and thus in the friction losses, the total flow rate coming from the liquid reservoir does not equally split along the channels of the needles, causing the growth of drops of slightly different sizes (Table 3 gives an idea of the sizes, volumes and masses of millimetric drops). Since friction losses depends also on flow rate, its reduction may reduce this problem but not completely prevent it. Repeatability of drop sizes depends on the flow rate used to feed the cylinder. It has been generated in two way: by pressurization of the liquid reservoir and by elevation of the liquid reservoir. The first method was the original one and it is suitable also to degas water, as requested by studies of drop impacts onto heated surfaces. However it was not possible, with the available compressor, to ensure a constant pressure and therefore a constant flow rate. Thus the liquid reservoir was elevated above the dripper to get a suitable discharge head and more constant flow rate, even if now dependent from the amount of liquid inside the tank. The choice of the drop diameters and of the instant of detachment is not free because of the continuous growth of the drops until their natural detachment. Thus instant of detachment and drop diameters are related together and with the flow rate, but these relations are not known a priori.

Dripper upgrade

To obviate these problems maintaining the very efficient way of detachment a new dripper, sketched in Figure 9a, has been suggested. It is formed by a number of piston-cylinder systems equal to the number of needles. Since the heads of the pistons are sealed inside the cylinders, the drops are in this case generated by a slow movement of the pistons, allowing a control of the drop sizes by controlling the stroke of the pistons, in a way typical of the syringe pumps. The drop detachment can be achieved again by an impulsive little motion of the pistons. Thus the pistons should be able to do slow movements to generate the

D (mm)	V (µL)	m (µg)
1.0	0.52	0.52
1.5	1.77	1.77
2.0	4.19	4.19
2.5	8.18	8.18
3.0	14.14	14.14

Table 3: Diameter, volume and mass of water drops in the range of investigation.

drop and impulsive infinitesimal movement to detach the drops. Each needle can be fixed directly on one face of the cylinder or externally, on a metallic plate, and connected with a flexible pipe to the cylinder.

A similar setup was tested using a HAMILTON one syringe diluter. It can moves the piston of a syringe up to 1500 steps, dispensing small amount of liquid, whose quantity depends on the section of the installed syringe. As sketched in Figure 11, during the suction phase the syringe takes the fluid from a reservoir, while during the active phase the syringe generate two drops of desiderate volume on the top of two needles. Since a dual syringe dispenser was not available, the flow produced by the syringe was slitted using a Y valve, having the problem on equality of drop sizes discussed above. Moreover the movement of the piston could not be enough quick to detach the drops (it was possible mounting a syringe with a larger section, but the consequence was a reduction in volume resolution). The detachment was then achieved using method cited in Sec 2.1. A simple mechanical system to obtain the vertical fast movement of the needles was produced by mounting needles on one side of a thin metallic bar, fasten on the other side on a support, as sketched in Figure 12. With an hammer it was possible to give a fast little vertical motion to the free side of the bracket, causing the drops do be detached, as shown in Figure 13, while the bracket soon cames back to the initial position thanks to its elasticity. The system was rudimental, but the method worked.

The system suggested could be completely realized using a dual syringe diluter or building a more compact ad-hoc device, but for reasons of costs and of time of development it has been chosen to keep using the old drop generator, also because digital image processing allows to have a relaxation of the control of the impact parameters, as will be discussed in Section 2.4.

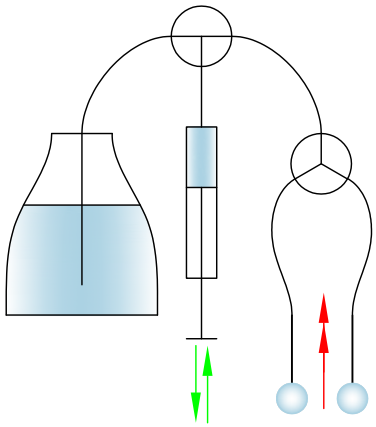

Figure 11: New setup of double drop generation.

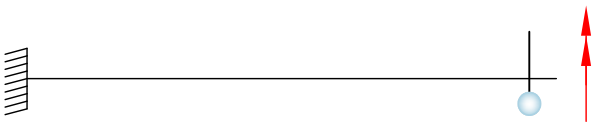

Figure 12: Sketch of the bracket used to mechanically detach drops.

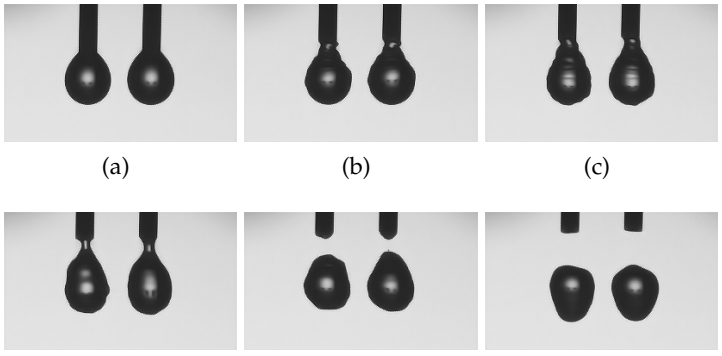

(a) (b) (c)

(d) (e) (f)

Figure 13: Double drop detachment due to an impulsive acceleration of the needles.

The container of the target fluid must allow the observation of the impact phenomena inside, so it has to be built in a transparent material, at least for the visualization windows on the light and on the camera sides. Initially it was built using polymethylmethacrylate (PMMA[1]), a plastic material even more transparent that normal glass, but also more sensible to abrasions and scratches and incompatible with alcohols. A second container was built with glass, but it is more complicate to make holes to connect pipes. The final best choice was to built a container using aluminium, which can be easily worked, with three glass windows on the bottom and on two opposite walls.

Size

The size of the container must be large enough to avoid wall influence on the impact phenomena. However, as will be explained later, increasing the size of the container increase also image distortion due to refractive effects, so it has been chosen in order to get a suitable compromise. To study drop impacts onto a deep pool a container of 10 cm $\times$ 10 cm $\times$ 10 cm has been used, while to study drop impacts onto thick films a container of 20 cm $\times$ 20 cm $\times$ 10 cm has been used. The larger size is due to the need to insert a vertical movable platform in order to change the depth of the pool.

The development of the container has followed the research of the elimination of the visualization problem caused by the liquid meniscus formed at the interface between the liquid surface and the walls of the container.

2.2.1 *Meniscus distortion*

As shown in Figure 14a, the meniscus formed by the target liquid on the walls of the container deflects away the light, obscuring the area close to the interface and preventing the observation of the liquid interfacial phenomena. The height h of the meniscus on the unperturbed surface may be calculated as (Bush):

$$h = l_c \cot(\theta), \tag{2.2}$$

where l_c is the capillary length:

$$l_c = \sqrt{\frac{\sigma}{\rho g}}. \tag{2.3}$$

The capillary length of water is about 2.7 mm and the contact angle θ on glass is about between 10° and 30°, giving a meniscus

1 PMMA is usually sold under many trade names and is commonly called acrylic glass, perspex or plexiglas.

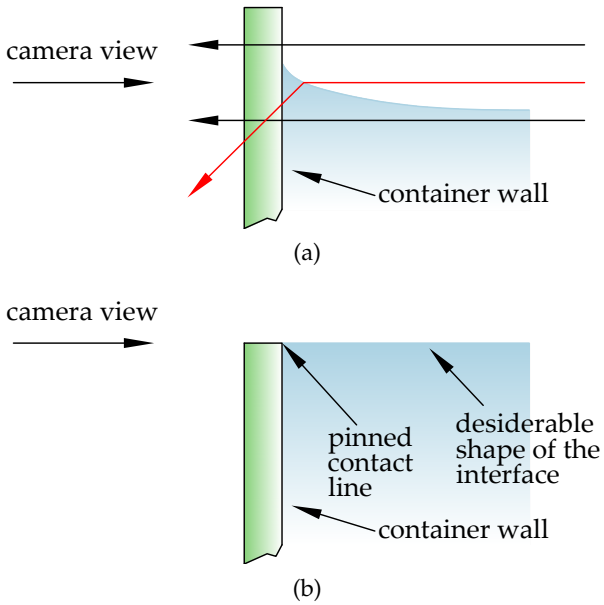

Figure 14: (a) Diffraction caused by the meniscus at the edge of the container. (b) Flattening of the meniscus using the edge of the container.

of height comparable with the drop size. The result is a black line in the recorded images in the region close to the interface, as evidenced in Figure 15. To solve this problem, both the menisci, formed on the wall close to the light side and on the wall close to the camera side, have to be flattened.

Methods to overcome the meniscus problem

In a study related with the interaction between a raising bubble and a free surface Di Marco and Di Gaetano (2008) used a smart system of mirrors to collect on the same camera the images coming from two slightly tilted views (one above and one below the liquid surface). However in the present study the solution of this problem has been based on wetting and constrained wetting.

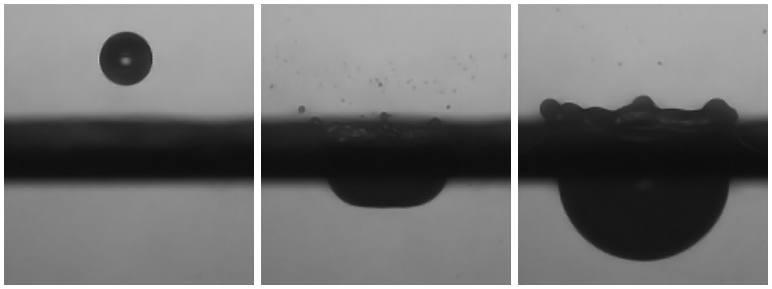

Figure 15: Drop impact with obscuration of the region close to the interface due to the meniscus between the target liquid and the walls of the container.

The better solution would be the use of a container made with a transparent material with a liquid-wall contact angle of 90°, but it is not simple find a material with the desired wetting properties, which are also strictly related to the liquid being used. Another way would be an internal coating (painted or stuck) of the container's walls. Both material neither coating, with the desiderate wetting properties, were found, so the solution has been looked for constrained wetting. If the container is hydrophilic, it can be filled to the brim in order to use it to reduce the meniscus. A similar solution is to stick a thin transparent sheet on the upper part of the internal side of the walls and use the little step formed to constrained the meniscus. A last solution is the use of an hydrophobic coating instead of the sheet and use the stepwise change in the wetting property as a constrain for the meniscus. In the performed experiments the container was filled to the rim, as shown in Figure 14, in order to use it to constrain the contact line. For this reason the two glass visualization windows on the walls were cut in a way to get as sharp, orthogonal and less indented upper edge as possible. As shown in Figure 5, the main container was also connected, by a flexible tube, to a liquid reservoir, placed on a micrometric vertical stage, making possible, thanks to the communicating vessels principium, accurately regulate the level of the water. Moreover, increasing the total surface of the liquid, reduce the change of the depth due to the impacting drops, which is negligibly small. In fact considering a surface of 200 cm^2 and a big drop of 3 mm of diameter, the change on the depth after each impact would be about 0.7 $^-$m, i.e. more than 700 drops are needed to change depth of 0.5 mm. The container was placed on a level platform to allow the liquid to simultaneously reach the rim of two opposite walls.

2.2.2 *Regulation of the depth*

For the impacts onto thick films, an ad-hoc movable platform has been built, following few main directives:

- it has to allow visualization from below;
- it has to permit an accurate vertical regulation;
- its bottom surface has to allow an accurate level regulation.

Vertical movable platform

As sketched in Figure 16, the platform is placed in the main container and it is supported by a lateral arm. The depth of the liquid pool H is fixed by the vertical distance between the edge of the container (which coincide with the liquid level, since it is used to constrained the meniscus) and the upper surface of the platform. As shown in the mechanical design of Figure 17, the platform is formed by two horizontal plates with a cavity. The

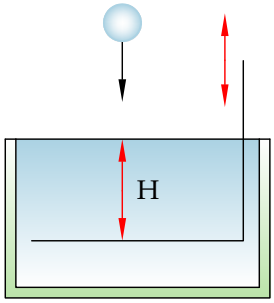

Figure 16: Sketch of the vertical movable platform used to change the depth of the target fluid.

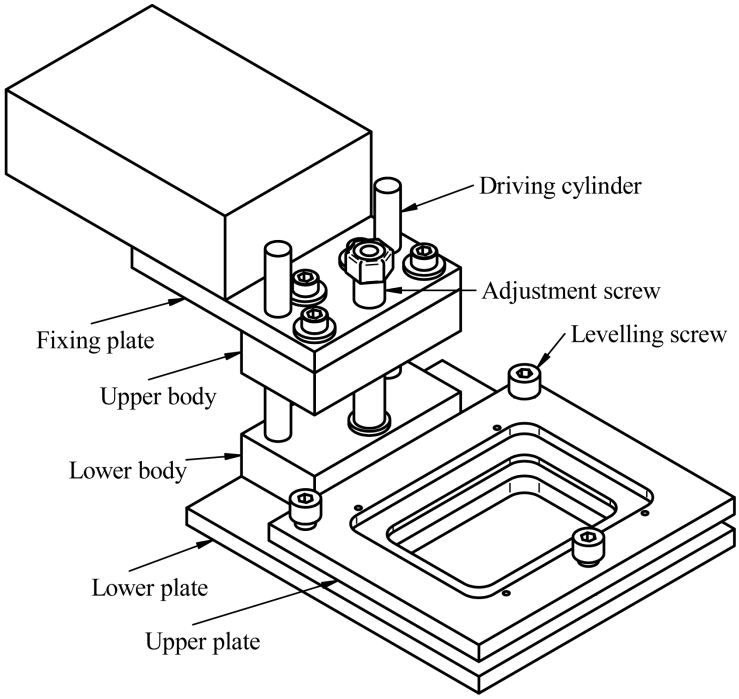

Figure 17: Mechanical design of the vertical movable platform used to change the depth of the target fluid.

upper base has a case for a glass impact plate. The upper plate leans on the lower plate through three screws, which allow the leveling of the surface in way to set it parallel to the above free liquid surface. The lower plate is integral with the lower body, which is hold by the adjustment screw (obtained from a metallic rod), which can freely rotate in the lower body and has a thread joint in the upper body. The upper body is fixed to the test rig with a fixing plate. The rotation of the adjusting screw permits to lift and to lower the platform, while the two driving cylinders, which have a thread joint in the lower body and can freely rotate in the upper body, ensures only a vertical movement, preventing the rotation of the platform.

High speed imaging has become a useful and power method of investigation in fluid-dynamics, and it has been used in the present study. High speed imaging allows two see and investigated phenomena which are to fast or to small to be observed with the naked eye and to perform measurements on them.

Frame rates

High speed imaging tends to reach higher and higher frame rates, in particular when it has to investigate small phenomena, since, as pointed out by Thoroddsen et al. (2008), the required frame rate is strictly affected by the optical magnification of the imaging. It becomes clear considering that a velocity of 1 m/s corresponds, under the microscope, to 1 µm/µs. Therefore, low velocity, or low Reynolds number, does not correspond to low frame rate, as the magnification must be considered. In free-surface flows at small length scales, the fluid motions are often driven by surface tension. For example the natural frequency of the n-th mode of oscillation of a drop is:

$$\omega_n = \sqrt{n\,(n-1)\,(n+2)\,\frac{\sigma}{\rho R^3}}, \tag{2.4}$$

which is equal to 100 kHz for the second mode of a water drop of 2 mm of diameter, requiring a very high frame rate to study this kind of phenomena. Equation 2.4 has been obtained for an inviscid liquid, and viscosity certainly affects the motion for very small drops, but the required frame rate still remains high.

Instruments

In the present study images were recorded with a PCO.1200 hs digital 12 bit CMOS high-speed camera mounting a SIGMA Macro 105 mm f/2.8 lens. A back-light continuous illumination was produced by a 1 kW lamp and diffused through an etched glass. Camera was synchronized with the impact using a delay circuit and detecting a falling drop with a STM fork sensor.

Parameters

The global setup of the acquisition system involves a number of parameters, often related each other. Here they will be introduced following a general approach, considering a single drop impact onto a deep pool and the characteristics of the used devices. The maximum size L of the subject, i. e. the drop impact, could be estimated considering that a water drop of 3 mm of diameter falling from a height of 1 m generates a crater not deeper than about 4 times the drop diameter in the target liquid and a crown of a comparable height above the target surface. Since the crater grows almost with an hemispherical shape, its width is double of its depth and equal to the depth of the crater plus the height of the crown, giving a reference volume with three similar dimensions of about 25 mm.

It is not worthless to note that the dimension of the subject is time-dependent, going from the smaller size of the drop before the impact to the bigger size of the crater and the crown at their maximum growth. One of the advantages of high speed imaging is the capability to record a sequence of frames very closed in time of the same event instead of take as many frames as different events, as in normal photography. Thus, the acquisition setup has often to be calibrated on the entire evolution of the phenomena under investigation.

The subject has to be recorded on a length L_{rec} given by the sensor of the camera, which has a maximum size of 15.36 mm $\times$ 12.29 mm, formed respectively by 1280 px $\times$ 1024 px of 0.012 mm $\times$ 0.012 mm each. Taking the smaller size as reference, the real dimension l_{sbj} would be recorded on a virtual dimension $l_{\text{rec}} =$ 12.29 mm formed by $n = 1024$ discrete bits of $s = 0.012$ mm each, with a magnification:

$$m = \frac{L_{\text{rec}}}{L} = \frac{n\,s}{L} \tag{2.5}$$

of about 0.5 and a circle of confusion (which is the inverse of the spatial resolution):

$$c = \frac{m}{s} \tag{2.6}$$

of about 0.025 mm/px. However, the frame rate *fr* of the camera depends on the region of the sensor (ROI) actually selected and used, with higher frame rates corresponding to smaller ROI. The maximum frame rate available with the full size of the sensor is 636 fps, which might increased up to 30 000 fps for a ROI of 16 px $\times$ 1024 px. The reduction of the ROI corresponds to an increase of the frame rate only if the width is reduced, while the height may be always kept to its maximum size without a reduction in the frame rate. If the subject under investigation has a bigger horizontal extension and more frame rates are needed, the camera may if necessary be rotated[2] of 90°. This has been the case of the present investigation, since a greater hight of the ROI was useful to record few frames of the drop before the impact, in order to measure its velocity and diameter.

As seen, increasing the frame rate, i. e. in the time resolution, means a reduction in the spatial resolution and a deal has to be found. Moreover, the choice of a spatial resolution also influence other related parameters. Referring to Figure 18, a point in the plane of focus at a distance u from the lens is sharply imaged in a point at distance v behind the lens. A point at a distance u_{d} would be sharply imaged at a distance v_{d} behind the lens; however, at the focus distance v, it is imaged as a disk, known

2 The images can be then easily rotated in the right position during the post processing.

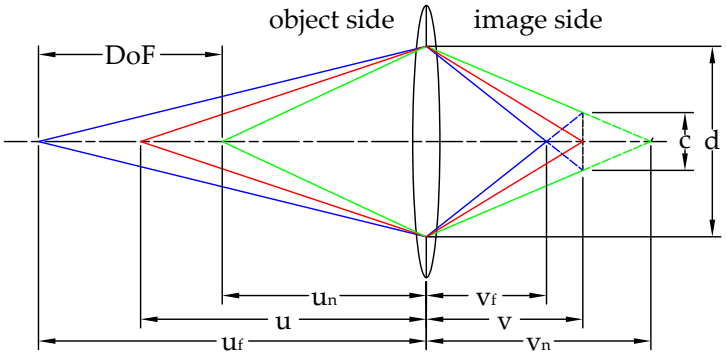

Figure 18: Lens nomenclature.

as a blur spot. If the blur spot is sufficiently small, it is indistinguishable from a point, so that a zone of acceptable sharpness, known as the depth of field *DoF*, exists between two planes on both sides of the plane of focus. The plane at u_n is the near limit of the *DoF*, and the plane at u_f is the far limit of the *DoF*. The diameter of a 'sufficiently small' blur spot is known as the acceptable circle of confusion CoC. The size of the blur spot may be reduced by reducing the size d of the aperture.

Using simple geometric optics, the distance u of the object from the lens and the distance v of the sensor from the lens, corresponding to a sharp focused recorded image, may be related by the magnification m (Conrad, 2004):

$$m = \frac{v}{u} \tag{2.7}$$

and by the thin lens equation:

$$\frac{1}{f} = \frac{1}{u} + \frac{1}{v} \tag{2.8}$$

where $f = 105\,\text{mm}$ is the focus length of the used lens. The range of variation of v depends on the lens. It's minimum value is equal to the focus length:

$$v_{\min} = f, \tag{2.9}$$

and corresponds to $u = u_{\max} = \infty$, coherently with the definition of the focus length. The maximum value of v is generally given by the lens builder in terms of the minimum distance of focus $u_{\min}$ and it can be calculated using Equation 2.8:

$$v_{\max} = \left(\frac{1}{f} - \frac{1}{u_{\min}}\right)^{-1} \tag{2.10}$$

which gives about 158 mm for the used lens. The depth of field *DoF* may be expressed as:

$$DoF = \frac{f\,u^2}{f^2 - Nc\,(u-f)} - \frac{f\,u^2}{f^2 + Nc\,(u-f)} \tag{2.11}$$

where N is the lens f-number, which is a dimensionless number giving the ratio of the focus length f to the diameter d of the entrance pupil of the diaphragm of the lens[3].

Up to now the acquisition setup is regulated by 11 parameters:

$$\{L, f, N, s, fr, u, v, DoF, c, m, n\}, \tag{2.12}$$

where the dimension of the subject $\{L\}$ is fixed by the phenomenon under investigation, the focus length and the aperture $\{f, N\}$ are fixed by the choice and the setup of the lens, the dimension of the pixels of the sensor $\{s\}$ is fixed by the choice of the camera, the frame rate, the distance of the lens from the subject and from the sensor, the depth of field, the circle of confusion and the magnification $\{fr, u, v, DoF, c, m\}$ are fixed by the Equations (2.5,2.6,2.7,2.8,2.11), which may be rewritten as a function of the number of pixels $\{n\}$ selected to record the subject, used as independent variable:

$$u = \frac{f(l + n\,s)}{n\,s} \tag{2.13a}$$

$$v = \frac{f(l + n\,s)}{l} \tag{2.13b}$$

$$DoF = \frac{2d\,f^2L^2n(l + n\,s)}{(-d\,l^2 + f\,n^2s)\,(d\,l^2 + f\,n^2s)} \tag{2.13c}$$

$$m = \frac{n\,s}{l} \tag{2.13d}$$

$$c = \frac{n}{l} \tag{2.13e}$$

$$fr = (1.98 \times 10^{-6}\,n + 8.07 \times 10^{-6})^{-1} \tag{2.13f}$$

where Equation 2.13f has been empirically obtained with a best fit linear interpolation of the values of fr and n of the used camera.

Figure 19 shows the values of all this terms as a function of n. A bigger ROI means a lower circle of confusion c (thus a larger spatial resolution) and a greater magnification m, but also a smaller frame rate fr. Moreover the distance u between the subject and the lens has to be augmented and this may cause problems of illumination.

Sampling

The intensity of light reaching the sensor has to be sufficiently high to be detected and classified by the sensor of the camera. The available camera mounted a 10 bit sensor, meaning that the light intensity might be sampled in 2^{10} numbers. Intensity of light equal or below the minimum sensitivity of the sensor takes value zero, while intensity of light equal or above the maximum sensitivity of the sensor takes value 1023. All the intermediate

3 In photography the f-number is commonly expressed with 'f/' preceding its numerical value.

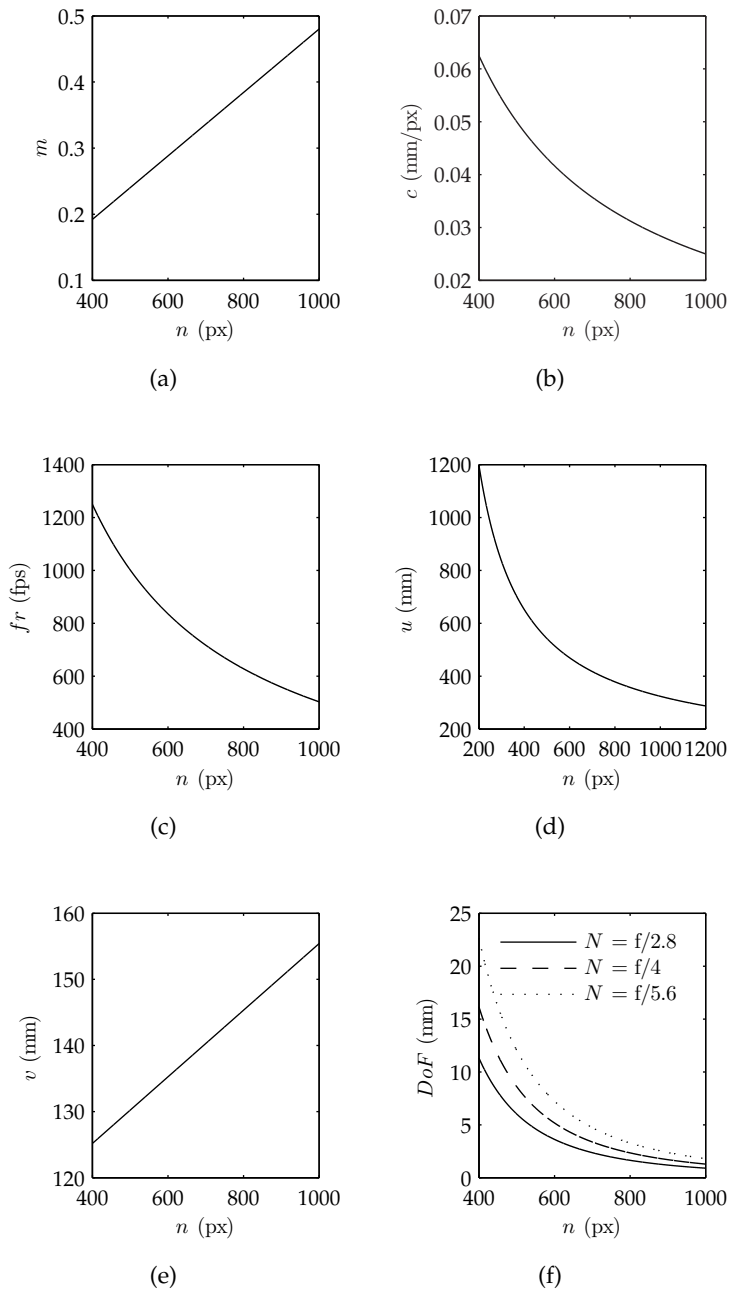

Figure 19: Behavior of some parameters of the acquisition setup as a function of the width of the ROI chosen to represent a real dimension of the subject of 25 mm. Values have been calculated assuming a focus length $f = 105$ mm and a pixel size $s = 0.012$ mm. 19a Magnification m. 19b Circle of confusion c. 19c Frame rate fr. 19d Distance u of the subject from the lens. 19e Distance v of the sensor from the lens. 19f Depth of field DoF for the three bigger f-numbers N.

values of light intensity are equally classified (depending on the linearity of the sensor) in the remaining numbers.

Illumination

For a fixed light source, the amount of light allowed to reach the lens is regulated by the aperture of the diaphragm and by the exposure time. The former has an influence also on the *DoF*, as shown in Figure 19f, where it can be seen how *DoF* increases when the aperture decreases. Its regulation has the goal to make the image suitably fit its histogram. In high speed imaging, a sufficient amount of light to record a well sharp image has to be collected with an exposure time which maximum value is constrained by two reasons:

- the chosen frame rate fixes a limit on the exposure time. For example a frame rate of 1000 fps means that 1000 images are collected each second, thus the exposure time cannot obviously be greater than 1 ms.
- The chosen spatial resolution has often to be ensured for moving subjects. For example a drop falling from an height of 62 cm impacts onto the target surface with a velocity of about 3.5 m/s and a spatial resolution of 0.1 mm/px can only be obtained with an exposure time not greater than 30 µs.

In the present study the exposure time had to be lower than 30 µs and the diaphragm, even if with an high intensity light given by a 1 kW lamp, had to be used completely or almost completely open $N = f/(2.8 - 4 - 5.6)$, with a limitation of the depth of field. In general the problem may be solved in two ways:

- increasing the light intensity, with the consequence to increase also the external influence on the observed phenomenon, which will be heated up by the light. An infra-red filter may be interposed between the light source and the subject, but it will also probably reduce the intensity of the visible light.
- Increasing the sensibility of the sensor of the camera, which should be sensible to smaller intensities of light, still remaining capable to suitably recognize its gradients.

Memory

A last constrain to consider is the memory consumption. The used camera had a RAM memory of 1 Gbyte, meaning that recording at the full sensor size and at the relative maximum frame rate the time of recording has to be lower than:

$$t < \frac{1\,\text{Gbyte}}{(1280 \cdot 1024 \cdot 12)\ \text{bit} \cdot 636\,\text{fps}} = 0.4\,\text{s}, \qquad (2.14)$$

which is bigger than the time of an impact event, lasting less than 0.2 s. It only makde a limit on the number of successive

events that can be recorded before to discharge the data on an external device, as the hard disk of a computer.

Each sequence of acquisition was saved in a *tiff*-format file. This file coding has the capacity to store sequences of 16 bit images in a single file, increasing the handiness of the data. As written above, the camera produces only 10 bit images, but they are recorded in a 16 bit format because it does not exist a specific 10 bit format.

In the present investigation high speed imaging was used to take pictures of drop impacts mainly from a side of the impact point, recording a two-dimensional projection of the three-dimensional phenomenon. For this reason, particular cares were paid to source of image distortion due to alignment and refractive effects.

2.3.1 *Image distortion due to alignment*

Referring to Figure 20, the position of the camera is defined by Tait-Bryan angles, which, together with the height of the camera, have to be adjusted in order to get the lens axis lying on the plane of the target liquid, in direction of the impact point. For this reason the camera was mounted on a tilting, rotating and movable platform.

If, for example, a reference cylinder vertically suspended at the impact point, as in Figure 20, have to be recorded, the ideal image would be that represented in Figure 21a. Respect to this ideal case, a variation of the pitch angle causes the two dimensional liquid surface to be projected on the sensor of the camera not as a line, but as a strip, with a distortion similar to that of the meniscus described in Section 2.2.1, as represented in Figure 21a. A variation of the roll angle causes the record of a skew image, as represented in Figure 21c. A variation of the yaw angle causes a discontinuity in the images between the two regions above and below the liquid surface, as represented in Figure 21d. This is due to refractive effects when the axis of the lens is not orthogonal to the walls of the container. Refractive effects induce the light coming from the submerged part of the impact to have a different path respect to light coming from the part above the liquid surface.

2.3.2 *Image distortion due to refraction*

As light passes the border between two media, depending upon their refractive indices n, the light will either be refracted to a

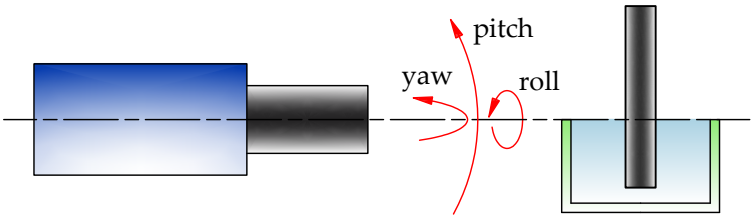

Figure 20: Angles defining position of the camera.

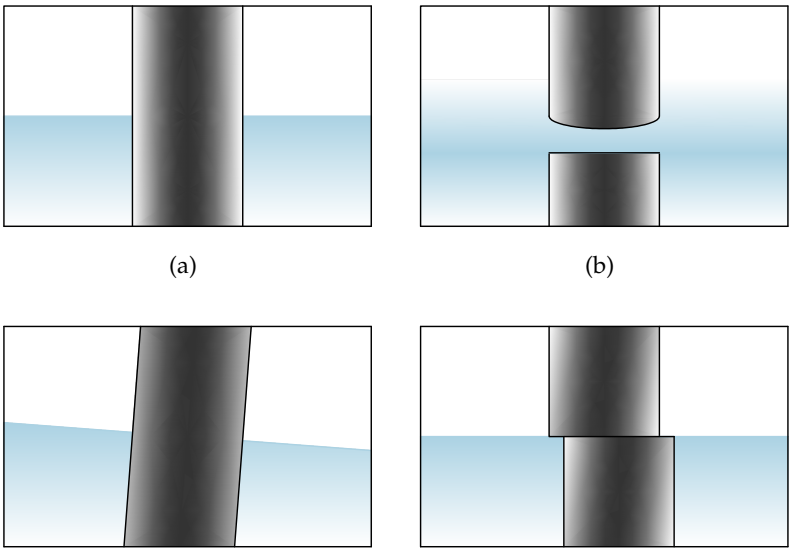

Figure 21: Effects of a variation of the Tait-Bryan angles, defining the position of the camera, respect to a ideal case. (a) ideal case with a perfect alignment. (b) variation of the pitch angle. (c) variation of the roll angle. (d) variation of the yaw angle.

lesser or a greater angle (Table 4 lists the values of some refractive indices). These angles θ are measured with respect to the line orthogonal to the boundary and are related to the refractive indices by Snell's law:

$$\frac{\sin\theta_1}{\sin\theta_2} = \frac{n_2}{n_1}. \tag{2.15}$$

In the present study, light coming from the submerged part of the phenomenon crosses two interface: water-glass and glass-air. Applying Equation 2.15 to both the interfaces and rearranging the two equations it comes that deviation does not depend on the refractive index of the wall, but only on the two refractive indices of the liquid inside the container and of the air outside:

$$\sin\theta_a = \frac{n_g}{n_a}\sin\theta_g = \frac{n_w}{n_a}\sin\theta_w \tag{2.16}$$

Since angles are small and the refractive index of water is greater than refractive index of air, light coming from the submerged part of the phenomenon is refracted away from the normal line. Figure 22 represents a section of the target container on the yaw plane and shows an example of this effect. The real point P is recorded as if it is in the position P', with a shift along the vertical and horizontal position, leading to two main consequences:

- Due to the vertical shift, the region below the liquid surface is recorded bigger than in reality, as shown in Figure 23. This is known as the water magnification effect. Differences on sizes between upper and lower parts in the recorded images are taken into account using two different calibrations for measurements performed above and below the surface.
- Due to the horizontal shift, two different focus distances are needed to focus both the above and submerged parts of the impact. If the difference between the two lengths is greater of the depth of field, focusing the camera on the upper part may lead to the unfocused appearance of the lower part of the image, and viceversa, as shown in Figure 24. This difference increases with the distance between the observed phenomena and the wall. Thus this distance has to be as little as possible, but large enough to avoid the influence of the wall on the impact phenomena.

2.3.3 *Alignment procedure*

In the quality of the recorded images depends on a great numbers of levelings and alignments. Even if a number of micrometric stages have been used, before each set of acquisition, a quan-

material	n
air	1.00
water	1.33
glass	1.52
PMMA	1.49

Table 4: Refractive indices.

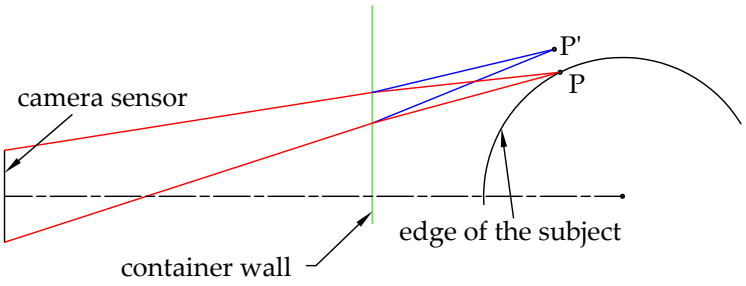

Figure 22: Explanation of the water magnify effect.

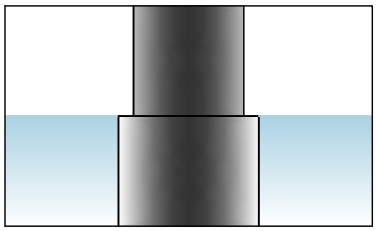

Figure 23: Example of the water magnify effect.

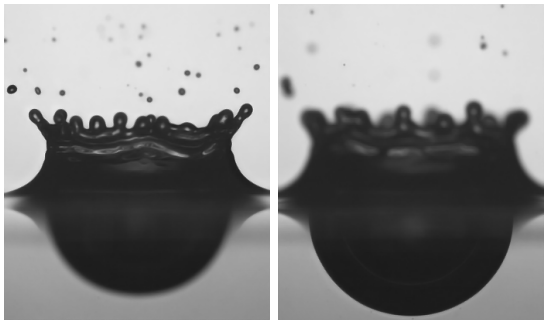

(a) (b)

Figure 24: Difference between images taken focusing above or below the water surface.

tity of a time and patience was needed to setup the acquisition system. The following alignment procedure was performed:

A. the level platform of the target container was adjusted as horizontal as possible using an high precision spirit level. The levelings have to be performed on different heights of the platform, in way to iteratively set also its vertical axis orthogonal to the liquid surface.

B. The target container was placed on its platform and the camera was adjusted with the central region of the field of view as orthogonal as possible to the plane of the rims of the target container, iteratively focusing on the nearer and farer rim until they did not lie on the same line.

C. The lift platform was placed inside the target container, with the upper surface a little below of the brims, and adjusted as horizontal has possible using the high precision spirit level.

D. The target container was connected to the level container and filled to the brim, checking the water to reach at the same time first the edges of the lift platform and than the brims of the container.

E. The camera and the light were turned on and the level of water into the target container was accurately adjusted acting on the vertical stage of the level container, checking on the monitor and reducing the thickness of the black line produced by the menisci. If necessary the camera was again a little regulated.

F. The cylinder of calibration was vertically suspended in the middle of the target container, with the lower part immersed into the pool liquid and the camera was focused on it.

G. The aperture of the camera and the distance of the light were set in order to suitably fill the image histogram. The distribution might be a little narrowed using a smaller aperture in favor of an increase in the depth of field.

H. The lamp was aligned with the camera and the cylinder of calibration to have an equal illumination of the two edges of the cylinder, to avoid small later errors in edge detection during image processing.

I. The target container was a little rotated in order to correct the yaw angle and to avoid the problem explained before, checking on the monitor the profile of the cylinder of calibration.

J. The cylinder of calibration was removed and some impacts were produced in order to adjust the position of the dripper to have impacts in the well focused region, while the

position of the drop detector was adjusted to correctly detect each drop. It was mounted as close to the target surface as possible, to detect only drops impacting in the focused region, since little flows in the surrounding air might easily influence the trajectory of the falling drop.

k. In the case of double drop impacts the position of the dripper has to be adjusted also two have the same distance of the two drops from the lens.

l. The synchronizing system was set to start the acquisition few time before the impacting drop was in the ROI of the camera, in order to have some first background images, useful for the subsequent image processing. The end-time of the acquisition was also properly set.

In the end the recorded images are the final product of all the experimental investigation. They are the raw entities containing the greater amount of data, which have to be converted to a more suitable format by image processing.

2.4 IMAGE PROCESSING

Impact parameters

Image processing has been first used to measure the impact parameters, i.e. drop diameter and impact velocity, which were used to select and to classify each recorded event. Both quantities were measured using five frames foregoing the impact, in order to reduce drop oscillations effects. Also the shape of the impacting drops was checked, revealing often the absolute similarity with a circle. For this reason, even if the drop diameter was calculated with an equivalent area method, the results were checked to be very close to those of other methods. Velocity was measured using the evolution of the vertical position of the center of area of the drops and the frame rate as time. Image processing was than used to recognize features of the investigated phenomena and to perform measurements on them. All the time-dependent variable quantities were measured assuming as a reference the first instant of drop impact, interpolated knowing the velocity of the drop in the last frame before impact and its distance from the unperturbed target surface.

Features

Time and spatial resolution

The time between to subsequent frames, i. e. , the time resolution, is given by the camera through the value of the frame rate, while the correspondence between the lengths in the images and the real lengths, i. e. , the spatial resolution, is obtained through a spatial calibration. It was performed recording a frame with a reference object after each set of acquisitions. The reference object was a calibrated cylinder vertically suspended in the focused area, with the lower part submerged into the pool in a way to

have on the same frame both air and water calibrations. Recorded images had a spatial calibration of about $14 - 25\,\mathrm{px/mm}$.

Relaxation of repeatability

Image processing may simplifies the control of the parameters governing the phenomenon under investigation. For example, in the present study, it allows, for each event, to measure the diameter of the impacting drop as well the impact velocity directly on the recorded frames, reducing the importance of having to know (and to control) exactly the impact conditions a priori.

Digital images

A grey-level image can be represented with a numeric matrix. The value of each cell of the matrix represents the light intensity of the corresponding pixel in the image. The lower value 0 is equivalent to the black. The higher value, corresponding to white, is equal to $2^b - 1$, where b is the bit-depth of the image and may have typical values of 8, 10, 12, 16. Thus, in the simpler case of a 8 bit image, the intensity is divided into 256 levels with integer values from 0 to 255. In the end image processing is a form of digital signal processing (DSP) technique working on matrix of numbers representing the images. This explains the advantage to process images in an environment like MATHWORKS Matlab, which provides also a powerful toolbox of a comprehensive set of reference-standard algorithms and graphical tools for image processing, analysis and visualization, which can easily be integrated with own code. Other useful used programs were MEDIA CYBERNETICS Image-Pro Plus, which allows to easily manipulate the *tiff*-sequences of images, and ADOBE Photoshop, which has powerful tools for image enhancement. For simple visualization of the image was used the freeware Faststone Image Viewer. All the frames of each event were recorded together in one file, in a *tiff* sequence, which was then processed. Although the code was automatic, analysis were run together with a graphical interface showing frame by frame the edges of the detected features superimposed with the original image and allowing for a user visual control. Each recorded sequence was started when the impacting drop was not yet in the view area of the camera, to get a free background in the first frames, to be used in image processing, while as the last frame was attached the calibration frame previously recorded.

Algorithm

All the measurements imply a similar algorithm composed of edge detection, object recognition and features extraction and analysis. Here only the main steps will be presented, while further details can be found in the comprehensive available literature, e. g. , (Pratt, 1991, Gonzalez, 2003). As written above, an image can be represented with a numeric matrix:

$$I(x_i, y_i), \tag{2.17}$$

where x_i and y_i are the rows and the columns of the cells of

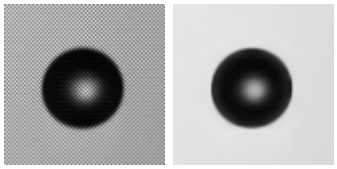

(a) (b)

Figure 25: Example of a grey-level image of a falling drop. (a) Original image. (a) Enhanced image.

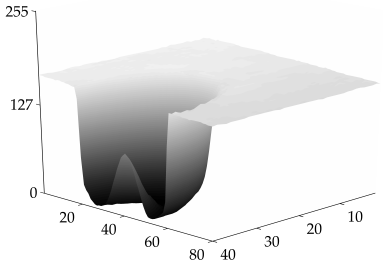

Figure 26: Three dimensional plot of a half of Figure 25a.

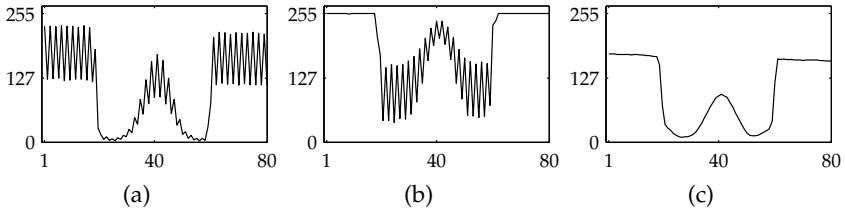

Figure 27: Plot of the intensity values of the central row of Figure 25a. (a) From the original image. (b) After background subtraction. (c) After a edge-preserving smoothing filter.

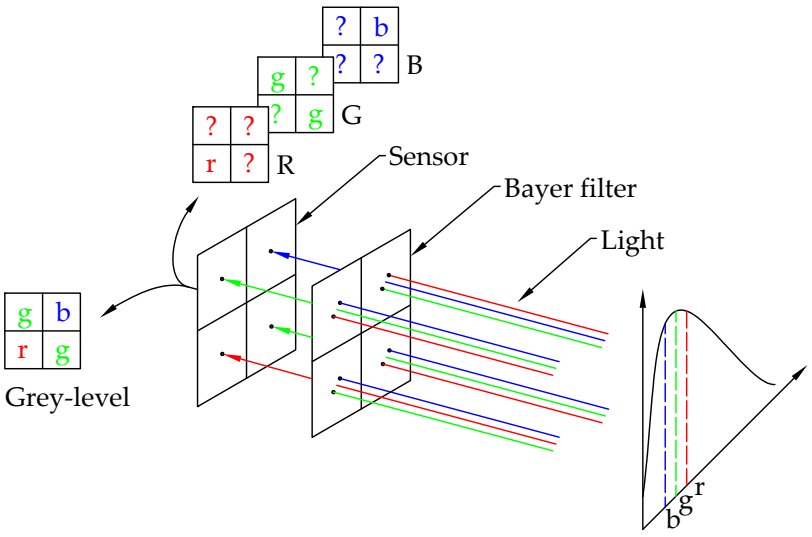

Figure 28: Bayer filter.

the matrix, corresponding to each pixel in the image. A three-dimensional plot of the values of the matrix, Figure 26, explains how the edges of an image match with gradients in the values of the matrix. Figure 27a shows the intensity plot along the central row of the matrix representing the image of Figure 25a. The great oscillation of the values is due to the fact that the grey-level images have been recorded using a color camera.

Bayer filter

Color images are represented by a combination of three matrices, defining for each pixel three values, which uniquely represent a color in a chosen color space, like the RGB (red, green, blue) space. They are generally recorded using a Bayer filter, named after its inventor, which is a color filter array for arranging RGB color filters on a square grid of photosensors, as shown in Figure 28. The filter pattern is 50 % green, 25 % red and 25 % blue. Green elements are twice as red or blue to mimic the human eye's greater resolving power with green light. Since each pixel is filtered to record only one of three colors, the data from each pixel cannot fully determine color on its own. To obtain a full-color image, various demosaicing algorithms can be used to interpolate a set of complete red, green, and blue values for each point.

Bayer filter distortion

When a grey-level image is recorded with a color camera, it simply is the raw matrix of the data of each pixel. Since the light recorded by each pixel does not belong to the same frequency range, the corresponding recorded value is different also in case of a same total light incidence. In the end the grey-scale images are formed by a pattern of 4×4 pixel of different values also in the presence of a uniform illumination. This variation cannot be easy eliminated, without blur the edges, because of the differences are not constants, but depend on light intensity and distribution. For example background subtraction usually allow to obtain sharper images, more suitable for edge detection, if a background image is available. Figure 27b shows the result of this operation, evidencing the positive smoothness effect on the background pixels (higher values), but the worsening of the oscillations on the foreground pixels (lower values). Doing this operation the average luminosity of the image also change, but could be preserved adding to the result a value equal to the average intensity of the original image. However luminosity has only effect on the visualization of the image, not on the later process of edge detection. Figure 27c shows the effect of the application of an edge-preserving smoothing filter. The result is good and the sharpness of the edge is much more preserved than it has been with other generic smoothing filters, as showed in Figure 25, where (a) is the original image and (b) is the enhanced image. However image enhancement cannot recover the lost of resolution due to the Bayer filter, with the consequent loss of the

finer details.

Edge detection

The main task of all the performed image processing has been the detection of edges. As it is evident from Figure 26, and edge is located in correspondence of a sharp (usually monotonic) variation (gradient) in the intensity values of an image. Such a discontinuity may be numerically detected in three ways:

- dividing the foreground regions from the background using a threshold value;
- finding places where the first derivative of the intensity is greater in magnitude than a specified threshold;
- finding places where the second derivative of the intensity has a zero crossing.

Figure 29a represents the intensity profile $I(x_i)$ of a one dimensional image formed by 60 pixels. The background pixels on the left (higher value) are separated from the foreground pixels on the right (lower value) by a region of variation of intensity, which may represent an edge. The two regions may be detected choosing a threshold value t, fixing at the same time the position of the edge. At different threshold values may correspond different positions of the edge, as can be evinced from Figure 29a, with a range equal to the length of the variation. Figure 29a shows the first derivative $I'(x_i)$ of the intensity distribution $I(x_i)$. In this case the edges may be formed by the pixels where the value of the derivative is greater (in absolute value) of a threshold value t. It is clear how edges may have a thickness greater than one pixel and the exact position of the edge may be fixed in correspondence of a local maximum or with other methods. The chosen value of the threshold have a decisive consequence on which edges will be detected. Figure 29a shows the second derivative $I''(x_i)$ of the intensity distribution $I(x_i)$. It characterized by two sharp picks of opposite sign at each side of the region of variation. The position of the edge may be fixed by the zero crossing of the segment linking these two pick points. In this case it is always uniquely determined and it does not depend on threshold values. A more accurate approach is to perform some kind of interpolation to estimate the position of the zero crossing to sub-pixel precision.

In the present study the second has been chosen, even if, as second order derivative, it is often unacceptably sensitive to noise. However zero crossings always lie on closed contours, the only exception to this is where the curve goes off the edge of the image, and, actually, it is best to think of the zero crossing detector as some sort of feature detector rather than as a specific edge detector. This characteristics is very useful because it allows to detect all the possible objects in an image, from which a

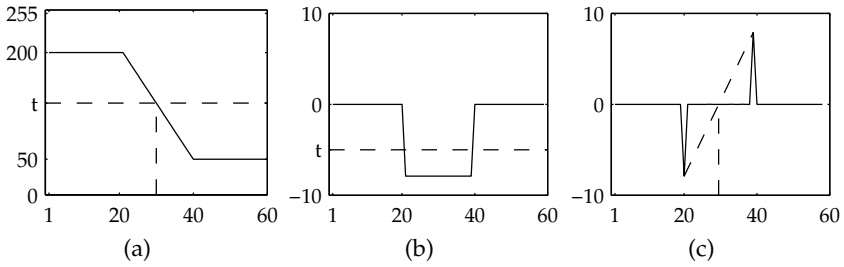

Figure 29: Example of edge detection. (a) Intensity profile of a virtual one-dimensional image of 60 pixels. (b) First derivative and threshold value t. (c) Second derivative and zero crossing.

selection can than be made. The problem of noise may be overcome convolving (filtering) an image with the Laplacian of a Gaussian (LoG), which smoothes the image (reduce noise) and computes the Laplacian. The behavior of the LoG zero crossing edge detector is largely governed by the standard deviation of the Gaussian used in the LoG filter. The higher this value is set, the more smaller features will be smoothed out of existence, and hence fewer zero crossings will be produced. Hence, this parameter can be set to remove unwanted detail or noise as desired. The idea that at different smoothing levels different sized features become prominent is referred to as scale. Figure 30a shows the result of this kind of operation, with low standard deviation, on Figure 25, where it is clear how zero crossings occurs at any place where the image intensity gradient starts increasing or starts decreasing, also in regions of very low gradient where the intensity gradient wobbles up and down around zero, and this may happen at places that are not obviously edges. Applying the same filter after have performed a background subtraction to the original images may help to reduce the numbers of spurious regions, as shown in Figure 30b. The unwanted regions may further be reduced by simply threshold the LoG output, as shown in Figure 30b, but this imply loosing the useful characteristics of detect always closed contours and has to be carefully performed. At this point all the touching pixels with the same logical state in the binary image can be divided in blob (binary large object), which can be labeled. Therefore, with a series of processing operations and analysis functions, a set of selected properties may be measured for each of them, produce information about any two-dimensional shape in an image. In presence of an high-speed sequence of images the trajectories of the detected objects may be tracked and a additional set of time-dependent properties may be calculated. In the presented example the drop represents the greater region detected, so all the other smaller regions can be deleted before to measure characteristics values as the equivalent diameter, the area or the eccentricity and to

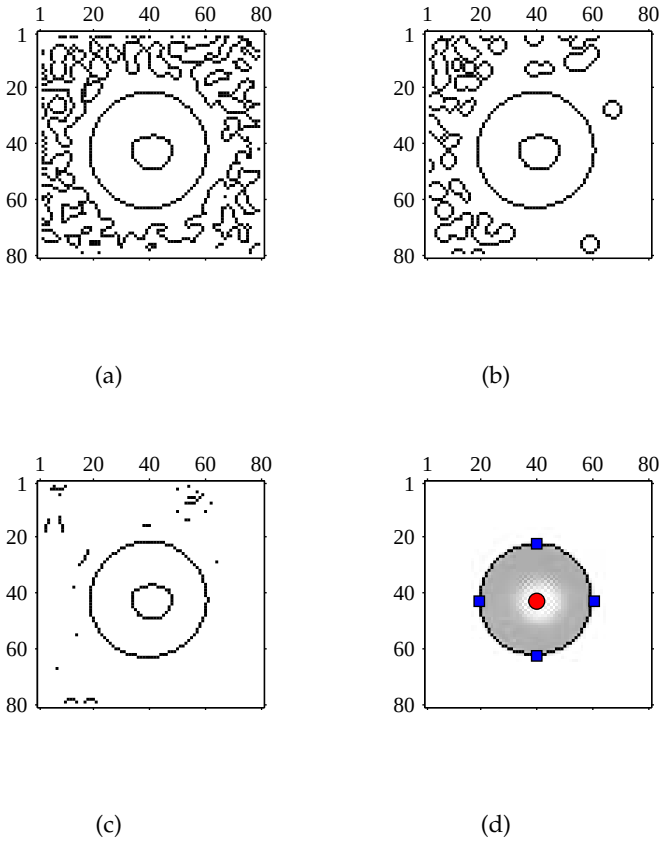

Figure 30: Example of edge detection with the Laplacian of a Gaussian method and feature recognition. (a) direct application. (b) application after background subtraction. (c) application with a threshold value. (d) features individuation.

detect the characteristics features as the extreme horizontal and vertical points or the center, which may be superpose to the real image, as shown in Figure 30d, for a visual user control.

3

SINGLE DROP IMPACTS ONTO A DEEP POOL

Phenomena of drop impacts have been extensively studied and discussed in previous literature. Rein (1993) wrote a comprehensive review on drop impacts on both solid and liquid surfaces, while Yarin (2006) restricted the area to thin liquid layers and dry solid surfaces. Wetted and dry solid surfaces were also considered by Sikalo and Ganic (2006). Thoroddsen et al. (2008) presented a technical review on ultrahigh-speed video cameras and their applications in experimental fluid mechanics, with an emphasis on the study of free-surface flows as the dynamics of drops and bubbles. Compressibility may have a role only in the very early stage of the drop impact and their effects are typical for high-speed impacts, which were reviewed by M.B. Lesser (1983), with a background mostly arising from liquid erosion problems related to materials-science aspects. Prosperetti and Oguz (1993) dealt mostly with phenomena of drop impacts related to the underwater noise of rain. Impact onto thin films or dry surfaces and compressibility effects have not been considered in the present study.

In the present study the impacts of a single drop onto a deep pool have been considered in order to made a comparison with double drop impacts, as will be presented in Chapter 4. In this section only a general survey is presented, in order to introduce all the related phenomena and nomenclature. However, from a literary review and from the present experimental data, some new details have been added:

- a new classification of the flow regimes has been proposed;
- a new flow regime has been detected;
- the splashing has been discussed;
- the dome formation has been observed to depend from the sphericity of the impacting drops.

3.1 FLOW REGIMES

Although the scenery has been already restricted to impacts onto deep liquid layers, the variety of phenomena which may occur is still so wide that several classifications have been proposed in the previous literature.

Impact parameters

As seen in the Section 1.3, three dimensionless numbers (*We*,

Fr, *Re*) may uniquely define the impact conditions of a drop impacting onto a deep pool. They are computed from the drop diameter D, the impact velocity V and the fluid properties (ρ, μ, σ). Here, as in most of the available literature, diameters ranges about from 1.5 mm to 3.5 mm, velocities about from 0 m/s to 4.5 m/s and the most used fluid has been distilled water. Having three parameters means that all the observed features may depend onto those three variables, which in turn depend mostly on velocity, since its range is wider than the ranges of the diameter or of the physical fluid properties. Thus, for reasons of simplicity, velocity has been chosen as reference variable to present the various typical drop impact phenomena. Starting from low velocity impacts, it is soon clear that, in the considered ranges, the Reynolds number has everywhere a high value, meaning that viscosities effects are negligibly small in comparison with inertial effects. For small velocities, Weber and Froude numbers have instead values close to unit, which increase with the square of velocity. This is the reason because in literature the phenomena arising from drop impacts onto a deep pool have been classified in a *We*-*Fr* space, neglecting the influence of viscosity. This is also the reason because there is a so wide gamma of phenomena, governed by a game where inertia, capillary and gravity effects all play a role. The smoothly effect of viscosity becomes important for smaller (micrometric) drops or for high-viscosity fluids.

Previous classifications

The various regimes arising after the impact of millimetric drops have been first divided in coalescence and splashing by Rodriguez and Mesler (1985). Rein (1996) presented an investigation on the transition region between coalescence and splashing, observing and describing a variety of phenomena. The same region was studied numerically by Morton et al. (2000) and experimentally by Liow (2001). Since the coalescing region is actually formed by a number of different phenomena, Fedorchenko and Wang (2004) called it composed regime. Cole (2007) further performed experimental observations on both the regions, producing the most recent map of the occurring phenomena. All these authors suggested some relations between *Fr* and *We* numbers in order to mathematically separate the regions. Here only phenomenological aspects will be presented, remanding to the related literature for further details.

New suggested classification

In the present section the phenomena arising from single drop impacts onto a deep pool will be presented following a new classification, composed of three main categories:

- coalescence;
- cratering;
- splashing.

It is based on the progressive importance of the main actors in the evolution of the impacts: passing from a class to the next, the phenomena characteristics of the previous class still may be present. For example the cratering region is characterized by the creation of a crater after the impact in the target fluid. However the same crater is present also in the splashing region, which is characterized by the additional ejection of secondary drops. This classification is only a useful tool to introduce the main typical aspects and transitions from a region to the following may not be stepwise.

3.1.1 *Coalescence regime*

Drop impacts in the coalescence region are characterized by phenomena deriving from the evolution of the impacting drop, while the target fluid remains almost in quiet. This regime may be characterized by:

- total coalescence;
- coalescence cascade;
- floating;
- (rolling);
- bouncing.

Floating and total coalescence

As shown in Figure 31, when the impact velocity is almost null, i. e. the drop is deposited gently onto the surface, it may float momentarily before it collapses into the bath due to gravity, as already observed by Reynolds (1881) and reviewed by Neitzel and Dell'Aversana (2002). Coalescence means that a thin film of the target liquid rises up the drop faster than the drop merges with the target fluid and Rayleigh (1879), Rayleigh (1882) and Thomson and Newall (1885) already reported several features of this phenomenon. The merger is generally delayed because the air layer between the droplet and the bath must first drain to a thickness at which Van der Waals forces between droplet and bath become important, approximately 100 nm (Charles and Mason, 1960a). The coalescence may take a number of distinct forms. Total coalescence arises when the entirety of the drop merges with the underlying reservoir.

Partial coalescence

Partial coalescence arises when only a fraction of the drop coalesces, leaving behind a smaller droplet that is ejected from the bath and bounces several times before undergoing itself a partial coalescence (Mahajan, 1930, Charles and Mason, 1960b, Thoroddsen and Takehara, 2000). Thus the coalescence process may take place in a cascade, where each step generates a smaller drop, as shown in Figure 32. This cascade is self-similar and up to six

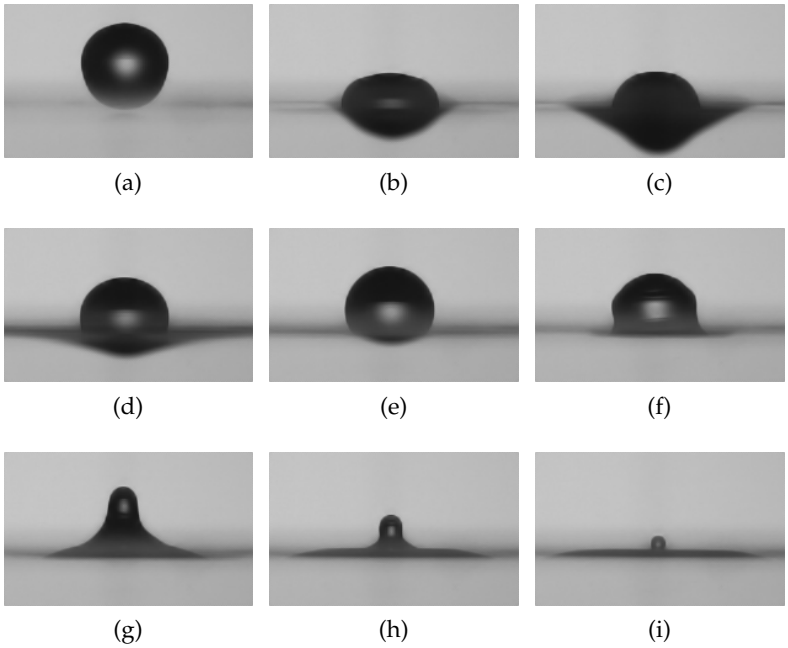

Figure 31: Drop impact in the coalescence regime.

steps have been observed. Each partial coalescence scales with the surface tension time scale and the cascade will not proceed ad infinitum because of viscous effects, which begin to be important for the very smallest drops. Thoroddsen and Takehara chose a limit of $Re = 20$ as the cutoff where viscous forces become dominant, while Aryafar and Kavehpour (2006) showed that for $Oh < 1$ drops fully coalesce but when $Oh > 1$ drops partially coalesce and a secondary drop is created. Blanchette and Bigioni (2006) demonstrated that partial coalescence is possible only if $Oh < 0.026$. Pikhitsa and Tsargorodskaya (2000) tried to explain the physical mechanism suggesting that the existence of the monolayer surfactant film is crucial for the multistage coalescence of the floating drop. Honey and Kavehpour (2006) observed that as the drop gets smaller, it bounces higher, under the main driving force of capillarity. The influence of viscosity on partial coalescence has been further examined by X.Chen et al. (2006), Gilet et al. (2007). A variety of novel partial coalescence events regarding droplets impinging onto a soap film have been reported in Gilet and Bush (2009).

Bouncing and rolling

If the impact velocity is a little increased the drop may bounce, Figure 33, and even roll (if the impact is not vertical) on the target surface, Figure 34. Then the drop still float before to coalesce (Jayaratne and Mason, 1964). Bouncing and rolling have been inserted in the coalescence regime even if they are not strictly related to the coalescence mechanism, because they end in a coalescence.

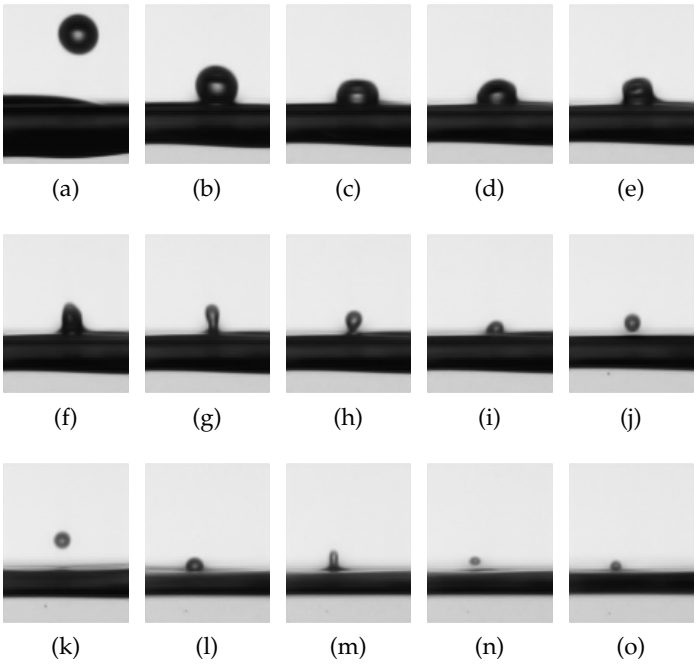

Figure 32: Coalescence cascade. The drop is a secondary droplet originated by a previous impact, which also originated the waves causing the obscuring of the region close to the interface.

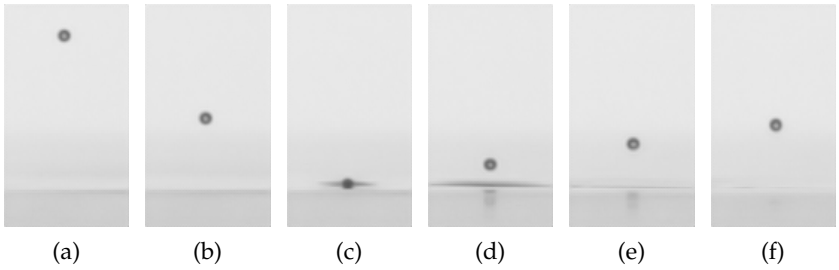

Figure 33: Drop impact in the bouncing regime.

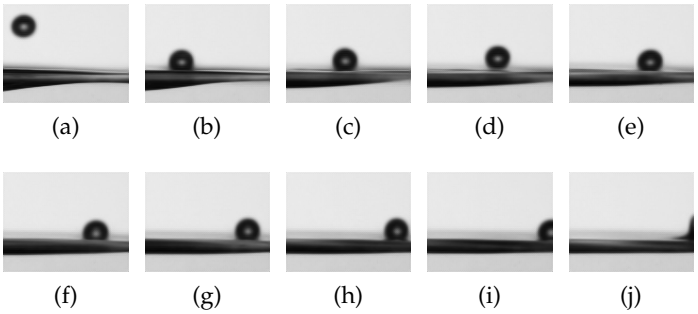

Figure 34: Rolling drop. The drop is a secondary droplet originated by a previous impact, which also originated the waves causing the obscuring of the region close to the interface.

3.1.2 *Cratering regime*

Drop impacts in the cratering regime are characterized by the evolution of the crater created in the target fluid, whose dimension becomes larger than that of the impacting drop. This tends to flatten on the bottom of the crater while coalescence is occurring. This regime may be characterized by:

- micro-entrapments;
- vortex rings;
- trampoline;
- micro-jetting;
- primary entrapment;
- thick jets;

Crater

While a crater is formed in the target liquid, a swell (a rather thick rim of displaced liquid) rises up on its base and propagates on the surface. The expansion of the crater is transitory because the surface tension arrests the downward motion of the liquid at a certain crater size, at which it collapses and the motion is reversed.The dynamics of how the cavity forms and collapses gives rise to a number of phenomena more strictly related with the evolution of the crater. At small impact velocity capillarity soon began to deform the expanding crater, restoring the plane free surface after several oscillations. At higher velocity the ejection of a Worthington jet[1] in the middle of the crater during the receding phase is observed. The crater size increases with the impact velocity and models for its maximum depth and its evolution have been proposed from a number of authors and will be treated in detail in Chapter 6. At small impact velocities its depth is grater than half of its width, due to a greater influence of surface tension. At higher velocity its shape is instead more hemispherical. In an intermediate region, due to the competition of the surface tension and inertia, sections of the crater walls merge during its collapse, resulting in entrapment of a big bubble in the bulk liquid. The first three phenomena of the cratering regime (micro-entrapments, vortex rings, trampoline) are indeed due to a superposition of coalescence and cratering mechanism, confirming that the transition is not step-wise.

Micro-entrapments

Apart from the compressibility effects, at the first stage of the impact, when the drop impacts onto the target liquid surface, many microbubbles may be entrapped in the bulk fluid (Blanchard and A.H.Woodcock, 1957, Esmailizadeh and Mesler, 1986, Peck and Sigurdson, 1994). This is due to a thin air sheet remaining trapped between the contacting surfaces, whose rupture

1 Sometimes it is called "Rayleigh jet".

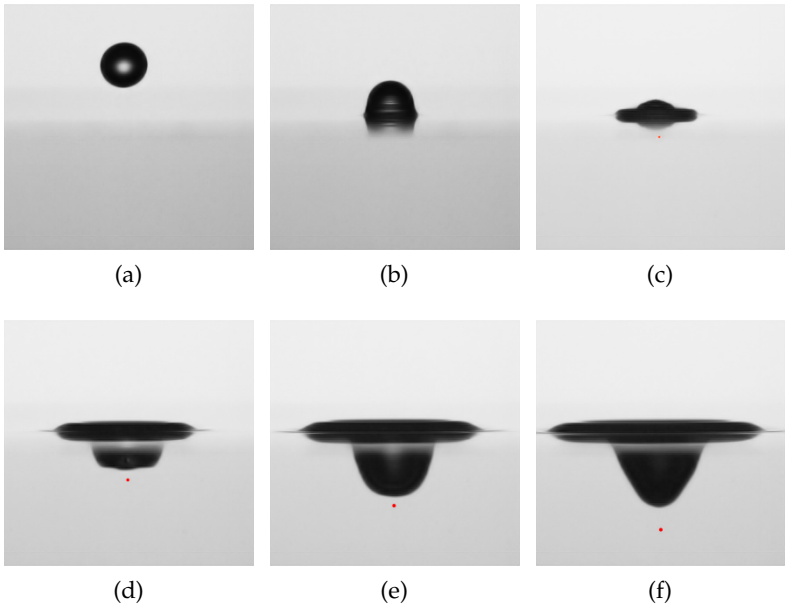

Figure 35: Drop impact with micro-entrapment of an air bubble. The bubble has been highlighted in red and a little enlarged for visualization purposes.

generates a number of bubbles, as found in a numerical analysis conducted by Oguz and Prosperetti (1989) and confirmed by experimental investigations of Sigler and Mesler (1990) and Thoroddsen et al. (2003). The air sheet is thicker for low impact velocities and its rupture leads to a variety of entrapment phenomena. Figure 35 shows an example in which only one main microbubble is entrapped. Once trapped the bubbles are often carried into the bulk fluid by a vortex ring generated by the coalescence of the impacting drop on the bottom of the crater (Durst, 1996).

Vortex rings

Drop-formed vortex rings, Figure 36, have been observed since Rogers (1858) and can be described as fluid spinning around a circle enclosed by a toroid, which travels downward and expands radially. Thomson and Newall (1885) was the first to observe a vortex ring in relation to drop impacts and proposed a model of formation based on viscosity and vorticity diffusion. Chapman and Critchlow (1967) suggested instead a model based on the pressure gradients resulting from the surface tension of the liquid, while Cresswell (1995) indicated a mechanism based on the generation of vorticity on relaxation of surface stresses at coalescence. The creation and evolution of a vortex ring, also because related to a number of fields, has been studied by many authors and a review can be found in Shariff and Leonard (1992).

Trampoline

The trampoline regime is a new phenomena detected thanks to the present experimental investigation. After the impact a cra-

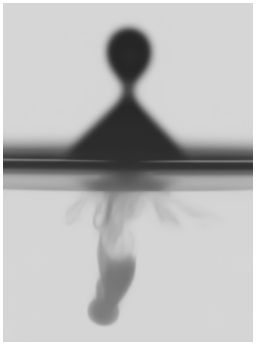

Figure 36: Drop impact with generation of a vortex ring. The visualization has been obtained dying the impacting drop.

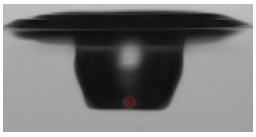

Figure 37: Coalescence cascade during the crater formation. A drop smaller then the impacting drop is floating on the bottom of the crater. The drop has been highlighted in red for visualization purposes.

ter is formed in the target liquid, while the impacting drop coalesce on its bottom. In the early stage of the coalescence a smaller drop may be formed, in a process similar to the coalescence cascade previously described. The new drop impacts on the bottom of the crater and does not have time to further coalesce in the target fluid, Figure 37, because it is designed away by the collapsing crater, which behave like a trampoline. This new phenomenon will be better described later, in Section 3.2.

Bubble entrapment

Impacts in the primary bubble entrapment regime, Figure 38, were first observed by Pumphrey and Walton (1988), who also related the generation of the bubble and its later oscillations to a substantial acoustic emission (Pumphrey et al., 1989), respect to all the other stages of the process, including the impact itself, which are relatively silent. Actually the relation between the sound emitted by the impact to the oscillations of bubbles entrapped into the bulk liquid was known since Franz (1959), but only with Pumphrey et al., who made the decisive innovation to photograph on the same frame both the physical event of drop impact and the trace of an oscilloscope driven by a hydrophone, the phenomenon has been well defined. The so called "underwater noise of rain" , whose understanding permits the detection and characterization of rain over the oceans by remote acoustic sensors, and its relation to drop impacts have been studied by a number of authors and it has been reviewed by (Prosperetti and Oguz, 1993). Oguz and Prosperetti (1990) suggested a relation of $We \sim Fr^{1/4}$ for the upper limit and of $We \sim Fr^{1/5}$ for the lower li-

mit of bubble entrapment and stated that whether or not a small bubble is formed beneath the crater depends on the exact timing of the reversal of the liquid motions in the various regions of the crater, founding that reversal of the liquid motions occurs latest at the bottom of the crater. Morton et al. (2000) described the mechanism as the result of capillary waves propagating through the cavity causing the collapsing walls to come together, while Liow (2001) showed a similarity between the initial upper portion of the crater with a Crapper wave. An analytical model was provided by Longuet-Higgins (1990) using potential theory. The effect of viscosity was investigated by Deng et al. (2007), exhibiting a shift in the inviscid bubble entrapment limits, whereas, at the impact crater, the local effect was seen as a weakening of the capillary wave, which is responsible for bubble pinching, and a weakening of the intensity of crater rebound. Deng et al. showed how the phenomenon can be captured well by the capillary number. As found by Rein (1996) and confirmed by Elmore et al. (2001), also more than one bubble can be entrapped into the bulk liquid.

Influence of the drop shape

It is important to point out that the drop impact phenomena may be influenced by the shape of the falling drop. The simplifying assumption of a spherical shape may not perfectly represent the reality in some cases. At small falling height dissipation has not enough time to damp the oscillations of the drop caused at its detachment, while at high falling velocity viscous stresses may deform the sphericity of the shape and cause internal circulation. Also the size of the drop has a strong influence, because of the relation between pressure and curvature (Young-Laplace equation). In the end, when the drop strikes the target surface, its shape may be described as a sphere or as a prolate or oblate spheroid. These variations may obviously have an effect on the phenomena arising from the impact. For example Chapman and Critchlow (1967) confirmed the existence of an optimum falling height, related to the time of drop oscillations, for the creation of vortex rings and stated that they are formed best if the drop is spherical and changing from an oblate to a prolate spheroid at the moment of contact with the bath. Liow (2001) observed that prolate drops do not entrap bubbles.

Microjetting

In the primary bubble entrapment region, the collapse of the crater generates two jets: one downward, into the bulk liquid, accompanying the entrapped bubble, and one, very thin and fast, ejected upward. The first, predicted by the analytical model of Longuet-Higgins (1990), was observed by Rein (1996) and Elmore et al. (2001). The second, Figure 39, first observed by Hallett and Christensen (1984), was thought by Rein (1996) only occurring after an air bubble had been entrapped under the liquid surface, in a mechanism of radial focusing. This was dis-

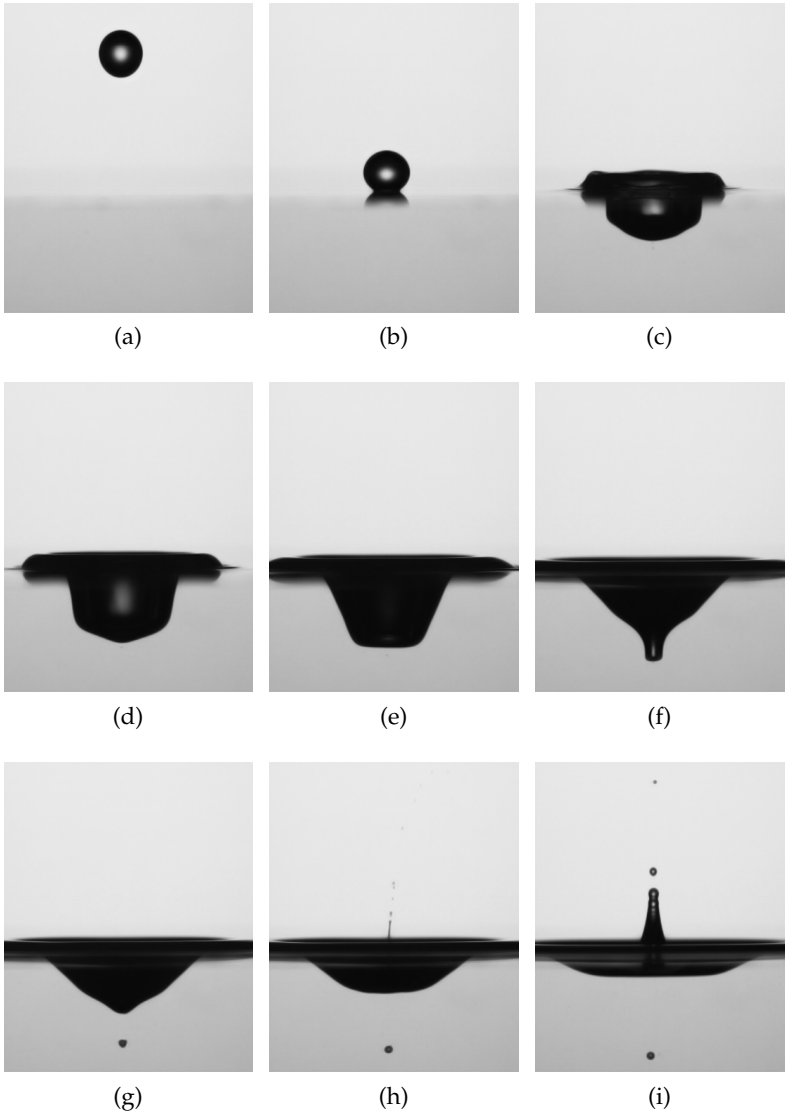

(a) (b) (c)

(d) (e) (f)

(g) (h) (i)

Figure 38: Drop impact with primary entrapment.

claimed by Liow (2001), who observed the same jet in a region, which called of pre-entrapment, where bubbles are not entrained. Deng et al. (2007) suggested that the thin jet being similar to the hydraulic jets produced by the collapse of free-surface standing waves. This jet is an example of a finite-time singularity, where the continuum description starts to break down, and several examples may be found in nature, as reviewed by Brenner (2000). Zeff et al. (2000) demonstrated that the shape of the liquid-air interface develops an extremely high curvature an instant before the jet is produced. The release of this curvature produces the jet. They showed this singular event being driven by the inertia and surface tension of the fluid, and ultimately stopped by the retarding influence of viscosity. The formation of a small vortex ring that forms at the very base of the cavity has also been observed in connection with the pre-entrapment jetting.

Thick jets

At higher impact velocities the jets are thicker, Figure 40 and they have been observed since Worthington (1908) in a region previously called of post-entrapment. The jet rises up above the free surface and usually breaks up into one or more secondary drops. Some of the only quantitative data on the height development of the jet with increasing Froude number comes from Liow (2001), while Fedorchenko and Wang (2004) have attempted to model the thick jet formation with an energy balance. Cole (2007) observed small vortex rings be formed only in the first region of post-entrapment and than disappear.

3.1.3 *Splashing regime*

Drop impacts in the splashing regime are characterized by the formation of secondary droplets from the periphery of the impact. This criterion is different from the definition given by Rodriguez and Mesler (1985), who used the appearance of a central jet from the crater bottom as a criterion for splashing. The same choice was used by Rein (1996) in view of the fact that after a drop impact either a central jet or a vortex ring will occur but not both of them. The jet criterion thus should distinguishes between the two main characteristic features of drop impact into liquids. However later works have revealed a number of other phenomena and vortex rings have been observed also in presence of jets. For this reason a criterion in continuity with the definition of splashing on solid surfaces is retained more significative. The splashing regime may be characterized by:

- prompt splashing;
- late splashing;

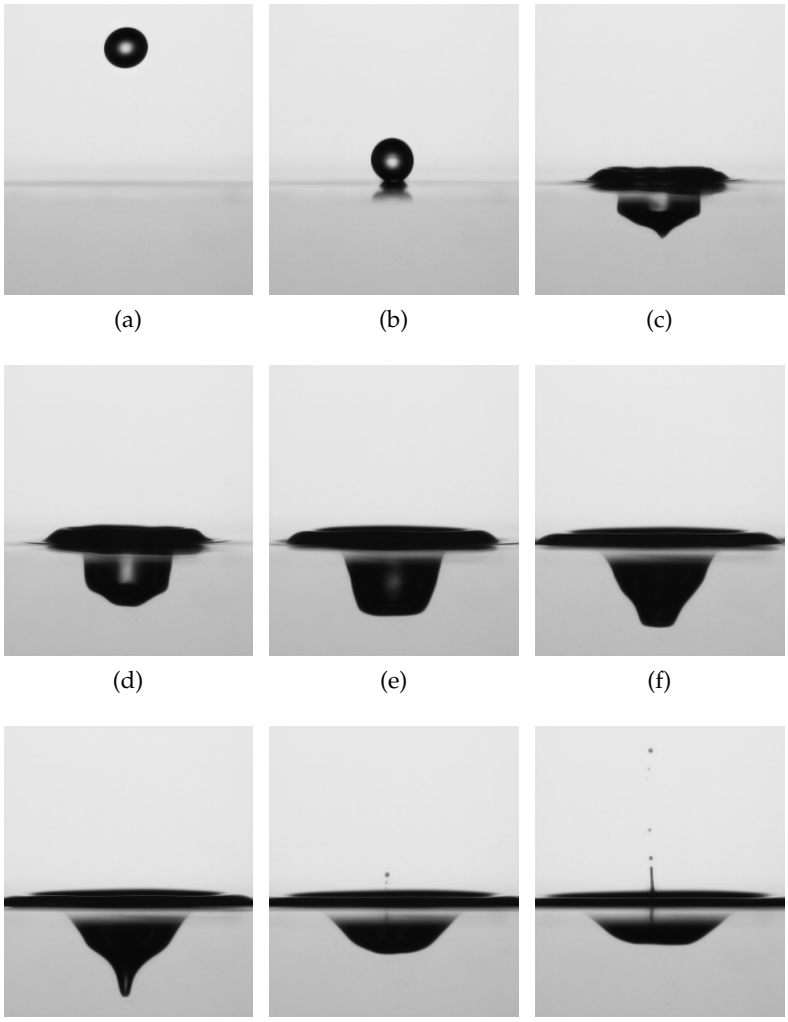

Figure 39: Drop impact in the micro-jetting regime.

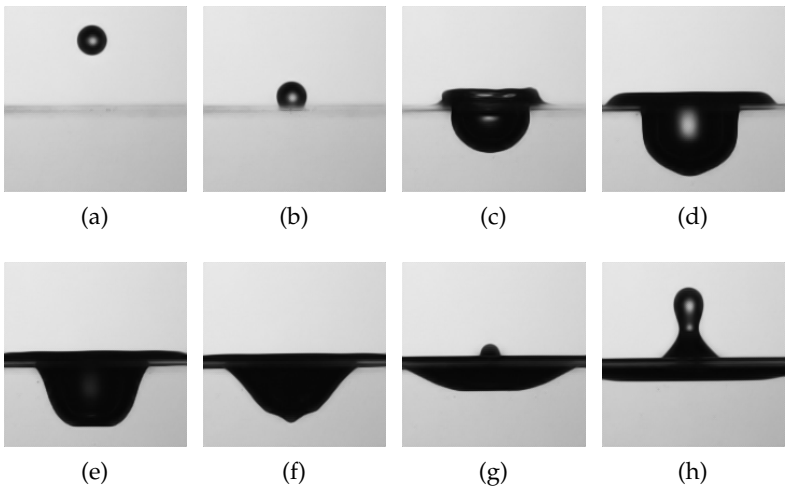

Figure 40: Drop impact in the thick jet regime.

- secondary entrapment;
- domes.

The outcome of the splashing is probably the most fascinating and still unknown phenomenon of drop impacts. Deegan et al. (2008) reported a description of their complexity, illustrating the main stages of splashing. First, a cylindrical fluid sheet shoots out from the layer, forming a fat rim. Second, cylindrical symmetry is broken by a linear instability of the rim, which selects a preferred wavelength at which the thickness of the rim varies periodically. Third, in a nonlinear stage of the original instability, the rim develops tips, from which jets emanate. Fourth, drops pinch off from the end of each jet. There are at least two types of sheets, of completely different physical origin, produced when the drop hits the fluid layer. The former, first predicted by numerical simulations of Weiss and Yarin (1999) and than observed by Thoroddsen (2002), shoots out horizontally from the neck region, where the contact between the impacting liquid drop and the liquid pool occurs, and contains equal amounts of drop and layer fluid. The second, first described by Peregrine (1981), travels outwards over the surface after the drop has penetrated the layer. Than the two sheets may interact in different ways.

Prompt splashing

The formation of secondary droplets starts in the very early stage of the impact. Than the setting up of the instability may be further sustained or may be dumped down. Figure 41 shows the difference between two impacts just below and just above the splashing limit. It can be noticed the absence of fingers on the wave swell, but the presence of small secondary droplets produced only in the very early stage of the impact. Cossali et al. (1997) found the dimensionless group $K = WeOh^{0.4}$ being the discriminating variable of the splash onto thin films: splashing occurs when K is greater than a critical value (function of the film thickness). Further details on splashing onto dry surfaces or thin liquid films may be found in a recent review of Yarin (2006).

Crown and late splashing

Increasing further the impact velocity, a thin liquid cylindrical sheet may raise up from the wave swell, with fingers on its top from which secondary droplets may detach. The shape is very characteristic and it is referred as a crown. Figure 42 shows a comparison among swell and crown formations at increasing velocity impacts. Yarin and Weiss (1995) made a significant step in understanding the mechanism of crown propagation. He described the crown as a kinematic discontinuity, predicting the square root temporal growth of the crown radius. This theory has been extended to take into account the viscosity by Trujillo and Lee (2001) and generalized by Roisman and Tropea (2002) to inclined and multiple impacts.

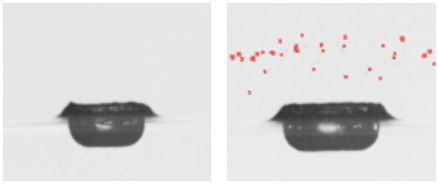

(a) (b)

Figure 41: Comparison between an impact without splashing (a) and with splashing (b). In the second case there is a production of secondary droplets from the periphery of the impact at the very early stage. Secondary droplets have been highlighted in red for visualization purposes. ((a): Water, $D = 2.0\,\mathrm{mm}$, $V = 2.4\,\mathrm{m/s}$, $We = 148$, $Fr = 287$, $Re = 5707$. (b): Water, $D = 2.5\,\mathrm{mm}$, $V = 2.4\,\mathrm{m/s}$, $We = 191$, $Fr = 234$, $Re = 7264$).

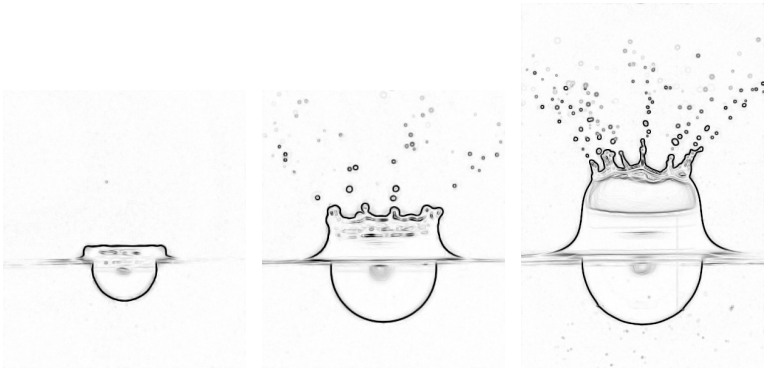

(a) (b) (c)

Figure 42: Drop impact onto a semi-infinite liquid target at increasing Weber numbers. Edges have been highlighted. (a): Only a liquid swell is formed above the target surface. (b): The liquid swell takes the shape of a crown. (c): A thin liquid sheet raises up from the crown. ((a): Water, $D = 2.2\,\mathrm{mm}$, $V = 2.4\,\mathrm{m/s}$, $We = 171$, $Fr = 262$, $Re = 6385$. (b): Water, $D = 2.8\,\mathrm{mm}$, $V = 4.2\,\mathrm{m/s}$, $We = 688$, $Fr = 619$, $Re = 14\,624$. (c): Acetic acid, $D = 2.7\,\mathrm{mm}$, $V = 4.2\,\mathrm{m/s}$, $We = 1893$, $Fr = 661$, $Re = 11\,529$).

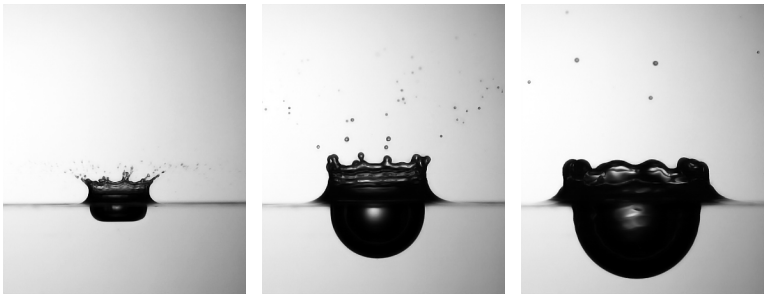

(a) $t = 1.3$ ms (b) $t = 4.3$ ms (c) $t = 10.4$ ms

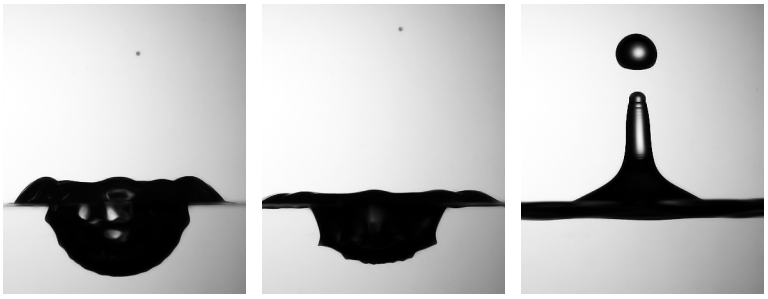

(d) $t = 22.6$ ms (e) $t = 28.7$ ms (f) $t = 78.8$ ms

Figure 43: Drop impact in the splashing regime. (Water, $D = 2.8\,\text{mm}$, $V = 4.2\,\text{m/s}$, $We = 688$, $Fr = 619$, $Re = 14\,624$).

The crater and the crown reach their maximum size at about the same time. Then the crown begins to fall down, generating capillary waves which travel to the bottom of the receding crater. Many capillary waves have been observed traveling down on the growing crater when it is reaching its maximum depth, giving it the shape of a cut-glass goblet (Shin and McMahon, 1990), which can be see in Figure 43d.

Secondary entrapment

At higher velocity, the impact may again entrap air bubbles in three ways. The first is due to a train of non-linear capillary traveling downward to the bottom of the receding crater, as showed in Figure 44. It is named secondary bubble entrapment after Liow (2001) and was investigated by Tomita et al. (2007). At still higher velocity it may happen that the base of the cavity spreads out into a dish-shape which then detaches from the cavity to form a very distorted bubble, as only reported by Pumphrey and Elmore (1990). The third way is due to the formation of a toroidal bubble over the crater by the crown.

Domes and toroidal bubbles

At even higher velocities, the thin liquid sheet may rise up further and possibly neck in, forming a dome above the crater, as showed in Figure 45. A downward jet is then formed, which falls down to the raising crater and may or may not intersect it and encapsulate one or more air bubbles in the target liquid. Successively the crater and the liquid sheet reach an equilibrium configuration with a shape similar to a toroidal bubble, Figure 45,

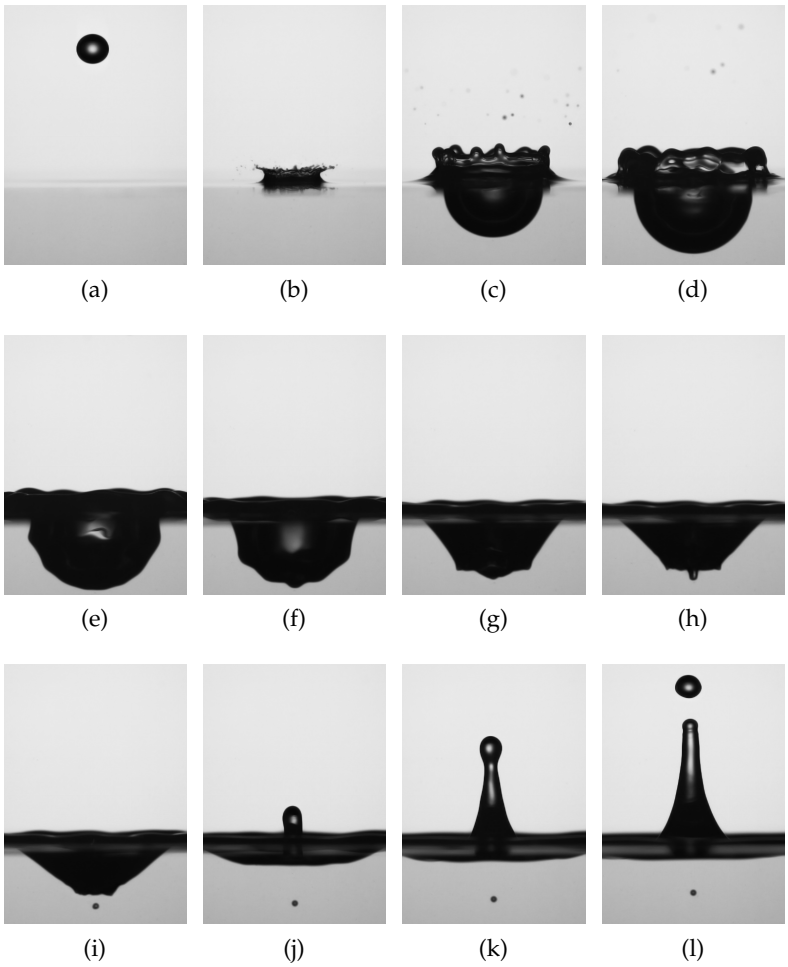

Figure 44: Drop impact in the secondary entrapment regime. (Water, $D = 2.1\,\mathrm{mm}$, $V = 3.6\,\mathrm{m/s}$, $We = 360$, $Fr = 629$, $Re = 9127$).

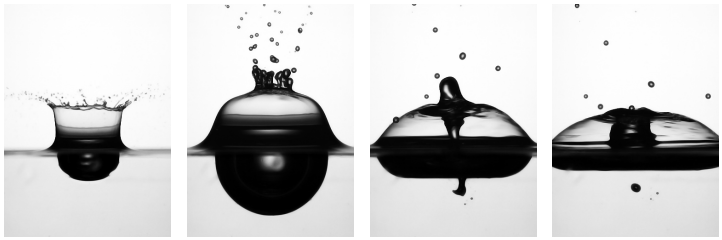

(a) (b) (c) (d)

Figure 45: Drop impact onto a semi-infinite liquid pool with formation of a toroidal bubble above the target surface and the entrapment of a bubble in the pool. (Acetic acid, $D = 2.9\,\text{mm}$, $V = 4.4\,\text{m/s}$, $We = 2177$, $Fr = 691$, $Re = 12\,642$).

which is maintained briefly until it is broken by instabilities. In this case capillary waves have not been observed on the crater. Domes-like bubbles, as a result of drop impacts, where first experimentally observed by Worthington (1908), who explained the constriction of the mouth of the bubble-thin cylindrical envelope in terms of surface tension. However, since the phenomenon is quite large and long, everybody can noticed it in puddles when it is raining. Its relation with rain is confirmed by the report of this phenomenon in a number of studies dealing with drop impacts at terminal velocity, mainly related to phenomena of erosion or sound production (Franz, 1959, Mutchler and Hansen, 1970, Hallett and Christensen, 1984, Snyder, 1990). Only Engel (1966) performed measurements of the bubble height, obtaining an asymptotic value of two times the drop diameter.

Terminal velocity

The falling velocity of an object in the vacuum is independent from its mass or shape. However, when a liquid drop falls in atmospheric conditions, aerodynamics drag takes more and more influence increasing drop sizes and falling velocity and it may result in a deformation of the drops or even in their fragmentation, justifying the wide spectra of diameters measured during rain, as shown by a recent study of Villermaux and Bossa (2009). Apart from fragmentation cases, the falling drop accelerates until it reaches a terminal constant velocity, where gravity is balanced by aerodynamics drag. The terminal velocity has been usually measured and reported as a function of the drop diameter (Laws, 1941, Spilhaus, 1948, Gunn and Kinzer, 1949, Dingle and Lee, 1972).

High speed impacts

Experiments on drop impact at terminal or high speed velocities have been performed by several researchers with impressive test rigs of heights up to 26 m, sometimes in reduced pressure conditions, which require special solutions to maintain constant the impact pool level, like with a constant head or with water onto ice (Hallett and Christensen, 1984). In order to increase fur-

ther the impact velocity, different strategies have been used, as vertically firing the impact pool against a suspended drop (Jenkins, 1967) or using vertical wind tunnel to accelerate the falling drop (Hallett and Christensen, 1984).

Additional complexities

Obviously many other parameters may be added to the cases explained above and few studies have been presented in literature. Manzello and Yang (2002) examined drop impingements onto liquid surfaces consisting of a different fluid, in order to get information from a fire-suppression perspective. Non vertical impacts have been investigated by Jayaratne and Mason (1964), Leneweit et al. (2005), Okawa et al. (2008). The presence of a surfactant may have a more complicated effect than to simply lower the surface tension because of the time taken for the surface film to spread over newly formed surfaces Rayleigh (1890).

Common features

Several of the cited phenomena are not limited to drop impacts, but are observed also in other circumstances. For example the closure of the rising cylindrical liquid sheet generated by the impact has been observed in microgravity experiments of projectile impacts onto liquid surfaces (Holfeld et al., 2008), where obviously inertia and surface tension effects are dominant upon gravity. Another example is the jet ejection by the collapsing crater, which can be observed also in case of object impacts onto liquid surfaces (Bergmann et al., 2009) or in other situations where a interface curvature of liquid reverses violently, as in (Antowiak et al., 2007).

3.2 A FLUID TRAMPOLINE

In the cratering regime, before the micro-jetting, a new phenomenon has been observed in the present investigations. It is due to a superposition between the partial coalescence and the formation of a crater. At low impact velocities a series of capillary waves propagate up the impacting drop. The capillary waves can converge at the top of the drop to pinch off a small secondary drop before the drop has completely flattened and coalesced on the bottom of the growing crater. As shown in Figure 46, the the secondary drop falls onto the bottom of the crater and may completely coalesce or may bounce or float on the bottom of the crater. In the second case it is ejected by the receding crater, which acts like a fluid trampoline, in a manner similar to that described by Gilet and Bush (2009). This behavior seems to be facilitated by a prolate shape of the impacting drop.

The ejection of a solitary drop was already observed by Cole (2007), who described two different zones of jetting. In the first the base of the crater has a low curvature and collapses to produce a single slow moving drop. In the second the crater exhi-

Case	D (mm)	V (m/s)	We	Fr	Re
a	2.88	4.42	2207	691	12 770
b	2.95	4.39	2227	666	12 979
c	2.86	4.41	2177	691	12 642

Table 5: List of impact parameters for the three reference cases in the analysis of the impacts producing domes-like bubbles.

bits a sharper curvature and collapses producing several high velocity drops. However the images of the present studies reveal that the ejected drop is not produced by the jet, but from a process of partial coalescence. In the present investigation the partial coalescence superposed to cratering have been observed for $We \sim (40 - 70)$ and $Fr \sim (50 - 110)$.

Other situations may arise from the partial coalescence of the impacting drop. In Figure 47 it can be seen, on the bottom of the main crater, the profile of a secondary crater, produced by the impact of the secondary drop. In Figure 48 it can be noticed the ejection of two drops. The first is due to a trampoline phenomenon, the second comes from the jet. Thus this last impact is in a region of superposition between the trampoline and the micro-jetting regimes.

3.3 DOME FORMATION AND TOROIDAL BUBBLES

Thanks to the use of acetic acid instead of water it has been possible to obtain impacts with higher Weber numbers. However the use of an acid has caused some problems because of the test rig was not designed to work with acids and only few impacts have been recorded. Pure water-free acetic acid, usually called glacial acetic acid, has been used. It has a superficial tension almost three times lower than water, while having a higher density and viscosity (Table 1). Thus, other things being equal, it allow to obtain impacts with Weber number almost three times higher than water, while Froude number remain almost unchanged. Three impacts have been selected and their impacts conditions have been reported in Table 5. They have been chosen because they show a different behaviors of the crown even if the impact condition are very similar. As can be see in Figure 49, cases *b* and *c* present the phenomena of dome-like superficial bubble, already described in Section 3.1.3, while case *a* do not have the closure of the crown. Moreover, case *c*, present also a bubble entrapment.

After the drop impact a crown is soon formed and many lit-

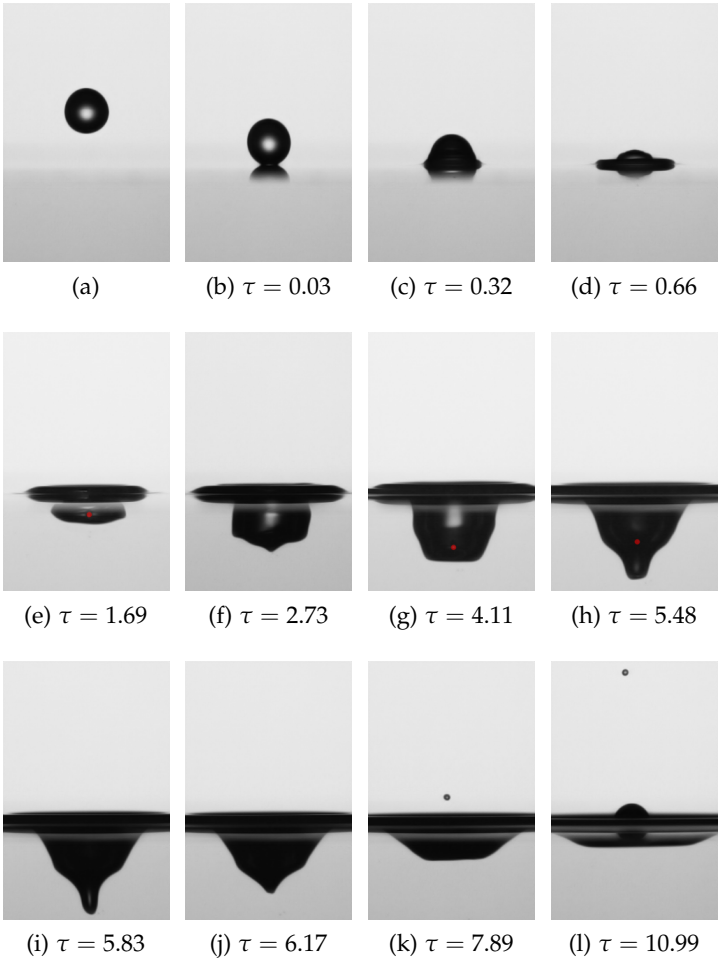

(a) (b) $\tau = 0.03$ (c) $\tau = 0.32$ (d) $\tau = 0.66$

(e) $\tau = 1.69$ (f) $\tau = 2.73$ (g) $\tau = 4.11$ (h) $\tau = 5.48$

(i) $\tau = 5.83$ (j) $\tau = 6.17$ (k) $\tau = 7.89$ (l) $\tau = 10.99$

Figure 46: Drop impact in the trampoline regime. The smaller drop originated from the impacting drop in a process of coalescence cascade has been evidenced in red for visualization purposes only when it was visible in the original images. (Water, $D = 2.8\,\mathrm{mm}$, $V = 1.24\,\mathrm{m/s}$, $We = 54$, $Fr = 52$, $Re = 4099$).

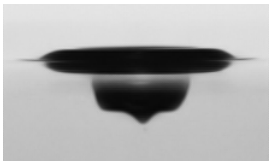

Figure 47: Example of a secondary crater in the trampoline regime. (Water, $D = 2.3\,\mathrm{mm}$, $V = 1.2\,\mathrm{m/s}$, $We = 45$, $Fr = 65$, $Re = 3409$).

Figure 48: Example of a double drop ejection in the trampoline regime. (Water, $D = 2.8\,\mathrm{mm}$, $V = 1.2\,\mathrm{m/s}$, $We = 55$, $Fr = 53$, $Re = 4150$).

tle droplets are designed away by prompt splashing. The liquid sheet forming the crown is initially crooked externally, with a great number of small fingers. It then evolve to a cylindrical shape, on which a rim of liquid is formed. The number of fingers decrease and their thick increase, as well as the size of the ejected drops, whose direction rotates from horizontal to vertical.

In all the three cases under investigation, in the early stage of the impact, two rings of small bubbles are formed below the crater, one above the other, but problems of resolution make hard to see them from the printed images of Figure 49. Then these two rings stand on the side of the crater at two different heights, creating on it the two edges barely visible in the third images of Figure 49.

The crowns of the cases *b* and *c* are thinner and raise faster than in the case *a*. At about $\tau \sim 6$ the rim on the top of the crowns start contracting. This reduction is very slight for the case *a*, where the wall of the crown remain plain, while assuming a conical shape. It is instead very pronounced for the cases *b* and *c*, where the walls of the crown are blended internally, toward the symmetry axis. The number of fingers still decreases and their thickness increases, until they meet on the symmetry axis forming like a plume on the just formed dome-like bubble. below the plume a downward jet formes and falls down, impacting onto the jet rising up from the bottom of the crater, giving a toroidal shape to the bubble. In case *c* the curvature of the top of the bubble is more pronounced and the downward jet falls down earlier and with greater velocity, going to intersect the raising crater and encapsulating in it a bubble. Than both cases *a* and *b* assume again a similar shape which is in the end broken by instabilities. In the case *b* the open conical crown falls down

	a	b	c
D_{hor} (px)	51	50	48
	52	49	49
	51	50	49
	51	50	49
D_{ver} (px)	44	49	47
	45	48	47
	45	49	46
	45	49	46

Table 6: Horizontal and vertical diameter (in pixels) of the falling drop in the four frames previous the impact for the three cases of Table 5.

in a little internal circular region of the crater, changing its shape. In the end a big jet raises up from the center of the crater.

Shape of the impacting drops

Since impact conditions are very similar, the reason of a different behavior of the crown has been researched in the shape of the impacting drop. An image analysis of the last five frames previous of the impact has revealed, as shown in Table 6, how the closure of the crater to form a dome (cases *b* and *c*) is related to a better sphericity of the impacting drop, while in case *a* its shape in more oblate. A better sphericity of the impacting drop seems to determine a higher efficiency and regularity in the ejection of the crown. The difference between cases *b* and *c*, i. e. the entrapment of the drop may be explained with the differences existing in the related Weber and Froude number. As reported in Table 5, case *c* has a lower Weber number and a higher Froude number, which may explain the earlier and faster bending of the crown due to a retarded effect of gravity and a earlier effect of surface tension.

Measurements

Figure 50 shows the evolution in time of the dimensionless crater depth, evidencing how the closure of the crown has only a little influence on its maximum, even if it is a little smaller for the related cases *b* and *c*. Figure 51 shows the crown reaching its maximum height earlier than the crater. This time is smaller for the case *c*, for which it was noticed above a better efficiency in crown formation. Measurements on the crown have been performed considering its top external points and without consider the plume formed in the cases *a* and *b*. Oscillations in the results are due to the fact that the crown has not a well defined profile, but, because of fingers, it presents a very indented edge. The ratio between the dimensionless crown height and crater depth is plotted in Figure 52, evidencing a difference between the cases

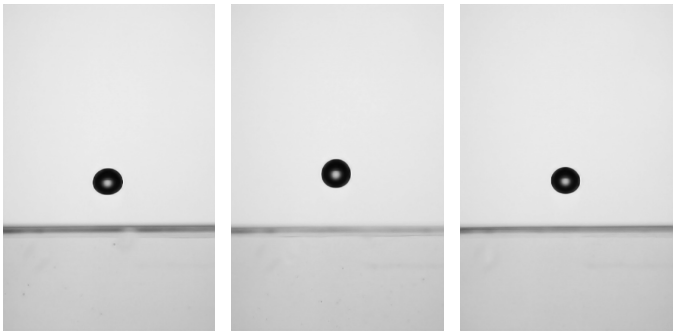

(a1) (b1) (c1)

(a2) $\tau = 2.5$ (b2) $\tau = 2.1$ (c2) $\tau = 2.5$

(a3) $\tau = 3.7$ (b3) $\tau = 3.3$ (c3) $\tau = 3.7$

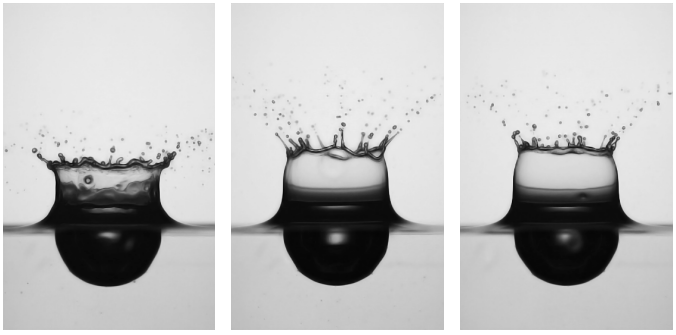

(a4) $\tau = 7.4$ (b4) $\tau = 6.9$ (c4) $\tau = 7.4$

Figure 49: Continue...

(a5) $\tau = 13.5$ (b5) $\tau = 14.0$ (c5) $\tau = 13.6$

(a6) $\tau = 25.7$ (b6) $\tau = 25.9$ (c6) $\tau = 25.9$

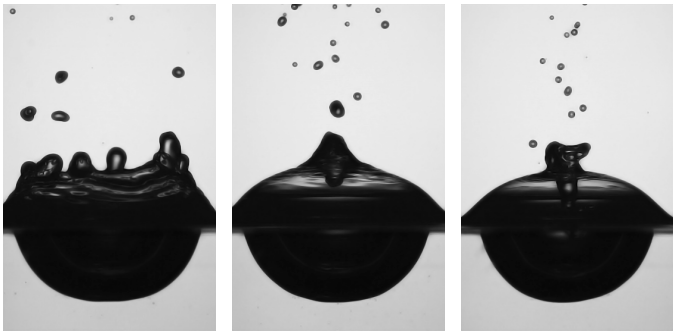

(a7) $\tau = 45.3$ (b7) $\tau = 44.9$ (c7) $\tau = 44.4$

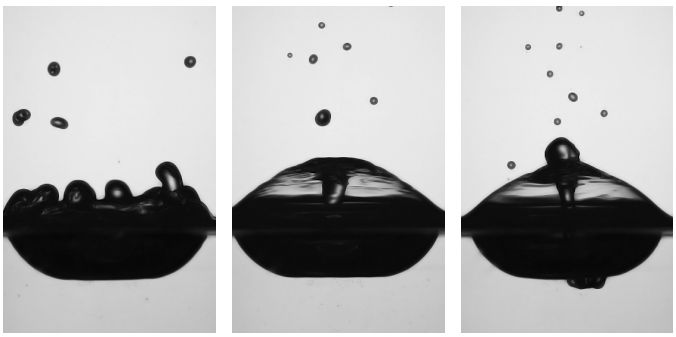

(a8) $\tau = 57.6$ (b8) $\tau = 57.9$ (c8) $\tau = 58.0$

Figure 49: Continue...

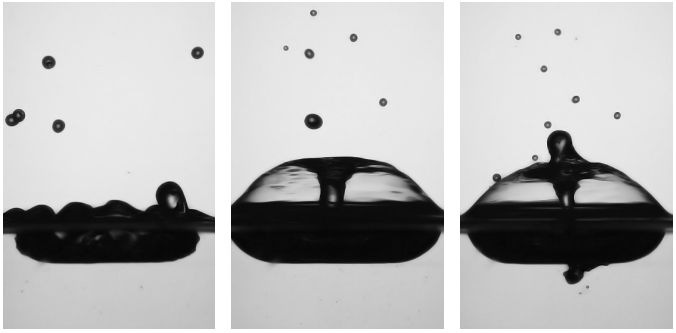

(a9) $\tau = 66.2$ (b9) $\tau = 66.2$ (c9) $\tau = 66.7$

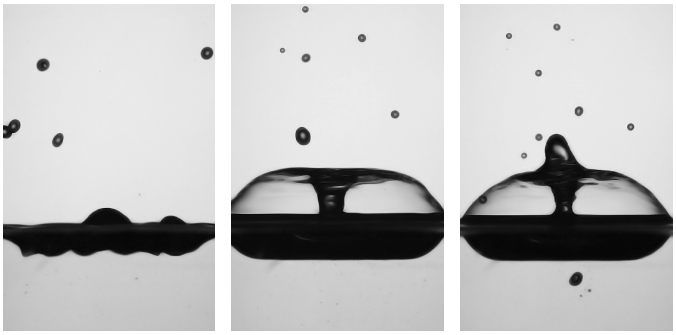

(a10) $\tau = 76.0$ (b10) $\tau = 75.7$ (c10) $\tau = 75.3$

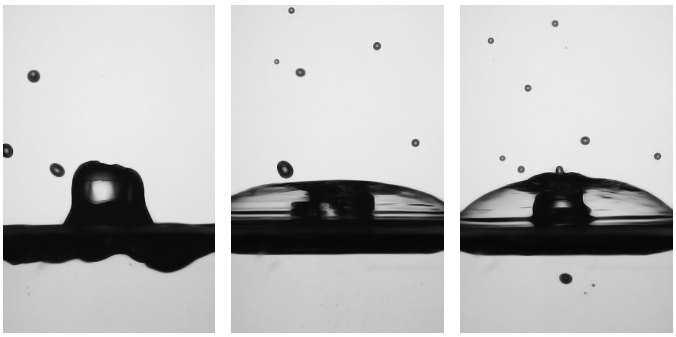

(a11) $\tau = 91.9.7$ (b11) $\tau = 92.3.$ (c11) $\tau = 92.6$

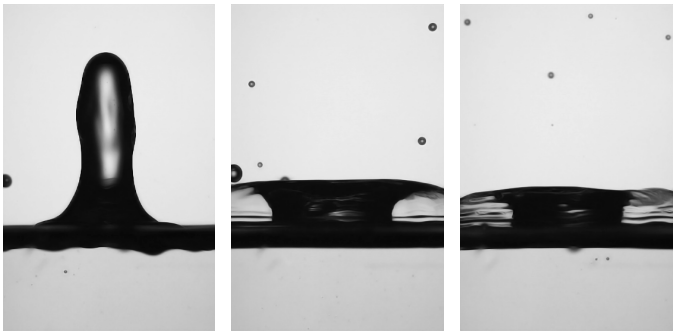

(a12) $\tau = 142.1$ (b12) $\tau = 142.2$ (c12) $\tau = 142.0$

Figure 49: Drop impacts with dome formation. The three columns represent respectively cases *a*, *b* and *c* of Table 5.

with or without dome. In the first case the height of the crown is soon greater than the crater depth and then decrease, while in the second case the height of the crown is initially smaller that the depth of the crater, but ratio increase till both reach the same size at about $\tau = 18$, when, curiously, also the height of the crowns presenting dome formation have the same size of the related crater.

Figure 53 shows the evolution in time of the dimensionless crater width, evidencing how the closure of the crown has only a little influence on its maximum, even if it is a little smaller for the related cases *b* and *c*. The great differences in Figure 54 are due to the dome formation, where, as already noticed above, case *c* have a earlier and faster closure motion.

Figure 55 shows how in all the three cases the diameter of the top of the crown are smaller than the diameter of the base of the crater. This is obvious for cases *b* and *c*, which reach the closure, but is still valid also for case *a*. This leads the crown to fall inside the crater, changing its shape in the region close to the interface, as shown in Figure 49b.

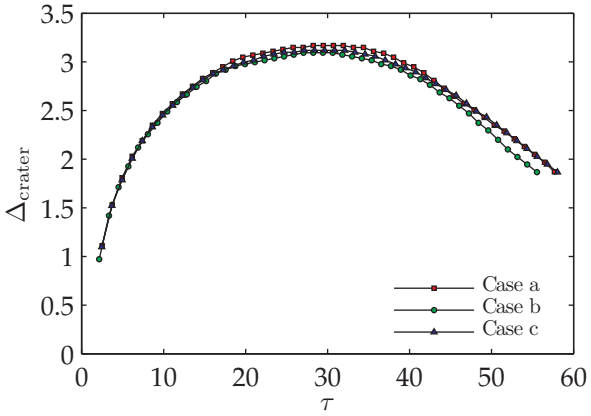

Figure 50: Dimensionless crater depth as a function of dimensionless time for the three cases of Table 5.

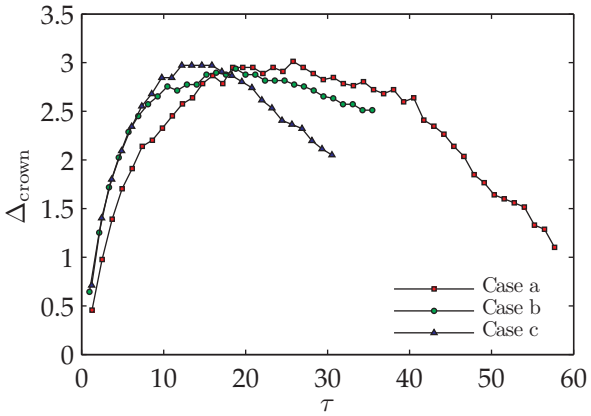

Figure 51: Dimensionless crown height as a function of dimensionless time for the three cases of Table 5. The plume of the crown (cases *a* and *b*) has not been considered.

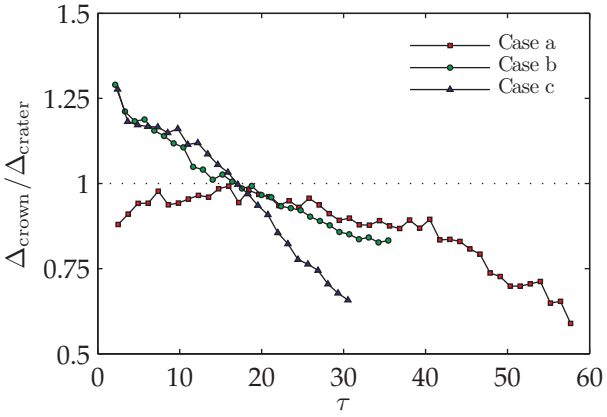

Figure 52: Ratio between the crown height and crater depth as a function of dimensionless time for the three cases of Table 5.

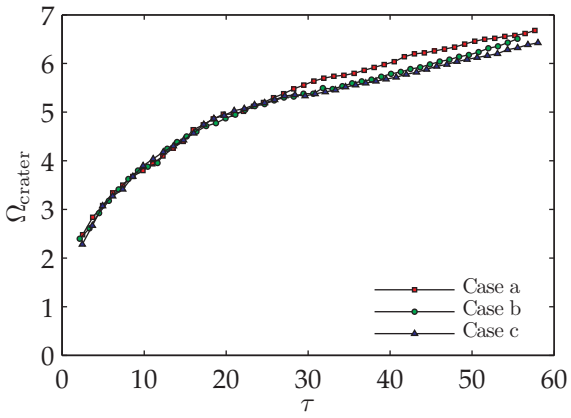

Figure 53: Dimensionless crater width as a function of dimensionless time for the three cases of Table 5.

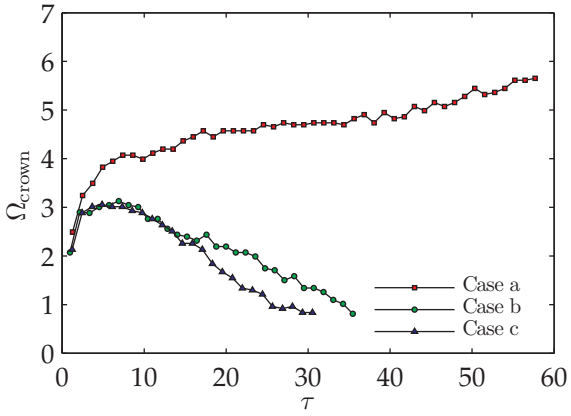

Figure 54: Dimensionless crown top width as a function of dimensionless time for the three cases of Table 5.

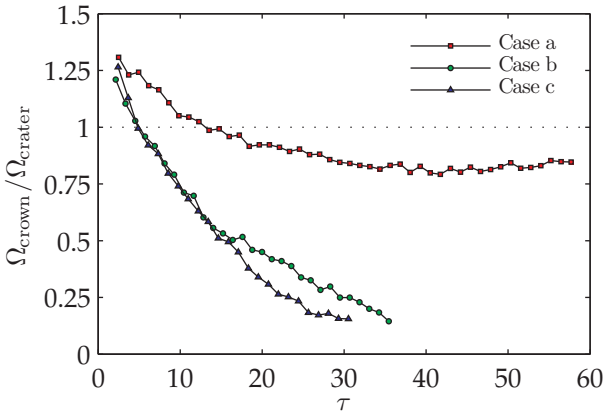

Figure 55: Ratio between the crown top width and crater width as a function of dimensionless time for the three cases of Table 5.

4

DOUBLE DROP IMPACTS ONTO A DEEP POOL

As explained in Chapter 1, the investigation of multiple drop impacts is a necessary step to the extrapolation of results from drop to spray impacts. The only studies published in previous literature are related to double drop impacts onto dry surfaces or thin liquid layers.

Literature review

Roisman et al. (2002) observed experimentally and described theoretically the impact of two drops onto a dry substrate and their interaction, obtaining a remote asymptotic solution for the velocity, the thickness, and the shape of the uprising liquid sheet, formed from the collision of the two spreading lamella, for inertia dominated impacts. Cossali et al. (2003, 2004a,b, 2005, 2007) connected the rising of this liquid sheet with the existence of a third splashing mechanism (after prompt and late splashing), in competition with, but less efficient than late splashing. They experimentally investigated the simultaneous impact onto heated dry surfaces and thin liquid layers of three drops, as this was considered, due to the symmetry of the configuration, the most useful and simple form to obtain first information on the drop-drop interaction processes. With impacts onto dry surfaces, they observed the crown interaction producing splashing also for impact conditions under which single drop impact would not give rise to splash, lowering the splashing threshold. With impacts onto liquid films this mechanism of secondary atomization is rather in competition with crown-splashing and quantitatively less efficient.

Additional parameter

Here the study of multiple drop impacts is extended considering impacts onto a deep pool. As explained in Section 1.3, only the simultaneous impact of two identical drops will be considered, since this allows to introduce into the problem only one more parameter respect to the single impact case (which is defined by the Weber, Froude and Reynolds numbers), i. e. the distance L between the two impacting drops, which is non-dimensionalized with the drop diameter:

$$\tilde{L} = \frac{L}{D} .$$

The minimum limit dimensionless drop distance is $\tilde{L} = 1$, which means that the surfaces of the two falling drops are tangent. However, in this situation, the action of short distance forces would cause the coalescence of the two drops. Therefore this minimum

case	D (mm)	V (m/s)	We	Fr	Re	$\tilde{L}$
a	2.8	1.9	134	127	6486	2.0
b	2.15	2.0	120	180	5265	1.9
c	2.5	2.1	148	175	6457	1.8
d	2.4	2.1	150	187	6396	2.2
e	2.4	2.1	151	187	6423	2.2
f	2.4	2.1	146	186	6480	2.3
g	2.7	2.1	159	167	6888	2.8
h	2.7	3.0	322	336	9818	3.0
i	2.6	3.0	320	337	9763	3.1
l	2.6	3.6	484	515	11 970	4.3

Table 7: List of impact parameters of the selected cases of double drop impacts. Figures have been reported at the end of the present section.

distance is only a limit, it may represent only a transient configuration and in all the present experimental data $\tilde{L} > 1$.

Selected cases

As explained in Section 2.1.1, due to some problems of repeatability and control of the impact parameters for the simultaneous double drop impacts, an extensive parametric analysis could not be performed. However it is also beyond the purpose of the present study, which is oriented to a first phenomenological observation, focused on the difference between the features arising from single and double impacts in the cratering and splashing regimes (see Section 3.1). Ten cases have been selected, whose figures have been reported at the end of the section and whose impact parameters have been summarized in Table 7. Case *a* (Figure 57) has the lower impact parameters and it is the most influenced by capillary effects. Case *b* is the more detailed case presented. Its related images have been taken from two orthogonal lateral sides (Figure 58) as well as from below (Figure 59) and from an inclined view (Figure 60). Cases *c-g* (Figure 61, 62, 63, 64, 65) have the same impact velocity and similar drop diameters. They have been chosen to investigate the influence of the drop distance $\tilde{L}$. Cases *h-l* (Figure 66, 67, 68) are in the splashing regime, while the previous cases are in the cratering post-entrapment regime (if the impact parameters are reported to the classification of single drop impacts onto a deep pool given in Section 3.1).

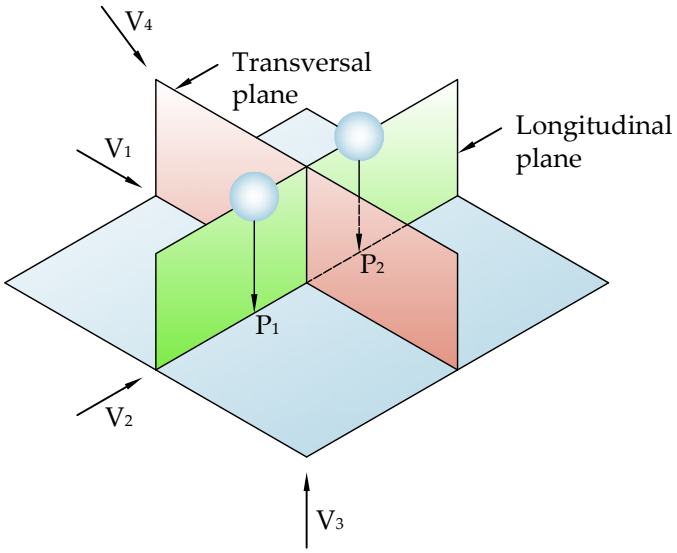

Figure 56: Sketch of the symmetry planes and of the camera views. The double drop impacts have a symmetry with respect to the longitudinal and transversal planes. The camera views V_1, V_2, V_3 and V_4 have been named respectively: first lateral view, second lateral view, view from below, inclined view.

4.1 GENERAL CONSIDERATIONS

Symmetry

A first great difference between a single and a double drop impact is the change of symmetry. While a single drop impact is characterized by an axial-symmetric flow (non considering the complexity of the splashing), a double drop impact is characterized by a planar symmetry respect to two planes, as shown in Figure 56. The first plane of symmetry is the longitudinal plane, i. e. the vertical plane passing through the two impact points P_1 and P_2. The second symmetry plane is the vertical plane orthogonal to the previous and passing through the middle point of the segment connecting the two impact points.

Interactions

A second difference is the implication of an additional number of interactions between:

- the two falling drops;
- the two crowns;
- the two craters;
- the two jets ejected from the craters;
- the secondary droplets originated from the crowns or from the jets.

The aerodynamic interaction between the two falling drops causes them to merge if they are too close or to diverge if they are above a certain distance, particularly for high falling velocity. As can

be noticed from the data of Table 7, increasing the falling velocity, the dimensionless drop distance $\tilde{L}$ increases, being constant the initial distance of the two drops. Consider as an example the image sequence of Figure 67, corresponding to the case *i* of Table 7. When the two drops impact, (b), the prompt splashing of a drop is not influenced by the proximity of the other drop, since the process is present only in the very early stage of the impact. Than the two impacts develop a crown and a crater, which grow in time, (c). First the two crown meet, (d), causing the crown in the region of the contact to be higher than in the other regions, (d)-(g). When the two crowns meet, the phenomenon of splashing is already ceased. In all the recorded cases the impact velocity was not higher enough to evidence an interaction between the two crowns with a still active splashing mechanism. However this is the case analyzed by the few previous studies cited at the begin of the present section, which dealt with multiple drop impacts onto dry surfaces or thin films, where the creation of the crown and the splashing mechanism are more effective than in the case of drop impacts onto a deep pool. In this last case the focus is mainly on the role played by the craters. Few time after the impact each crater start to feel the presence of the other and to modify its shape. The walls on the side between the two impacts becomes more vertical, (d)-(e), while the walls on the other sides deform toward the vertical walls, (f)-(g). Capillary waves are only generated on the external sides, (e)-(f) and travel to the crater bottom, which is in turn moving toward the internal side. The two craters tend to a configuration with the shape of a cone, (g) before to start the receding phase, (g). Two jets are ejected from the bottom of the craters, (h). Their direction is not vertical, as in single drop impacts, but it is inclined toward the internal side, (i). They meet in the middle, (i) and merge to form an original hollow configuration, (j)-(k), which in the end closes in a single jet, (l), from which a very big secondary droplet is detached, (m)-(o). In this example the two jets do not produce secondary droplets before to merge, thus there is not interaction between them. However looking to images (b) and (c) can be imaged the existence of a certain probability of interaction between the great number of secondary droplets generated by the splashing mechanism. A curious example of interaction between the secondary droplets generated by the two jet is presented in Figure 63, corresponding to the case *e* of Table 7. Two almost vertical jets (a little converging toward the internal side) are produced, from which two secondary droplets are detached, (h). The two secondary droplets are projected upward, (i), and afterwards they collide and merge to form a single droplet, (m)-(o). The merging phenomena is very quick and strong. The shape of the resulting droplet deforms and oscillates for a relative long

time before to reach a more stable spherical shape.

Complex shapes

The interactions between the two craters or the two jets ejected by the craters are the most typical features of double drop impact onto a deep pool observed during the present study. These interactions may lead to the formation of new complex shapes, which cannot be observed in single drop impacts. In Figure 66q the two jets merge to form a new jet with a T-shape, which tends to rotate due to the non perfect equality of the two previous jets. In Figure 67k the two jets form a hollow structure, as previously described. An hollow shape can be formed also by the two craters. The craters have a larger section in the region close to the target surface, thus they should meet and start to merge from there. However, since the craters grow deforming toward the transversal plane, their bottoms can meet and start to merge from below, as shown in Figure 62. In (e)-(f) the bottoms of the two craters get so close that in (g) they merge. In the meanwhile the merging of the two craters is begun also on the target surface, leading to the temporary formation of a single hollow crater (h)-(i). In this case the merging process do not prevent the formation of two jets from the original craters, (f), which are agglomerated in the thick jet (more similar to a bump) formed by the final crater, (p)-(q).

4.2 NUMERICAL RELEVANCE

The change of symmetry adds an additional relevance to the study of double drop impacts. As explained in Section 1.2, impacting drops provide an example of an unsteady free surface flow governed by inertial, gravitational, viscous and surface tension effects, for which several numerical approach have been developed. While for a single drop impact the numerical codes have been developed and tested for an axisymmetric geometry, the numerical simulation of a double drop impact requires a three-dimensional geometry. Thus a double drop impact may represent a new opportunity to develop and to test full three-dimensional numerical codes, being in mind that the developed methodologies, thanks to their generality, appear to be transferable to other fields. A full three-dimensional simulation is considerably more expansive from a computational point of view than an axisymmetric simulation, but the simultaneous impact of two identical drops, having two planes of symmetry, has the further advantage to reduce the required computational time, since it is possible to consider only a quarter of the full domain.

Test case

Case *b* of Table 7 has been chosen as test case for a possible numerical simulation and it has been accurately characterized. For identical impact conditions, images have been taken from

the four different points of view V_1, V_2, V_3 and V_4 sketched in Figure 56. The case is in the crater regime, in way to avoid the additional complexity of the splashing mechanism. Figure 58 shows images taken from the first (left column) and second (right column) lateral views. In the first instants after the impact the two impacts do not interact, than the two swells meet on the transversal plane and they merge in a liquid sheet which rise up higher than the other parts of the swells. This can be seen starting from the 3th frames. In the first lateral view (a4) the higher sheet is in the middle and its orthogonal projection is represented in the images of the second lateral view (b4). In (a4)-(a6) the two craters seem to be a little divergent in the region close to the target liquid surface, while their bottom point (the point of the crater having the maximum depth) is soon more close to the transversal plane respect to the related impact point. This means that the two craters try to diverge in the upper region, while they seem attracted in the lower part. In (b7) the higher central sheet on the transversal plane starts to divide in two parts, meaning that the two craters are beginning to merge. More and more fluid is moved from the central part of the higher sheet to the external region, causing a thinning and a lowering of it, as can be seen in the subsequent frames. The merging of the two craters can be observed on the left column. In (a7)-(a9) the two internal walls of the craters get vertical and closer and closer, while the external walls changes from slightly divergent to almost vertical to slightly convergent. Once the merge of the craters start, it evolves fast, led from the surface tension forces due to the high curvature of the transient new shape of the craters, (a10)-(a15). The two craters form therefore a unique crater, whose shape soon loose the memory of the previous two. As can be observed in (a14)-(a18) the final crater has a central region which stagnates and two external regions which rise up quickly. The final crater tends to have a conical shape (a8), whose bottom rises up very slowly forming a bump (a19)-(a36). This bump is similar to those of single drop impacts in the first region of the cratering regime, typical of lower impact parameters. This means that during the merging phase a significative amount of energy is dissipated in the creation of the new surface and the modification of the velocity field around the final crater causes a jet not to be formed. Another interesting feature can be observed comparing images (a19)-(a36) with images (b19)-(b36), which evidence the non axial symmetry of the submerged configuration. While on the left side only a crater is visible, on the right side the main crater seems to divide in two smaller craters.

Figure 59 shows images taken from below. The black spot visible in central region of the first images is due to a hole in the aluminium plate used to reflect and diffuse the light, as shown in

Figure 5, through which the falling drops pass. In the 3th frame it is possible to see the first moment of contact of the two swells, with formation of an higher liquid sheet, which is straight and is located on the transversal plane. It can be noticed also how the liquid around the two impacts is completely at rest. The capillary waves generated by the impacts are squashed around the two craters, which are thus growing with a velocity higher than that of propagation of the capillary waves in this early stage. Only from the 7th or 8th frame, at dimensionless time of about 6 the capillary waves seem to propagate further the craters. At the 7th frame the central region of the higher liquid sheet on the transversal plane starts to thin and to low, while the liquid is moving to its external edges. At the 10th frame the two crater start to merge, following the path given by the progressive intersection of two deformed hemisphere. Later the structure of the waves becomes more and more complicate. The shape of the capillary waves in the external region is similar to an oval, which tends to become a circle.

Figure 60 shows images taken from the inclined view V_4 of Figure 56. These images are not orthogonal projections, thus they give a three-dimensional perspective. Starting from the 7th frame it is possible to note the erosion of the higher liquid sheet on the transversal plane, with subsequent merge of the craters. From the 19th frame it is clear the formation of two new concavities in the central region, across the transversal plane. In the last frames it is possible to observe the almost oval shape of the final crater, with the oval formed by four arcs of a circle. In its center it is also possible to catch a glimpse of the rising bump.

4.3 INFLUENCE OF THE DROP DISTANCE

The cases *c*-*g* of Table 7 have all the same impact velocity V and a similar drop diameter D. They differ only because of the dimensionless drop distance $\tilde{L}$, even if the cases *d* and *e* have also the same $\tilde{L}$. They have been selected to analyze the influence of the crater merging and of $\tilde{L}$ on the phenomena arising from the double impacts.

Crater merging and bump creation

With a small drop distance (at limit $\tilde{L} = 1$) the two craters soon merge in a final crater, from which a slow bump rises up over the target surface, as previously described for the case *b*.

Bubble entrapment

Increasing $\tilde{L}$ the entrapment of an air bubble into the pool by the final crater has been detected and shown in Figure 61 (case *c*). The mechanism of formation of the bubble is not clear from the images. After the merging of the craters, (g)-(i), the final crater takes the shape of a cone, from whose tip a bubble appears, (n). The bubble seems to have been produced in a region not visible

from the first lateral view and than to be unveiled by the rising of the final crater. A careful observation of the images reveals a non perfect symmetry of the final crater soon after the merging process, (i)-(n), but it is not clear if this circumstance is related with the bubble entrapment.

"Unpredictability" of crater merging

The cases *d*-*e* have all similar impact conditions, but the behaviors have some differences. The case *d* is characterized by the formation of a hollow crater, as previously described. In this case two converging thick jets are ejected from the two craters and than they merge in the bump produced by the final crater. No secondary drops are detached from the tip of the two jets, while in the case *e*, which has almost identical impact parameters, two secondary droplets are detached, raise up and collide to form a single droplet, as previously described. In this case the two craters merge without form a hollow shape, i. e. the merging process take place only from the target surface. Moreover the two jets are initially diverging instead of converging, than they becomes almost vertical while emitting the two secondary droplets. This rotative movement gives a centripetal component to the momentum of the detached secondary droplets, allowing them to meet on the transversal plane. The merging phase of the two jets into the bump formed by the final crater is delayed respect to the previous case.

Hollow crater

Secondary droplets collision

The case *f* has a little larger drop distance $\tilde{L}$. In this case the two jets ejected from the two craters have a longer time before to be absorbed by the bump of the final crater, as shown in Figure 64. Two big secondary droplets (with a size comparable with the size of the impacting drops) are detached at the tip of the jets, (q)-(r), and two other small droplets are formed during the receding phase of the remaining part of the jets, (s)-(t). The first two secondary droplets have a smaller vertical velocity than in the previous case *e* and they soon fall on the target surface. The two jets are initially converging as in the case *d*, then they grow almost vertically.

The case *g* has a further greater drop distance $\tilde{L}$. As shown in Figure 65, the the two swells again meet on the transversal plane and form a higher liquid sheet, (d), while the two craters grow for a longer time without feel each other, (c)-(e). Their shape is almost axisymmetric with respect to the axes orthogonal to the target surface and passing through the impact point. In (f) their shape starts to have a more marked planar symmetry with respect to the transversal plane, as can be deduced from the external walls, which tend to be convergent. The action of the capillarity is not axisymmetric as in single drop impact and the different deformation of the internal and external walls lead to the formation of a singularity in the curvature of the crater profiles, (d)-(j).

Singularity in the curvature of the craters

The shape of the craters evolves from almost hemispherical, (d), to piecewise with three almost well defined edges, (h), to rounded with a singularity, (m), to rounded with a global conical convergence, (n). The singularity in the crater curvature causes the ejection of two initially fast jet, which then become thicker and slower. Their direction is initially convergent, (o), then more vertical, (p), then two secondary droplets are detached, (q). Finally a little bump appears, (r), but only when the two jets are already vanished. In this case the merging between the two craters take place only during their later evolution, (o).

The cases *h*, *i*, and *f* have an higher impact velocity. The images of the case *h* are shown in Figure 66. In (e)-(g) can be noted how the falling down of the crowns generates capillary waves only on the external walls of the craters. The capillary waves travel toward the bottoms of the deforming craters, reducing its wave length and increasing their frequency. The internal walls of the two grater get very close, (f)-(g), without the merging takes place. It only happen later, (i), and do not prevent the ejection of two jets from the original craters, (i), which are initially convergent. They merge into the bump of the final crater before to become more vertical and to detach secondary droplets, giving origin to the complex shape previously described. In the case *i* the two ejected jets are more in advance with respect to the crater merging, Figure 67h, and collide forming the hollow structure previously described, (j)-(k). The case *l* has a further higher impact velocity and drop distance. The crater merging take place still more later, at the end of the receding phase of the two original craters, when their bottoms are almost close to the target surface, Figure 68l. The two ejected jets are initially converging, but they are far enough to not interact. The bump of the final crater is very small and do not affect the evolution of the two jets, (p) -(r). The detached secondary droplets are bigger than the impacting drops.

Large secondary droplets

4.4 CONCLUSIONS

The present study has evidenced, in the range of the investigated impact parameters, the non influence on the splashing of a double impact respect to a single impact onto a deep pool. A difference may arise with higher impact conditions, which may lead to a situation similar to the study of Cossali et al. (2003, 2004a,b, 2005, 2007), with a bigger crown and a longer generation of secondary droplets. The influence is instead marked for the crater interaction and the subsequent generation of the jets. The two craters may get very close and then merge in a final crater. Depending on the impact parameters, the merging may take

place at different time respect to the impact instant and it may lead to different behaviors. If it takes place during the early stage of the growing phase of the two original craters, it prevents the formation of the two jets from their bottom and the final crater only produces a slow large bump. Increasing the impact velocity or the drop distance, the merging process takes place later, when the two original craters are already generating their two jets. In this case the direction of the jets is initially not vertical and they can subsequently meet and merge each other, before or while the creation of the bump by the final crater.

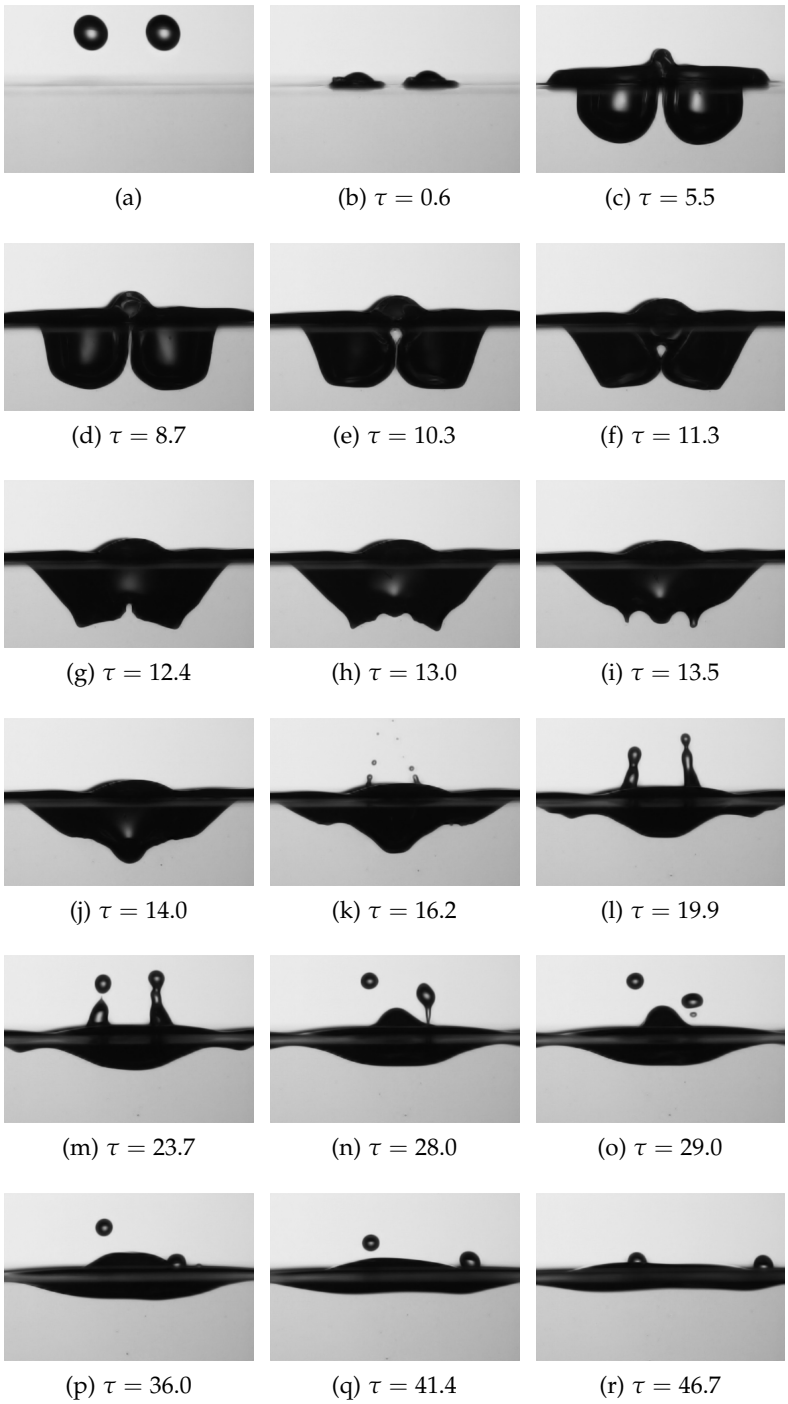

(a) (b) $\tau = 0.6$ (c) $\tau = 5.5$

(d) $\tau = 8.7$ (e) $\tau = 10.3$ (f) $\tau = 11.3$

(g) $\tau = 12.4$ (h) $\tau = 13.0$ (i) $\tau = 13.5$

(j) $\tau = 14.0$ (k) $\tau = 16.2$ (l) $\tau = 19.9$

(m) $\tau = 23.7$ (n) $\tau = 28.0$ (o) $\tau = 29.0$

(p) $\tau = 36.0$ (q) $\tau = 41.4$ (r) $\tau = 46.7$

Figure 57: Example of double drop impact: case *a* of Table 7. It may observed the asymmetric ejection of two fast jets. (Water, $D = 2.8\,\text{mm}$, $V = 1.9\,\text{m/s}$, $We = 134$, $Fr = 127$, $Re = 6486$, $\tilde{L} = 2.0$).

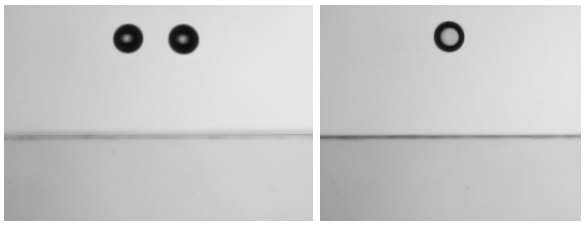

(a1) (b1)

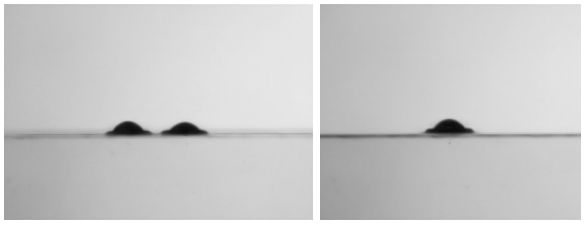

(a2) $\tau = 0.6$ (b2) $\tau = 0.6$

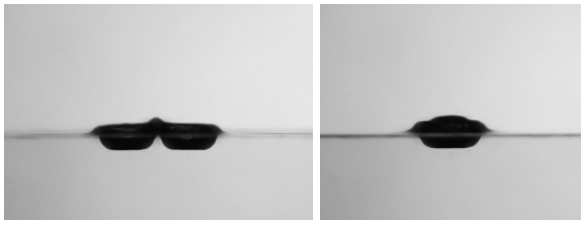

(a3) $\tau = 1.7$ (b3) $\tau = 1.7$

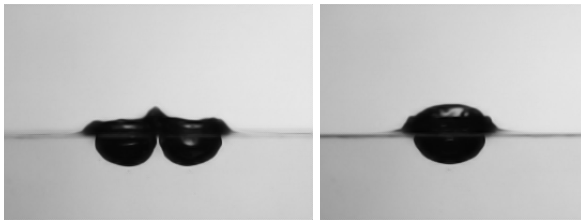

(a4) $\tau = 2.8$ (b4) $\tau = 2.8$

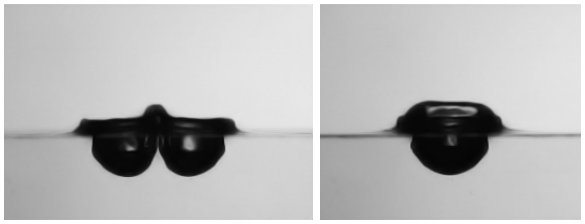

(a5) $\tau = 3.9$ (b5) $\tau = 3.9$

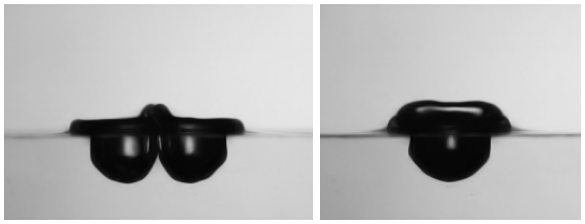

(a6) $\tau = 5.0$ (b6) $\tau = 5.0$

Figure 58: Continue...

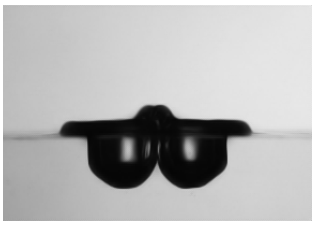

(a7) $\tau = 6.2$

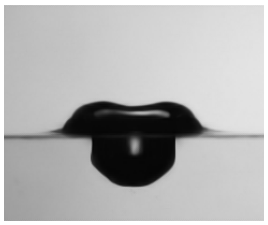

(b7) $\tau = 6.2$

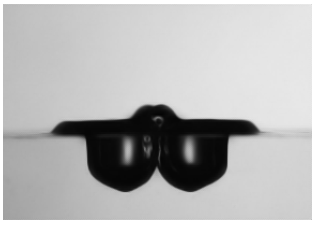

(a8) $\tau = 7.3$

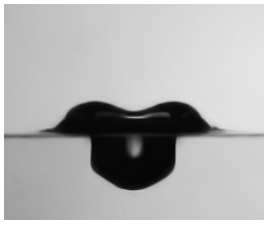

(b8) $\tau = 7.3$

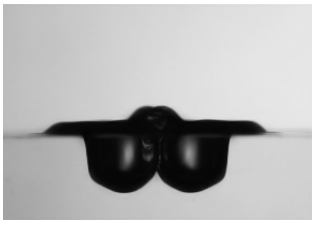

(a9) $\tau = 8.4$

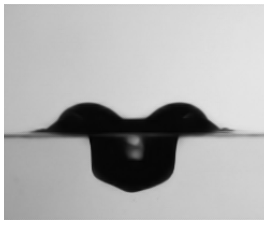

(b9) $\tau = 8.4$

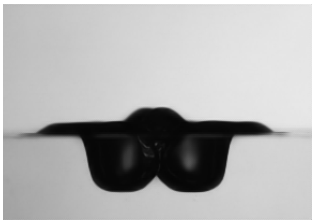

(a10) $\tau = 9.5$

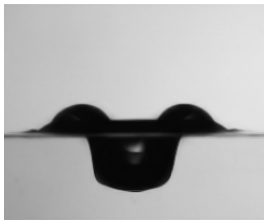

(b10) $\tau = 9.5$

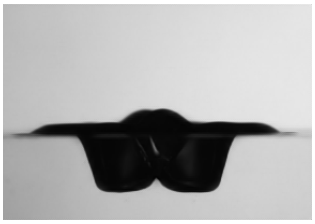

(a11) $\tau = 10.6$

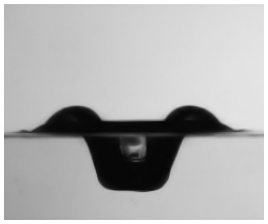

(b11) $\tau = 10.6$

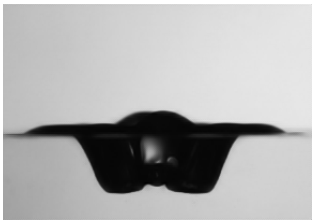

(a12) $\tau = 11.7$

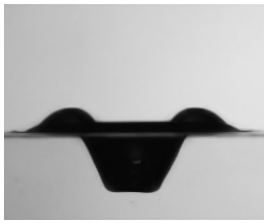

(b12) $\tau = 11.7$

Figure 58: Continue...

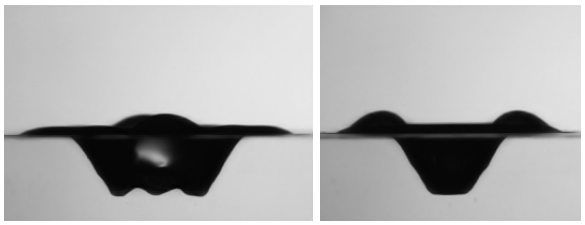

(a13) $\tau = 12.8$ (b13) $\tau = 12.8$

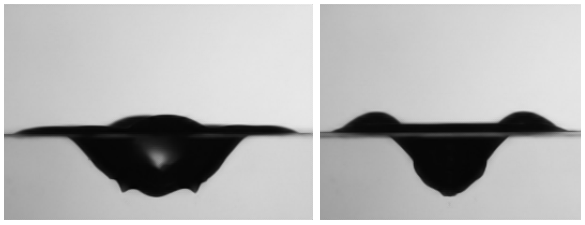

(a14) $\tau = 13.9$ (b14) $\tau = 13.9$

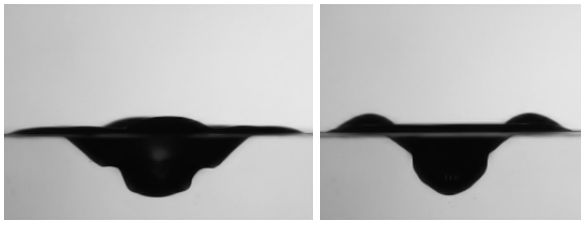

(a15) $\tau = 15.0$ (b15) $\tau = 15.0$

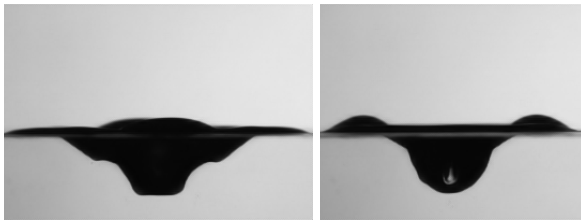

(a16) $\tau = 16.1$ (b16) $\tau = 16.1$

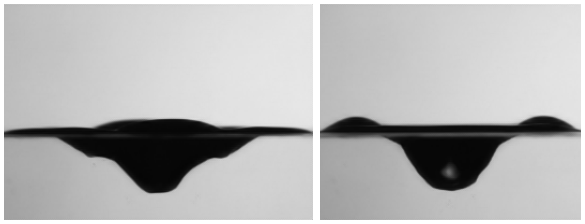

(a17) $\tau = 17.2$ (b17) $\tau = 17.2$

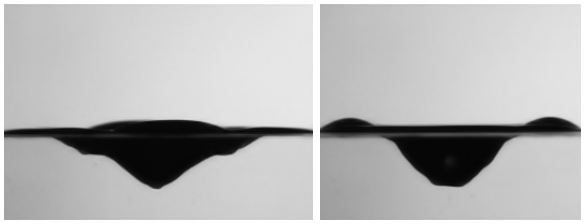

(a18) $\tau = 18.3$ (b18) $\tau = 18.3$

Figure 58: Continue...

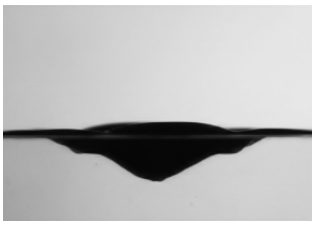

(a19) $\tau = 19.5$

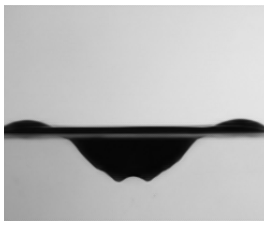

(b19) $\tau = 19.5$

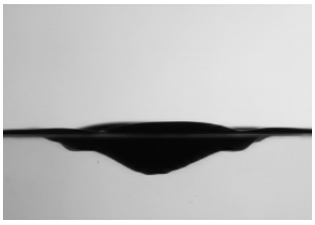

(a20) $\tau = 20.6$

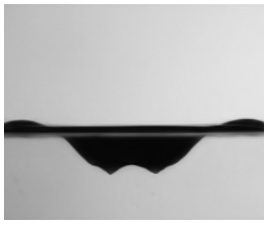

(b20) $\tau = 20.6$

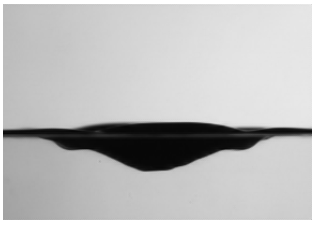

(a21) $\tau = 21.7$

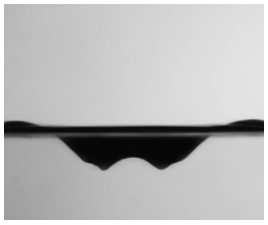

(b21) $\tau = 21.7$

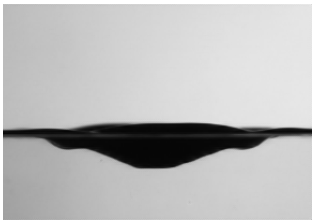

(a22) $\tau = 22.8$

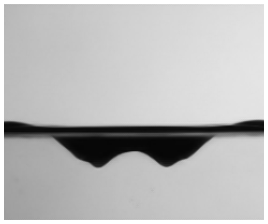

(b22) $\tau = 22.8$

(a23) $\tau = 23.9$

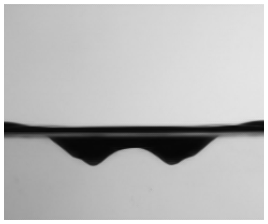

(b23) $\tau = 23.9$

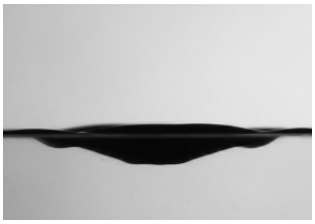

(a24) $\tau = 25.0$

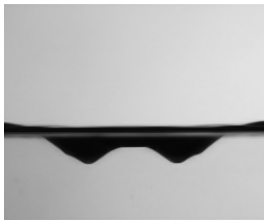

(b24) $\tau = 25.0$

Figure 58: Continue...

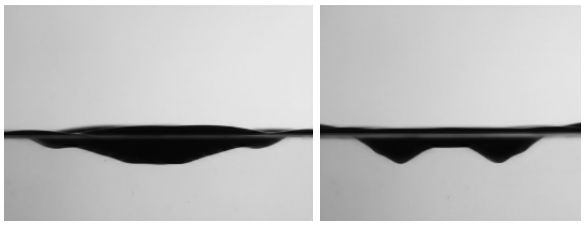

(a25) $\tau = 26.1$ (b25) $\tau = 26.1$

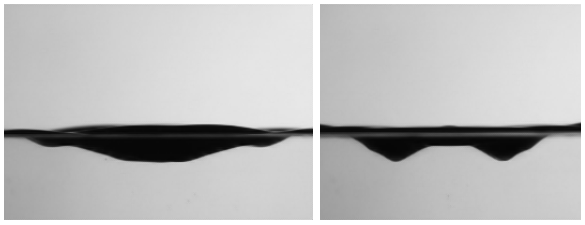

(a26) $\tau = 27.2$ (b26) $\tau = 27.2$

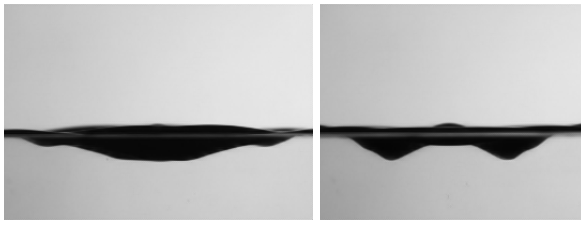

(a27) $\tau = 28.3$ (b27) $\tau = 28.3$

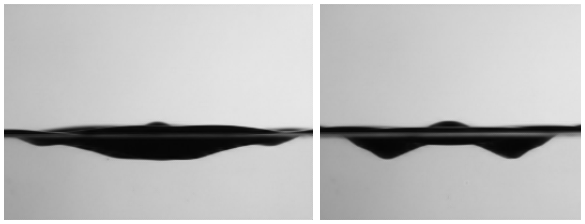

(a28) $\tau = 29.4$ (b28) $\tau = 29.4$

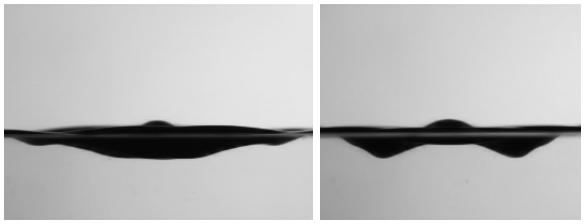

(a29) $\tau = 30.5$ (b29) $\tau = 30.5$

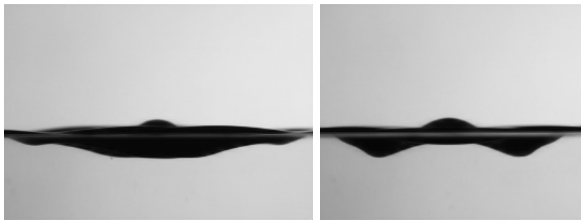

(a30) $\tau = 31.7$ (b30) $\tau = 31.7$

Figure 58: Continue...

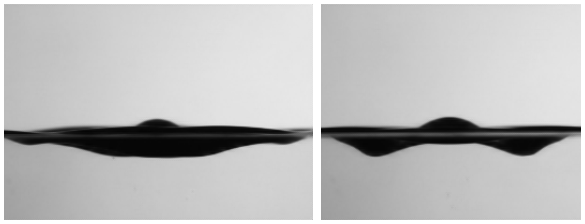

(a31) $\tau = 32.8$ (b31) $\tau = 32.8$

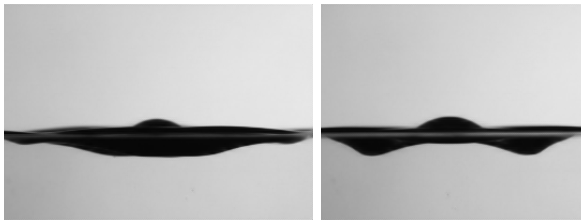

(a32) $\tau = 33.9$ (b32) $\tau = 33.9$

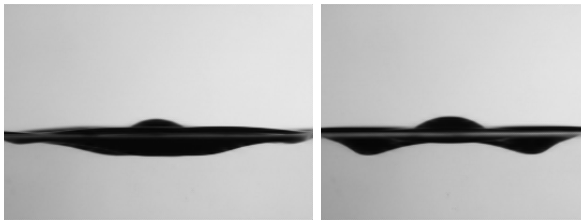

(a33) $\tau = 35.0$ (b33) $\tau = 35.0$

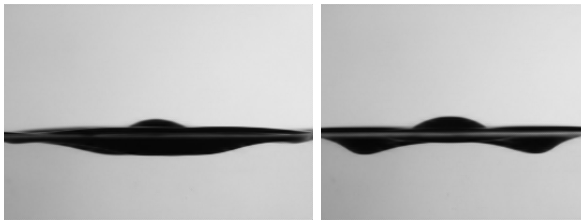

(a34) $\tau = 36.1$ (b34) $\tau = 36.1$

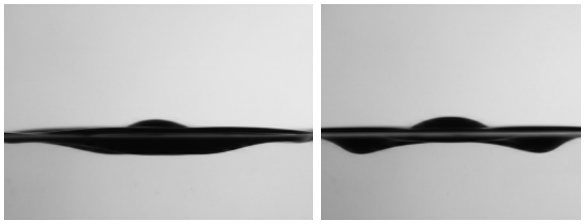

(a35) $\tau = 37.2$ (b35) $\tau = 37.2$

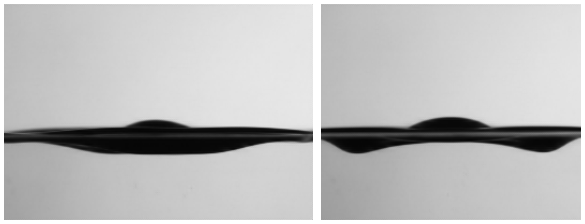

(a36) $\tau = 38.3$ (b36) $\tau = 38.3$

Figure 58: Example of double drop impact: case *b* of Table 7: view from two orthogonal lateral sides. It may be observed the crater evolution and merging. (Water, $D = 2.15\,\mathrm{mm}$, $V = 2.0\,\mathrm{m/s}$, $We = 120$, $Fr = 180$, $Re = 5265$, $\tilde{L} = 1.9$).

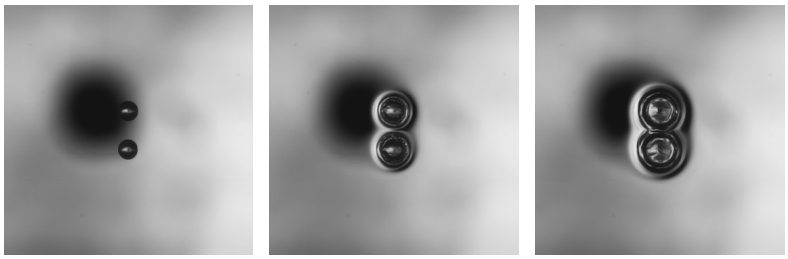

(1) (2) $\tau = 0.4$ (3) $\tau = 1.1$

(4) $\tau = 1.8$ (5) $\tau = 2.5$ (6) $\tau = 3.9$

(7) $\tau = 5.3$ (8) $\tau = 6.7$ (9) $\tau = 8.1$

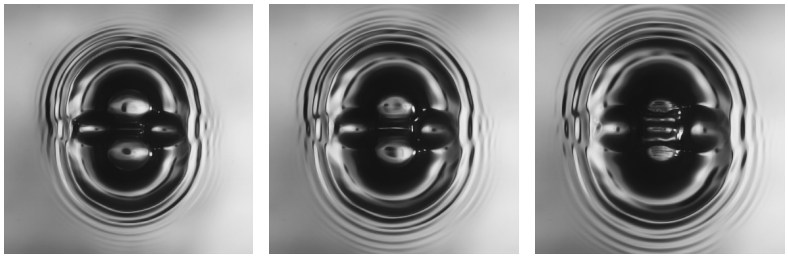

(10) $\tau = 9.5$ (11) $\tau = 11.0$ (12) $\tau = 12.4$

(13) $\tau = 13.8$ (14) $\tau = 15.2$ (15) $\tau = 16.6$

Figure 59: Continue...

(16) $\tau = 18.7$ (17) $\tau = 20.9$ (18) $\tau = 23.0$

(19) $\tau = 25.1$ (20) $\tau = 27.2$ (21) $\tau = 29.3$

(22) $\tau = 31.5$ (23) $\tau = 33.6$ (24) $\tau = 35.7$

(25) $\tau = 37.8$ (26) $\tau = 39.9$ (27) $\tau = 42.1$

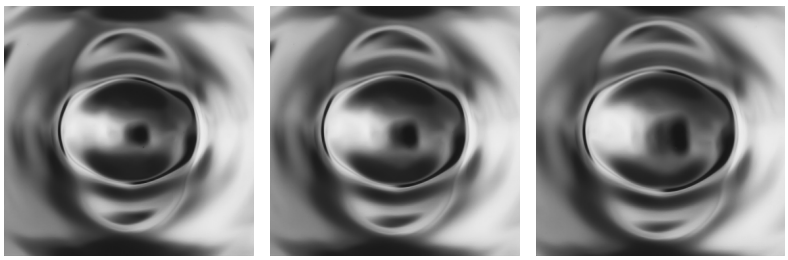

(28) $\tau = 44.2$ (29) $\tau = 45.6$ (30) $\tau = 47.7$

Figure 59: Example of double drop impact: case *b* of Table 7: view from below. It may be observed the evolution of the crater profiles and the pattern of the capillary waves. (Water, $D = 2.15\,\mathrm{mm}$, $V = 2.0\,\mathrm{m/s}$, $We = 120$, $Fr = 180$, $Re = 5265$, $\tilde{L} = 1.9$).

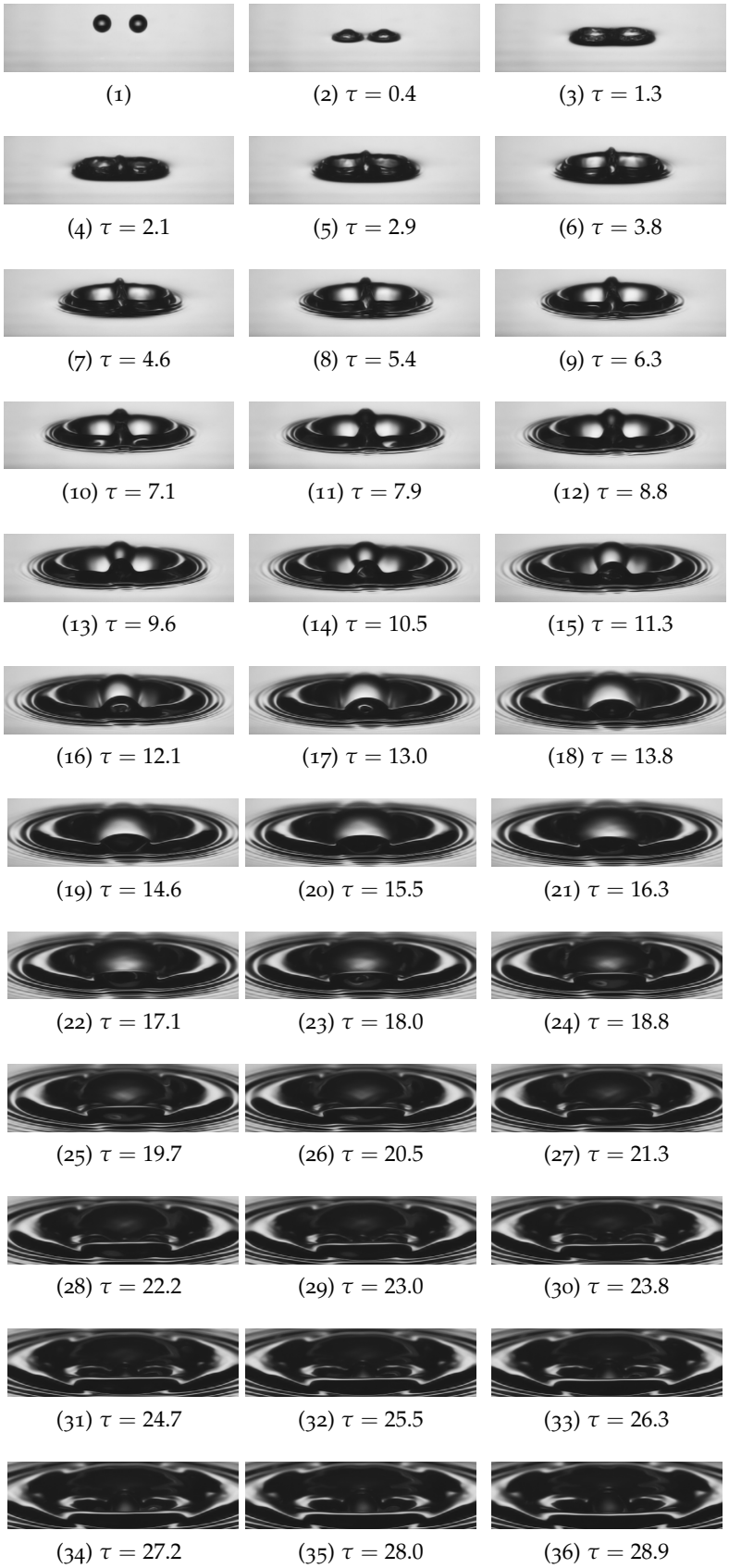

Figure 60: Example of double drop impact: case *b* of Table 7: inclined view. It may be observed the merging of the crater and it shape. (Water, $D = 2.15\,\mathrm{mm}$, $V = 2.0\,\mathrm{m/s}$, $We = 120$, $Fr = 180$, $Re = 5265$, $\tilde{L} = 1.9$).

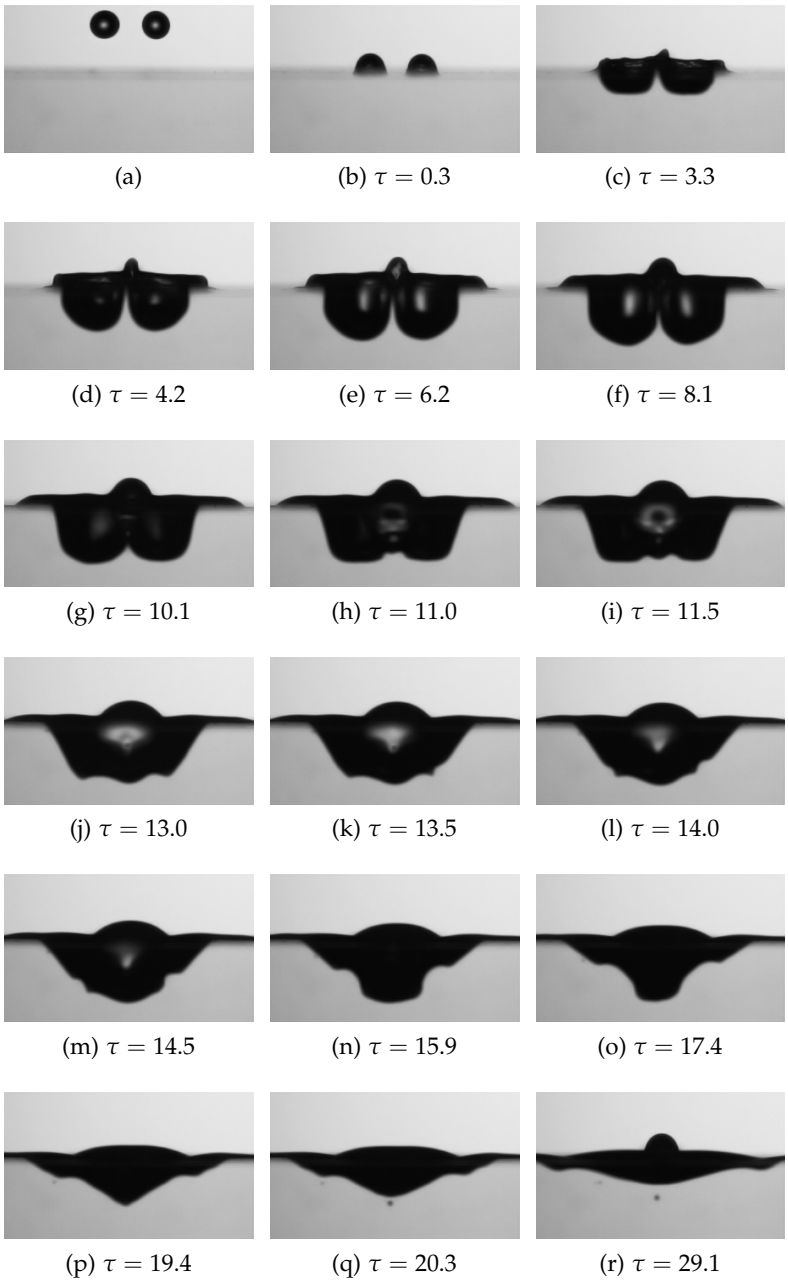

(a) (b) $\tau = 0.3$ (c) $\tau = 3.3$

(d) $\tau = 4.2$ (e) $\tau = 6.2$ (f) $\tau = 8.1$

(g) $\tau = 10.1$ (h) $\tau = 11.0$ (i) $\tau = 11.5$

(j) $\tau = 13.0$ (k) $\tau = 13.5$ (l) $\tau = 14.0$

(m) $\tau = 14.5$ (n) $\tau = 15.9$ (o) $\tau = 17.4$

(p) $\tau = 19.4$ (q) $\tau = 20.3$ (r) $\tau = 29.1$

Figure 61: Example of double drop impact: case *c* of Table 7. It may be observed the entrapment of a air bubble in the pool. (Water, $D = 2.5\,\mathrm{mm}$, $V = 2.1\,\mathrm{m/s}$, $We = 148$, $Fr = 175$, $Re = 6457$, $\tilde{L} = 1.8$).

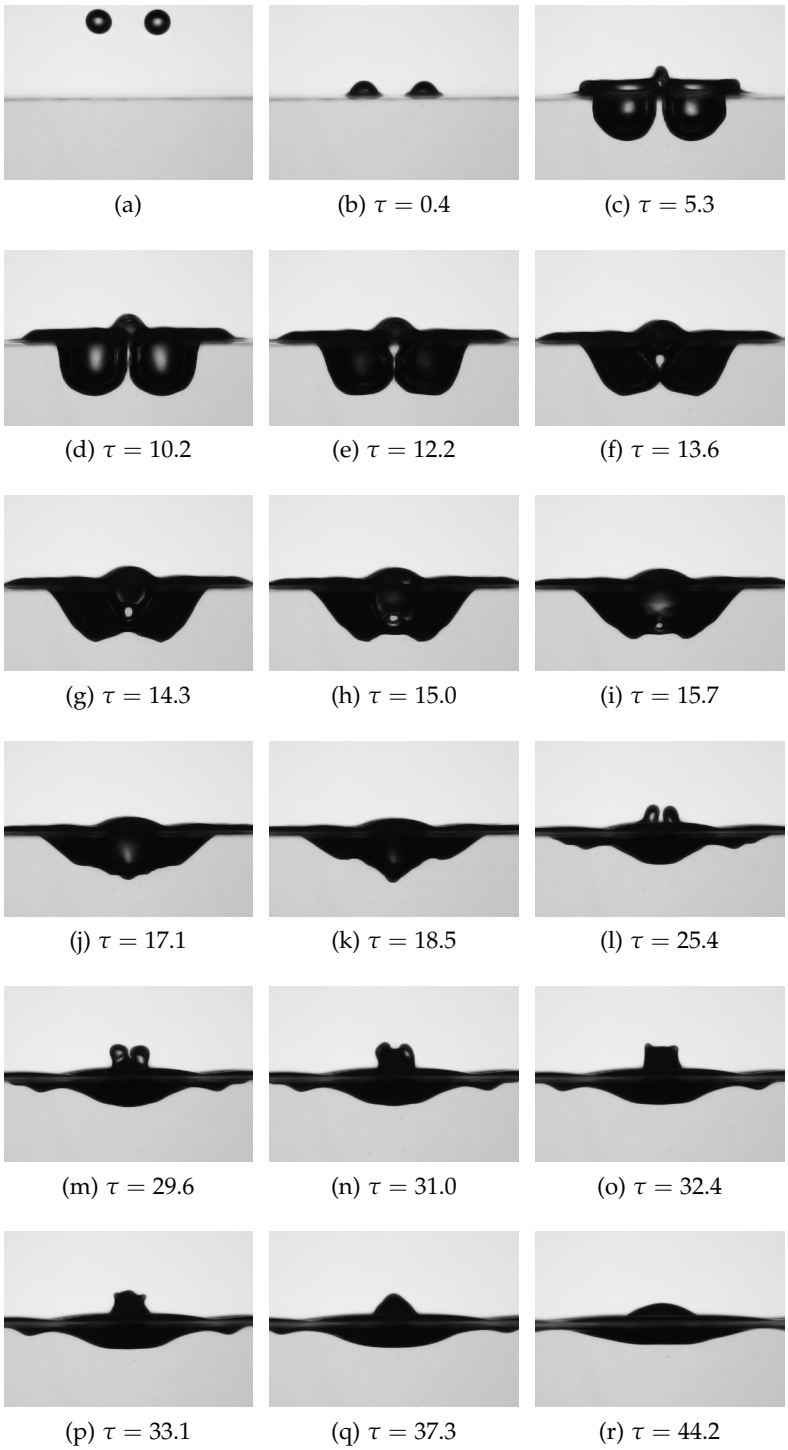

(a) (b) $\tau = 0.4$ (c) $\tau = 5.3$

(d) $\tau = 10.2$ (e) $\tau = 12.2$ (f) $\tau = 13.6$

(g) $\tau = 14.3$ (h) $\tau = 15.0$ (i) $\tau = 15.7$

(j) $\tau = 17.1$ (k) $\tau = 18.5$ (l) $\tau = 25.4$

(m) $\tau = 29.6$ (n) $\tau = 31.0$ (o) $\tau = 32.4$

(p) $\tau = 33.1$ (q) $\tau = 37.3$ (r) $\tau = 44.2$

Figure 62: Example of double drop impact: case *d* of Table 7. It may be observed the hollow shape of the crater. (Water, $D = 2.4\,\mathrm{mm}$, $V = 2.1\,\mathrm{m/s}$, $We = 150$, $Fr = 187$, $Re = 6396$, $\tilde{L} = 2.2$).

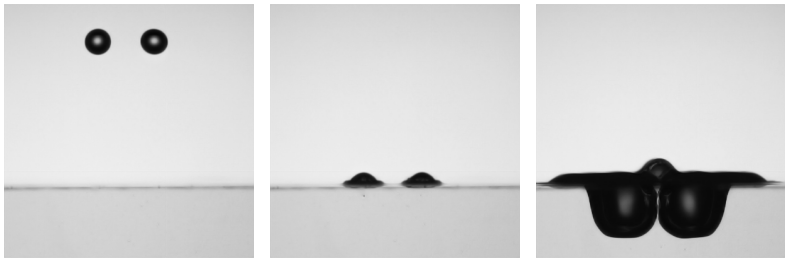

(a)

(b) $\tau = 0.5$

(c) $\tau = 11.0$

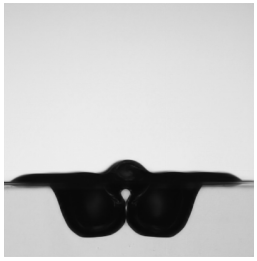

(d) $\tau = 12.3$

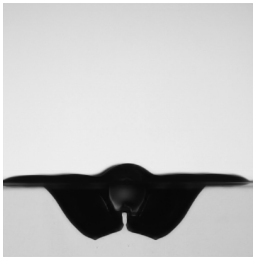

(e) $\tau = 14.4$

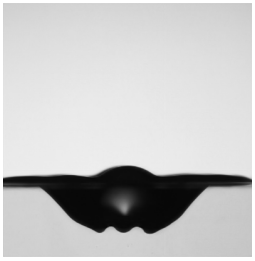

(f) $\tau = 15.8$

(g) $\tau = 20.7$

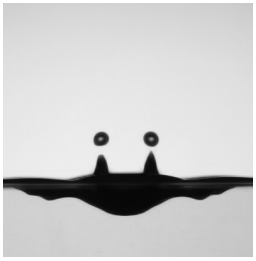

(h) $\tau = 25.5$

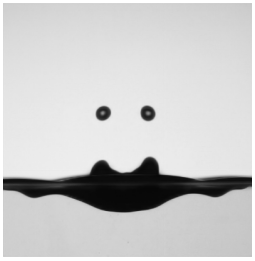

(i) $\tau = 30.4$

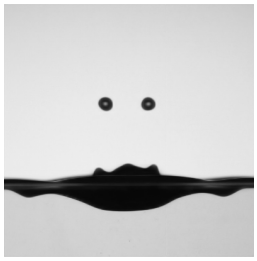

(j) $\tau = 32.5$

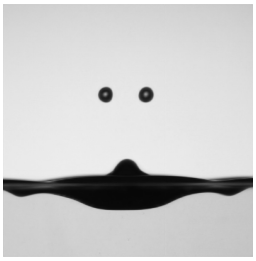

(k) $\tau = 34.6$

(l) $\tau = 58.9$

(m) $\tau = 63.0$

(n) $\tau = 64.4$

(o) $\tau = 65.1$

Figure 63: Example of double drop impact: case *e* of Table 7. It may be observed the interaction of the two secondary droplets. (Water, $D = 2.4\,\mathrm{mm}$, $V = 2.1\,\mathrm{m/s}$, $We = 151$, $Fr = 187$, $Re = 6423$, $\tilde{L} = 2.2$).

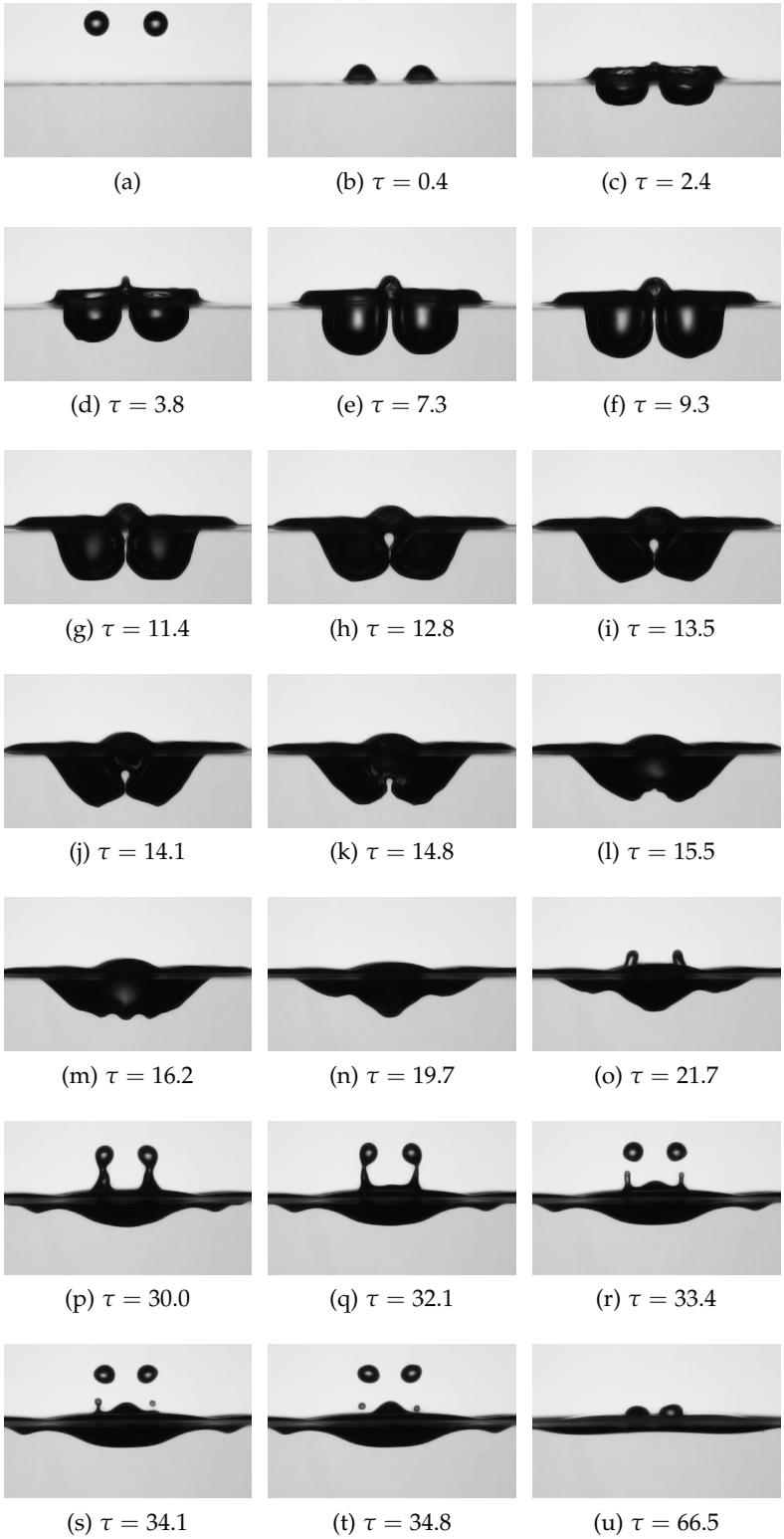

(a) (b) $\tau = 0.4$ (c) $\tau = 2.4$

(d) $\tau = 3.8$ (e) $\tau = 7.3$ (f) $\tau = 9.3$

(g) $\tau = 11.4$ (h) $\tau = 12.8$ (i) $\tau = 13.5$

(j) $\tau = 14.1$ (k) $\tau = 14.8$ (l) $\tau = 15.5$

(m) $\tau = 16.2$ (n) $\tau = 19.7$ (o) $\tau = 21.7$

(p) $\tau = 30.0$ (q) $\tau = 32.1$ (r) $\tau = 33.4$

(s) $\tau = 34.1$ (t) $\tau = 34.8$ (u) $\tau = 66.5$

Figure 64: Example of double drop impact: case *f* of Table 7. It may be observed the rupture of the two ejected jets in four secondary droplets. (Water, $D = 2.4\,\text{mm}$, $V = 2.1\,\text{m/s}$, $We = 146$, $Fr = 186$, $Re = 6480$, $\tilde{L} = 2.3$).

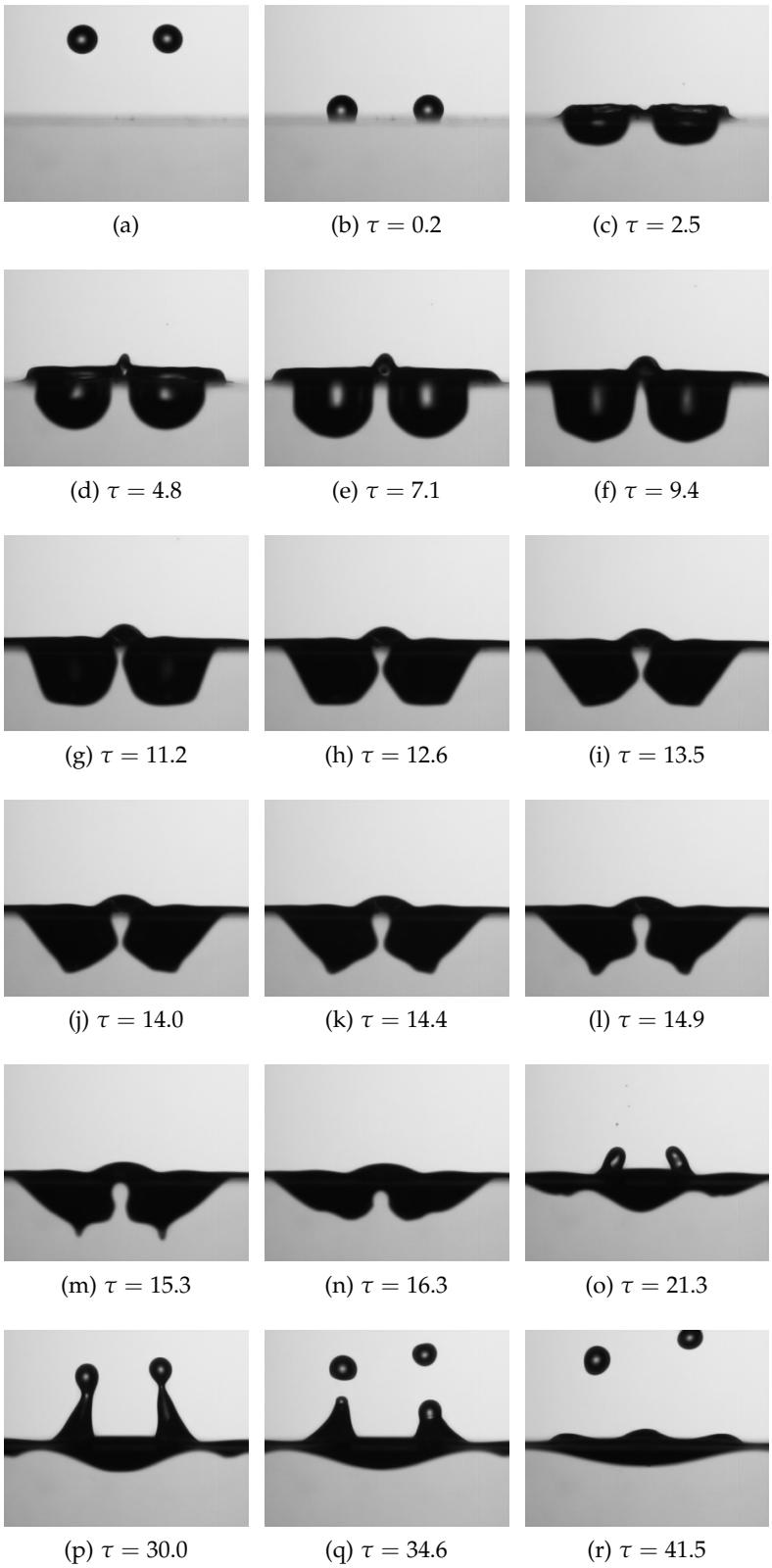

(a) (b) $\tau = 0.2$ (c) $\tau = 2.5$

(d) $\tau = 4.8$ (e) $\tau = 7.1$ (f) $\tau = 9.4$

(g) $\tau = 11.2$ (h) $\tau = 12.6$ (i) $\tau = 13.5$

(j) $\tau = 14.0$ (k) $\tau = 14.4$ (l) $\tau = 14.9$

(m) $\tau = 15.3$ (n) $\tau = 16.3$ (o) $\tau = 21.3$

(p) $\tau = 30.0$ (q) $\tau = 34.6$ (r) $\tau = 41.5$

Figure 65: Example of double drop impact: case *g* of Table 7. It may be observed the high curvature created by the capillary waves and the ejection of two converging jets. (Water, $D = 2.7\,\text{mm}$, $V = 2.1\,\text{m/s}$, $We = 159$, $Fr = 167$, $Re = 6888$, $\tilde{L} = 2.8$).

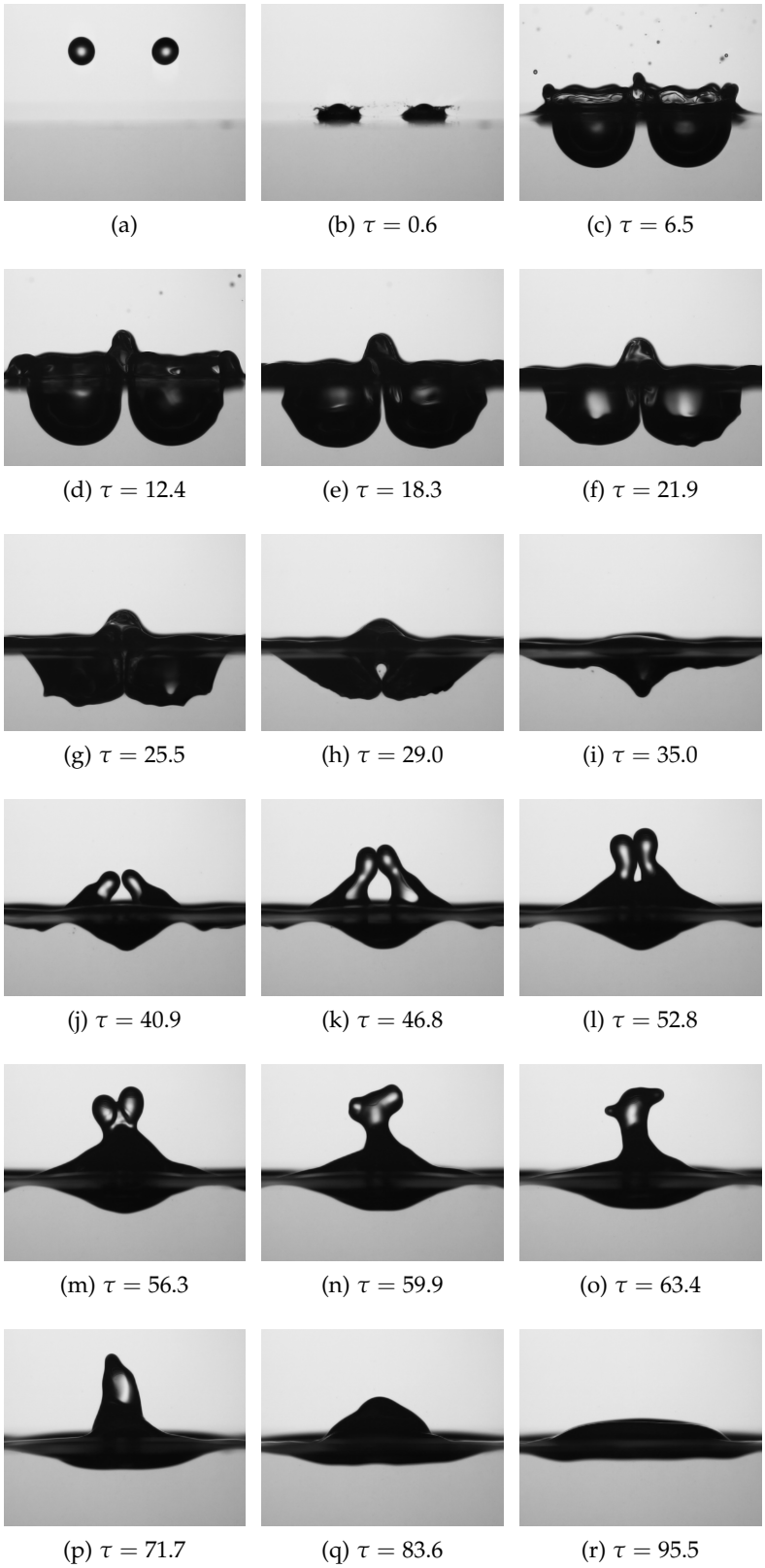

(a) (b) $\tau = 0.6$ (c) $\tau = 6.5$

(d) $\tau = 12.4$ (e) $\tau = 18.3$ (f) $\tau = 21.9$

(g) $\tau = 25.5$ (h) $\tau = 29.0$ (i) $\tau = 35.0$

(j) $\tau = 40.9$ (k) $\tau = 46.8$ (l) $\tau = 52.8$

(m) $\tau = 56.3$ (n) $\tau = 59.9$ (o) $\tau = 63.4$

(p) $\tau = 71.7$ (q) $\tau = 83.6$ (r) $\tau = 95.5$

Figure 66: Example of double drop impact: case *h* of Table 7. It may be observed the complex rotating structure formed by the merging of the two jets. (Water, $D = 2.7\,\mathrm{mm}$, $V = 3.0\,\mathrm{m/s}$, $We = 322$, $Fr = 336$, $Re = 9818$, $\tilde{L} = 3.0$).

(a)

(b) $\tau = 1.8$

(c) $\tau = 4.2$

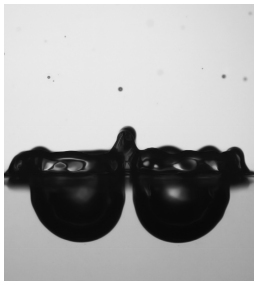

(d) $\tau = 11.4$

(e) $\tau = 20.9$

(f) $\tau = 25.7$

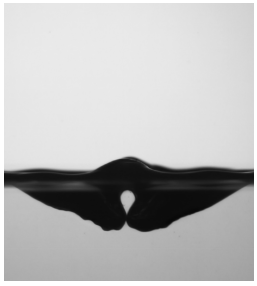

(g) $\tau = 30.5$

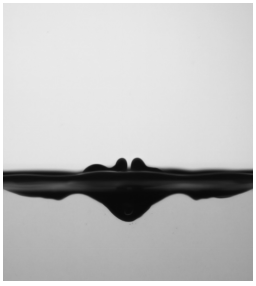

(h) $\tau = 37.7$

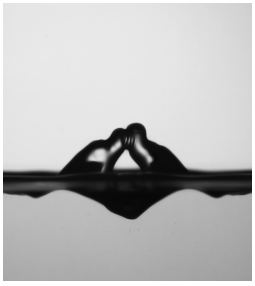

(i) $\tau = 43.7$

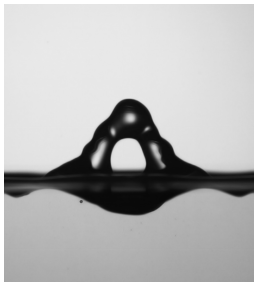

(j) $\tau = 50.8$

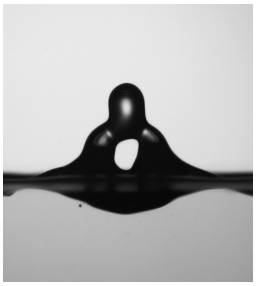

(k) $\tau = 56.8$

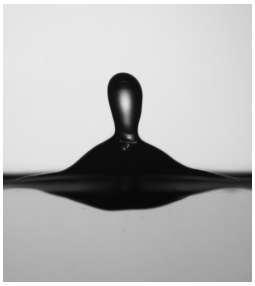

(l) $\tau = 64.0$

(m) $\tau = 78.3$

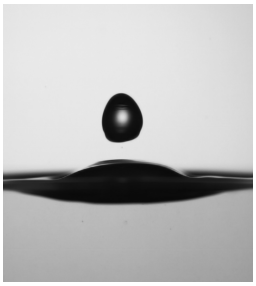

(n) $\tau = 86.7$

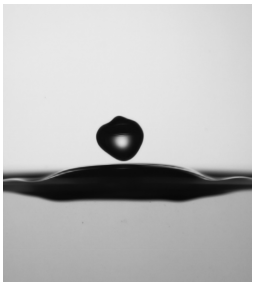

(o) $\tau = 95.1$

Figure 67: Example of double drop impact: case i of Table 7. It may be observed the interactions between crowns, craters, jets and secondary droplets. (Water, $D = 2.6\,\mathrm{mm}$, $V = 3.0\,\mathrm{m/s}$, $We = 320$, $Fr = 337$, $Re = 9763$, $\tilde{L} = 3.1$).

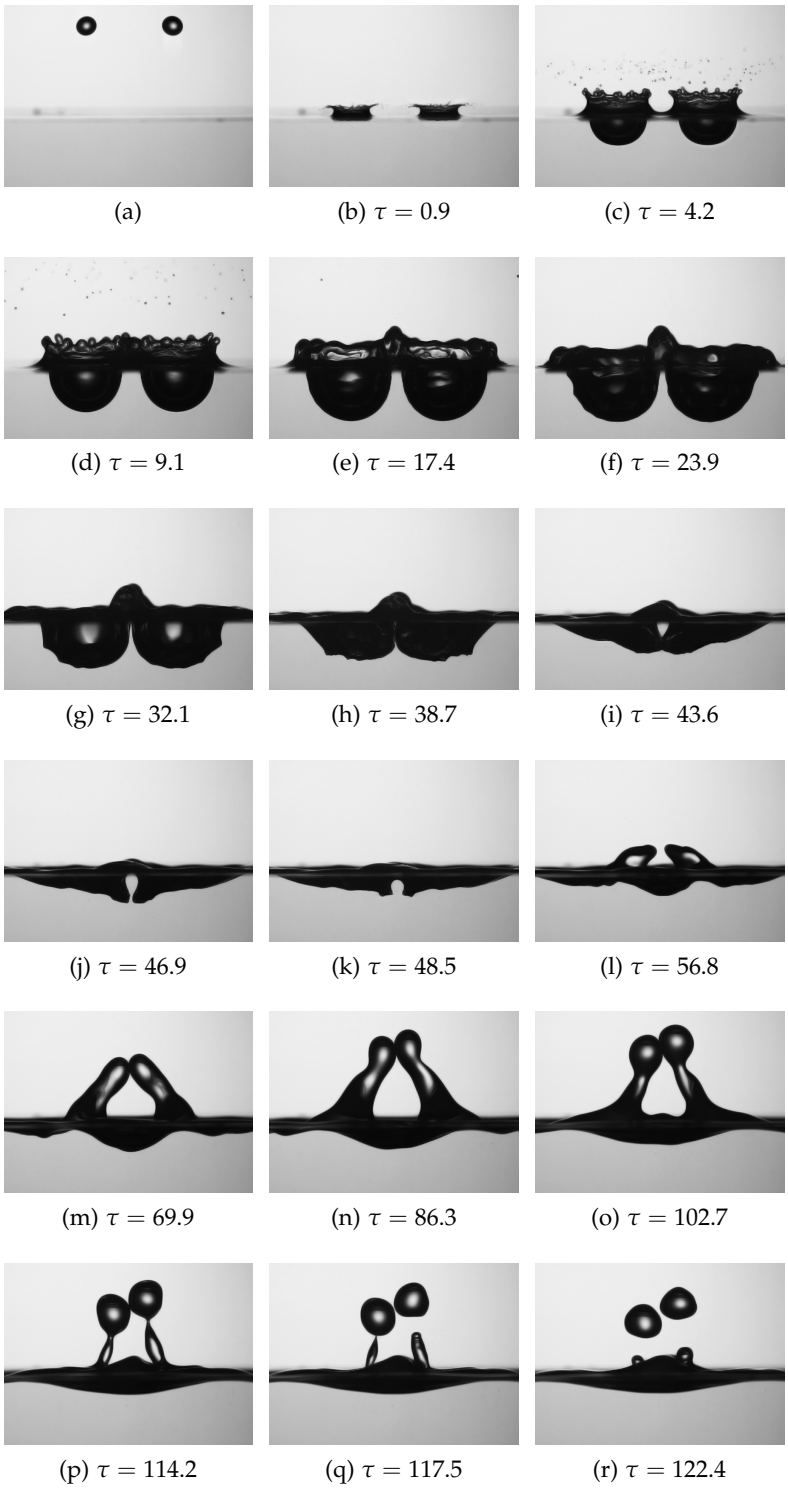

(a) (b) $\tau = 0.9$ (c) $\tau = 4.2$

(d) $\tau = 9.1$ (e) $\tau = 17.4$ (f) $\tau = 23.9$

(g) $\tau = 32.1$ (h) $\tau = 38.7$ (i) $\tau = 43.6$

(j) $\tau = 46.9$ (k) $\tau = 48.5$ (l) $\tau = 56.8$

(m) $\tau = 69.9$ (n) $\tau = 86.3$ (o) $\tau = 102.7$

(p) $\tau = 114.2$ (q) $\tau = 117.5$ (r) $\tau = 122.4$

Figure 68: Example of double drop impact: case *l* of Table 7. It may be observed the ejection of two converging jets which do not interact. (Water, $D = 2.6\,\mathrm{mm}$, $V = 3.6\,\mathrm{m/s}$, $We = 484$, $Fr = 515$, $Re = 11\,970$, $\tilde{L} = 4.3$).

5

SINGLE DROP IMPACTS ONTO THICK FILMS

If the liquid layer where a drop impacts has a finite thickness, the impact phenomena may be influenced by the presence of the bottom wall. Starting from a deep pool situation and decreasing the depth, the influence of the wall becomes more and more pronounced, up to the opposite limit case of drop impact onto a dry wall. Usually in studies of drop impacts the target liquid layers are classified in thin, thick (or shallow) and deep on the base of the ratio between their depth H and the diameter D of the impacting drop, i. e. the dimensionless film thickness $\tilde{H}$ defined in Section 1.3:

Additional parameter

$$\tilde{H} = \frac{H}{D}\,.$$

In the present section the influence of a finite depth of the target liquid film on the evolution of the crater has been accurately investigated. It will be shown how the classification in three regions has a significance from a morphological point of view, but the limits cannot depend only from the depth H of the film and the diameter D of the impacting drop, since the impact velocity V must also be considered.

5.1 REVIEW OF PREVIOUS STUDIES

First studies

Probably the first study on drop impacts onto shallow pools was performed by Hobbs and Osheroff (1967), who noticed that when the depth is decreased the velocity and the maximum height of the jet ejected from the crater and the average number of drops that break away from the jet increase until a point where they fall off sharply. They also noticed these picks being more pronounced in liquids with higher surface tension. However their explanation that the jet is influenced by the reflection of the vortex ring on the wall was criticized by Hall et al. (1968), who stated that there are no mechanism for the reflection of the energy from the vortex ring at the base of the tank. They also explained that as the crown collapses the energy available to contribute to the formation of the jet is less in the fluid of lower surface tension because more secondary droplets have been formed.

Craters

Macklin and Hobbs (1969) took the first subsurface images, showing that it is the result of the interaction of the subsurface

cavity with the solid boundary beneath the liquid to influence the behavior of the jet, modifying considerably the pressure gradients in the liquid during the formation and collapse of the crater. Macklin and Metaxas (1976) estimated the deep splashing, where the bottom of the target liquid container does not affect the splash, occurring when the depth of the crater is 1.5 times greater of the maximum depth of the crater, and the shallow splashing, characterized by an almost cylindrical cavity, occurring when the depth of the crater is 0.5 times smaller of the maximum depth of the crater. In both cases they performed an energy balance for the prediction of the maximum crater depth and of the maximum crown height, while, for conditions falling between these two lines, they pointed out that further geometrical factors need to be introduced into the cavity and crown energy terms.

The tuning of a splash

Shin and McMahon (1990) namedas the "tuning of a splash" the fact that the height and the speed of the jet ejected from the crater are greatest when the depth of the target liquid is equal to the maximum crater depth. They found the depth of the crater not changing with the depth of the liquid until it comes very close to the tuning depth, when the crater briefly touches the bottom. Not substantially changes were found varying surface tension or viscosity, while the tuning was almost completely inhibited when a thin piece of synthetic sponge was adhered to the bottom of the pool. This observation allowed them to conclude that when the crater matches the depth of the liquid, the stem which forms at its bottom is delayed in retracting upward by the condition that no fluid velocity is allowed in the vertical direction. Since the curvature of the bottom of the crater is greater in any condition where a lingering stem is still present, surface tension forces are responsible for a higher pressure difference across the air-liquid interface during the jet formation than they would be in the case a deep pool impact. When a sponge layer replaces the solid floor, the tuning phenomenon is all but extinguished because small but important upward liquid motions at the surface of the sponge are permitted by the network of liquid-filled holes.

Splashing

Manzello and Yang (2002) found the critical impact Weber number for jet breakup being independent of liquid depth. Wal et al. (2006) observed thin films promoting splashing respect to the impact onto a dry surface, while thicker films act to inhibit it respect to thin films. They explained as a film represents the limiting case of a stationary leading fluid front into which the fluid from the impinging drop is advancing, generating the kinematic gradient which increase the splash. While the small depth of thin layers ensures that all the fluid goes outward, thicker layers absorb the drop rather than directing all the impinging fluid into

a radially directed flow.

Viscosity and surface tension

Wal et al. (2006) investigated also the effect of viscosity and surface tension using several fluids. For impact upon a dry surface, viscosity promotes splashing by fostering a kinematic gradient in the advancing fluid front. For droplets impinging upon a thin fluid film, the effect of viscosity is reversed, since the thin film itself is more effective to interfere with the advancing fluid front, and viscosity would dump the generation of this kinematic gradient. Surface tension manifests itself in the number and size of splashed products and seems to be less important than viscosity to controls the onset of the splash.

Conical shape

Fedorchenko and Wang (2004) signaled how the crater assumes a conical shape shortly before the central jet ejection, which speed is influenced by the value of the angle of the cone, that in turn depends from a competition between inertia, viscosity and surface tension.

Theoretical studies

Roisman et al. (2008) described theoretically the evolution of the crater diameter during the later stage of the crater propagation, improving the kinematic discontinuity approach (Yarin and Weiss, 1995, Roisman and Tropea, 2002), in order to take into account the gravitational and capillary effects. Berberovic et al. (2009), in a combined theoretical, experimental and numerical investigation, proposed a scaling relation for the residual film thickness on the bottom before the receding of the crater.

5.2 INFLUENCE OF THE WALL ON THE CRATER EVOLUTION

Experiments have been performed using water, whose physical properties have already been given in Table 1. The depth of the target film has been varied with the vertical movable platform described in Section 2.2.2. Only impacts in the cratering and splashing regions (Section 3.1.3) have been considered. Obviously if the impact velocity is very small, at limit null, as in the coalescence regime, the impact evolution resents of the presence of the bottom wall only if the film thickness is very small. This relation between the kinetic energy of the impacting drop and the influence of the wall will be better discussed at the end of this section.

Thin films

For target films of very small depth the crater instantly or soon reaches the bottom and assumes a cylindrical shape, Figure 69. The crater depth is obviously equal to the film depth for the greater part of the impact. The crater width increases in the first stage after the impact, (b)-(e), then it stagnates, (f)-(h), then it reduces thanks to the flow coming from the falling crown, in contrast with what is observed for deep impacts, where it usually in-

creases monotonically. Finally the formation of a small hint of jet is slightly visible in (l).

Hydrophobic surfaces

When the crater reaches the bottom wall, only a very thin film remains on the wall. At this point the characteristic of the surface of the wall as its roughness or its wettability may influence the flow in the thin film and the evolution of the crater. During a test of drop impacts onto a thin film on a super-hydrophobic surface it has been observed the existence of a minimum value of the thickness of the film under which the liquid film does not close again after a crater has been created by a drop impact, leaving a liquid film which only partially covers the super-hydrophobic surface. This takes place when the horizontal projection of the surface tension on the contact line delimiting the hole is strong enough to support the hydrostatic pressure of the liquid film. As shown in Figure 70, in the later stage of the impact, the fluid coming from the crown reduces the previously formed crater, (e), however the contact line does not continue to move in direction of a closure of the film, but moves in a positive radial direction, until a balance of stresses is reached, (f).

Thick films

Increasing a little the film depth, Figure 71, the crater still reaches the bottom and flattens on it (c)-(f). The falling down of the crown generates capillary waves which deform the crater (g)-(j), whose shape tends to a cone (m). From the crater center a jet is ejected (n) with enough strength to detach a secondary droplet at its top (o). This is a first difference respect to impacts onto very thin liquid films, where the crater cannot develop a central jet.

Increasing again the depth of the film, Figure 72, the capillary waves are generated before the crater reaches the bottom wall (d). The crater tends to assume a square shape (g)-(h), then only a portion of it sticks on the bottom, while its lateral wall starts to contract before the upward receding motion is begun (i)-(j). The crater assumes the shape of a funnel, (k), with a concave lateral wall. In the end the crater still reaches a conical shape, (m), from which a high-speed jet is ejected.

The tuning of a splash

When the depth of the film is similar to the maximum depth of the crater, Figure 73, the crater grows as in a deep pool impact, (c)-(i), and only at the end of its growing phase it skims over the bottom before to start to recede. The presence of the wall retards the upward motion of the last part of the crater, causing an enhancement of the surface curvature and of a process of radial focusing. The crater still evolves through a funnel and then a conical shape, (l)-(m), but the velocity of ejection of the jet is the highest and this case is named the "tuning of a splash" (Shin and McMahon, 1990). The jet is thin (as in the microjetting regime described in Section 3.1.2) and from its top many little

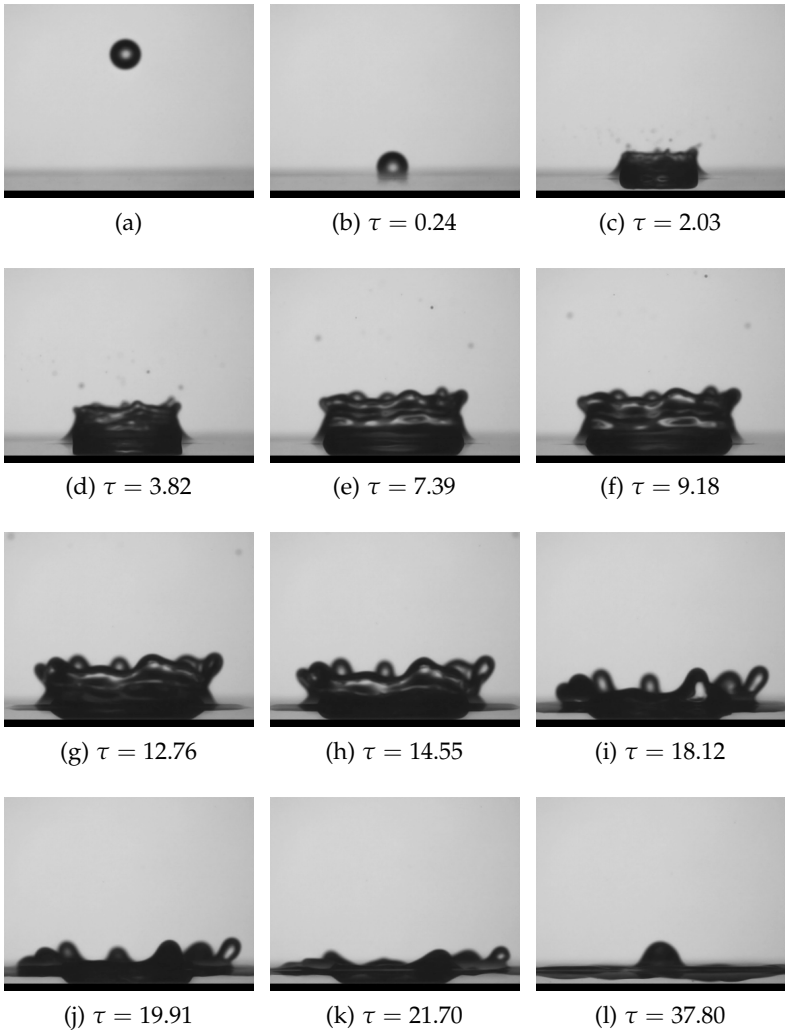

(a) (b) $\tau = 0.24$ (c) $\tau = 2.03$

(d) $\tau = 3.82$ (e) $\tau = 7.39$ (f) $\tau = 9.18$

(g) $\tau = 12.76$ (h) $\tau = 14.55$ (i) $\tau = 18.12$

(j) $\tau = 19.91$ (k) $\tau = 21.70$ (l) $\tau = 37.80$

Figure 69: Drop impact onto a thin film. (Water, $D = 2.5\,\mathrm{mm}$, $V = 2.8\,\mathrm{m/s}$, $We = 260$, $Fr = 314$, $Re = 8488$, $\tilde{H} = 0.5$).

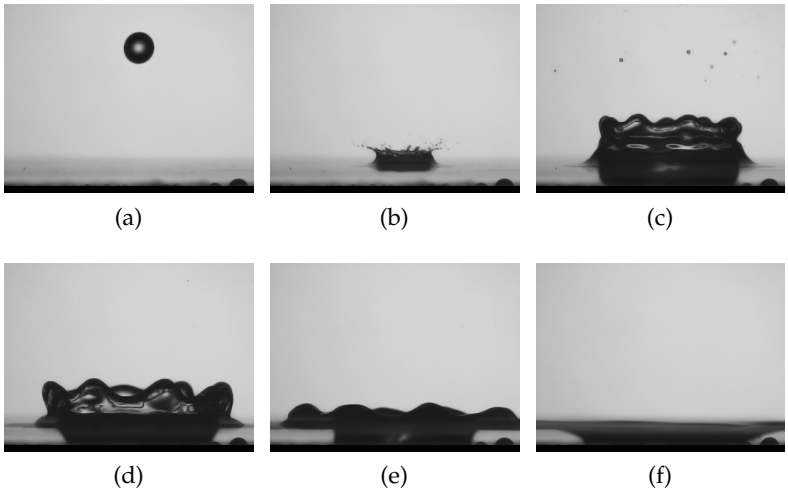

(a) (b) (c)

(d) (e) (f)

Figure 70: Drop impact onto a thin film above a super-hydrophobic surface.

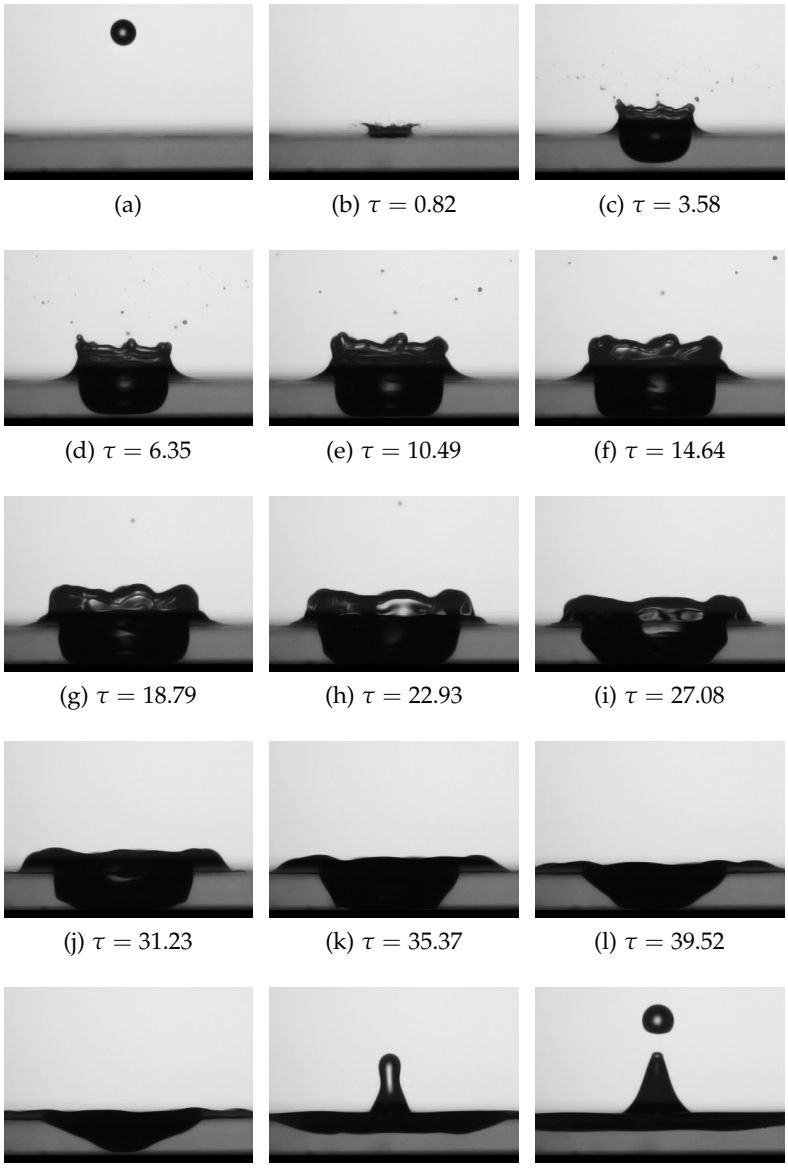

(a) (b) $\tau = 0.82$ (c) $\tau = 3.58$

(d) $\tau = 6.35$ (e) $\tau = 10.49$ (f) $\tau = 14.64$

(g) $\tau = 18.79$ (h) $\tau = 22.93$ (i) $\tau = 27.08$

(j) $\tau = 31.23$ (k) $\tau = 35.37$ (l) $\tau = 39.52$

(m) $\tau = 43.67$ (n) $\tau = 61.64$ (o) $\tau = 90.67$

Figure 71: Drop impact onto a thin/thick film. (Water, $D = 2.2\,\mathrm{mm}$, $V = 2.8\,\mathrm{m/s}$, $We = 237$, $Fr = 359$, $Re = 7668$, $\tilde{H} = 1.4$).

(a) (b) $\tau = 0.62$ (c) $\tau = 2.61$

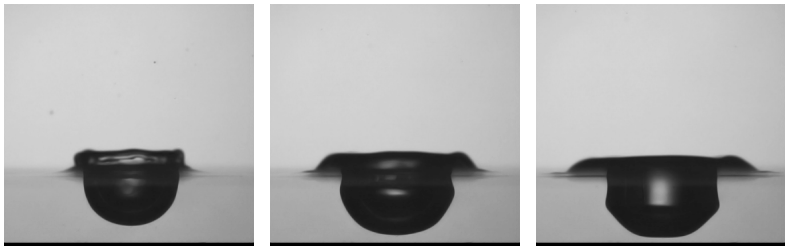

(d) $\tau = 6.60$ (e) $\tau = 12.58$ (f) $\tau = 16.57$

(g) $\tau = 18.56$ (h) $\tau = 21.55$ (i) $\tau = 23.55$

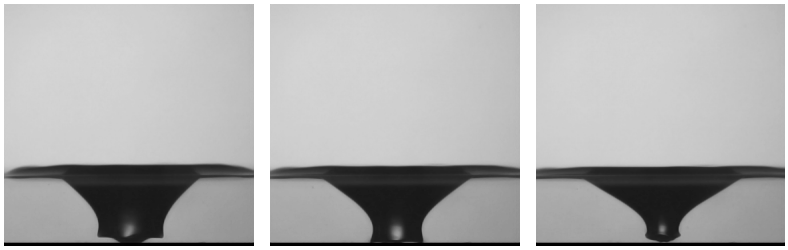

(j) $\tau = 25.54$ (k) $\tau = 27.54$ (l) $\tau = 29.53$

(m) $\tau = 31.52$ (n) $\tau = 36.51$ (o) $\tau = 43.49$

Figure 72: Drop impact onto a thick film with formation of a funnel-shaped crater. (Water, $D = 2.4\,\mathrm{mm}$, $V = 2.7\,\mathrm{m/s}$, $We = 231$, $Fr = 349$, $Re = 7570$, $\tilde{H} = 2.4$).

secondary droplets are detached.

Measurements

In order to better quantify the influence of a finite thickness of the target liquid film on the crater evolution, measurements have been performed on a set of acquisitions concerning the impact of a drop onto a liquid film of several depths. The impact parameters have been kept constant and are resumed in Table 8. Six cases related to six different depths have been selected and reported in Table 9.

Fluid	D (mm)	V (m/s)	We	Fr	Bo	Re
water	2.9	3.6	518	467	0.75	12 917

Table 8: Impact parameters kept constant while varying the pool depth.

Case	$\tilde{H}$	Δ_{max}
a	1.1	1.1
b	1.4	1.4
c	2.2	2.2
d	2.6	2.5
e	3.0	2.6
f	Inf	2.6

Table 9: Dimensionless film depths and maximum crater depths for six selected cases.

Crater evolution

Starting from a deep pool case and reducing progressively the pool depth has revealed the maximum depth of the crater not changing until the pool depth is very close to the maximum crater depth of the deep pool case, as confirmed by Figure 74a, which reports the evolution in time of the dimensionless crater depth Δ for the six selected cases previously introduced. However it can be noticed how cases d, e, f have almost the same maximum crater depth, but the evolution in time of the crater is different. The presence of the wall has the effect to slow down the crater penetration, causing the craters in the thick films cases to reach their maximum at a later time. The receding phase is delayed in time and its initial velocity becomes faster and faster, having a maximum when the maximum depth of the crater is equal to the film thickness. The total time evolution of the crater is almost similar for all the cases, as well as the velocity of penetration in the very early stage after the impact.

Figure 74b shows the evolution in time of the dimensionless

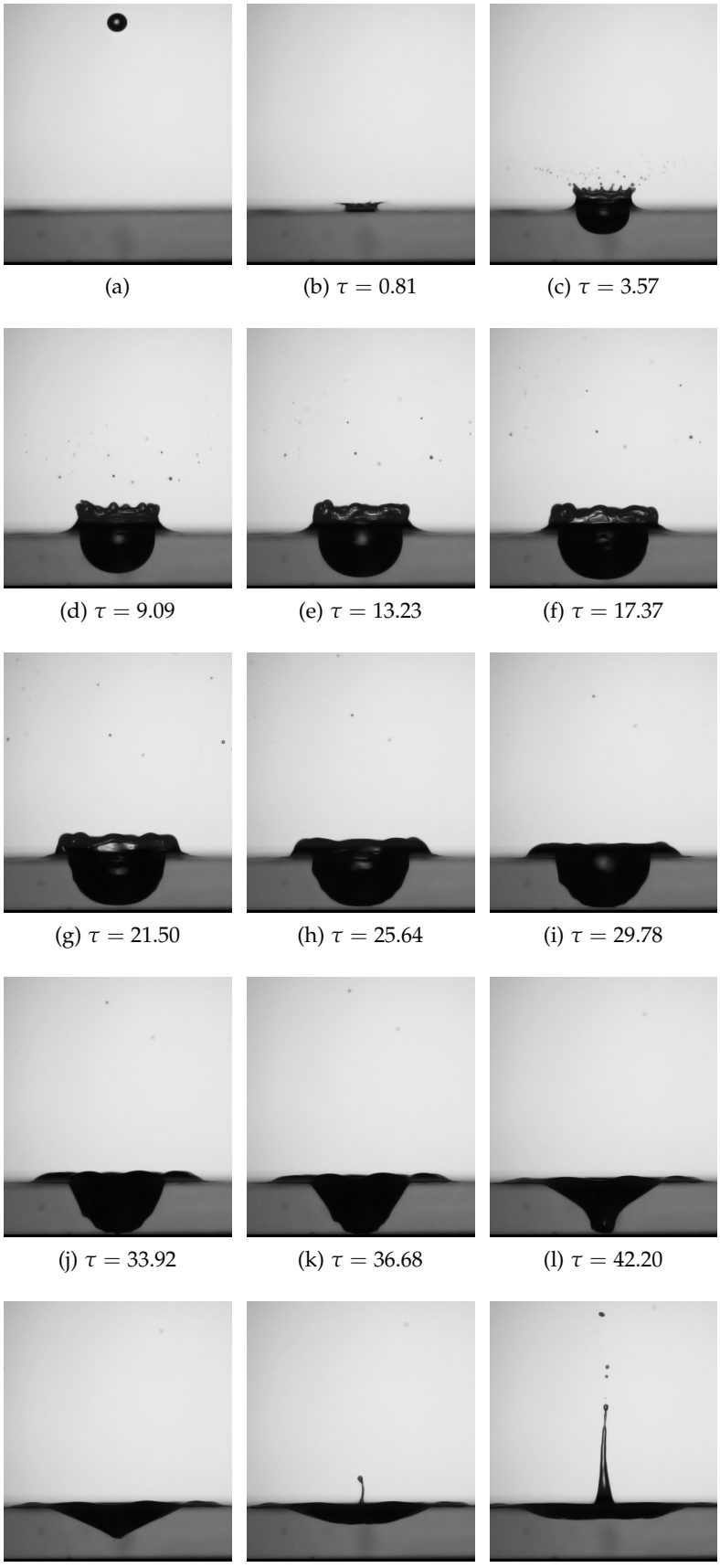

(a) (b) $\tau = 0.81$ (c) $\tau = 3.57$

(d) $\tau = 9.09$ (e) $\tau = 13.23$ (f) $\tau = 17.37$

(g) $\tau = 21.50$ (h) $\tau = 25.64$ (i) $\tau = 29.78$

(j) $\tau = 33.92$ (k) $\tau = 36.68$ (l) $\tau = 42.20$

(m) $\tau = 44.95$ (n) $\tau = 47.71$ (o) $\tau = 55.99$

Figure 73: Drop impact onto a thick film with the tuning of a splash. (Water, $D = 2.2\,\mathrm{mm}$, $V = 2.8\,\mathrm{m/s}$, $We = 236$, $Fr = 358$, $Re = 7650$, $\tilde{H} = 2.7$).

crater width Ω. The presence of the wall seems to influence the crater width only for film thickness about equal to the drop diameter ($\tilde{H} \sim 1$, while the evolution for greater depths is close to a deep impact case.

Figure 74c evidences the increase of the shape ratio $\epsilon = \Delta/\Omega$ with the pool depth. For small pool depths the shape ratio ϵ is little and the crater has an almost cylindrical shape, with a flat bottom. For a greater pool depth the shape ratio ϵ is bigger and it has a maximum in the case of a deep impact.

Graphical comparison

To better understand the evolution of the crater in an intermediate situation, where the crater does not touch the wall, therefore in a region between a deep pool impact and an impact with the tuning of a splash, a graphical comparison is reported in Figure 75. The first column reports an impact onto a deep pool, case f of Table 9. The second column reports the case e, with a dimensionless film thickness $\tilde{H} = 3$. The third column shows a superposition of the first two cases, where edges have been highlighted. The superposition has been possible since the falling drops of the two cases have the same velocity and diameter and the images of the impacts have been recorded at the same time instants, relative to the time of impact. As can be seen from the images of the third column, the growth of the crater is very similar in the early stage and only at 3th frame a difference is slightly visible. Then, in the 4th frame, the crater in the deep pool situation (in black) reaches its maximum depth and stagnates before stars to recede, while the crater of the thick film impact (in red) is in late, but it is still growing. In the 5th frame the depth of the two craters is similar and the image represents the intersection between the two lines of cases e and f of Figure 74a. It can be noticed how all the craters and the crowns are absolutely similar. Then, in the 6th frame, while the black crater is already receding, the red crater reaches its maximum and stagnates. The receding of the red crater is further delayed, as can be see in the 7th frame. While the width of the two craters keeps remain the same, the upward motion of the bottom of the red crater is slowed down by a limitation of the flow coming from the bottom, where there is the wall, and the crater assumes the shape of a cone. At this point, in the 8th frame, the receding and the ejection of a jet from the red crater is so faster than the black crater that the jet of the first reaches and overpass the jet of the second, as shown in the 9th and 10th frame. Therefore it seems that the ejection of faster jets in situation closer to the tuning regime is not due (or not only) to a higher curvature of the surface of the crater, as reported by Shin and McMahon (1990), but to a mechanism of radial focusing, in concomitance with a smaller amount of liquid forming the jet.

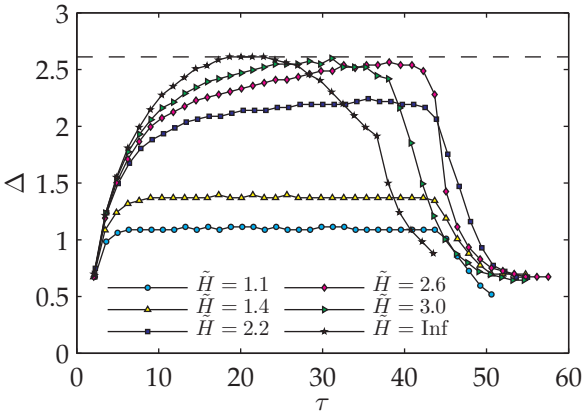

(a)

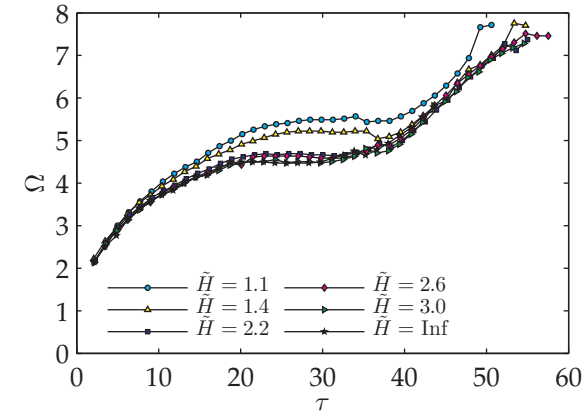

(b)

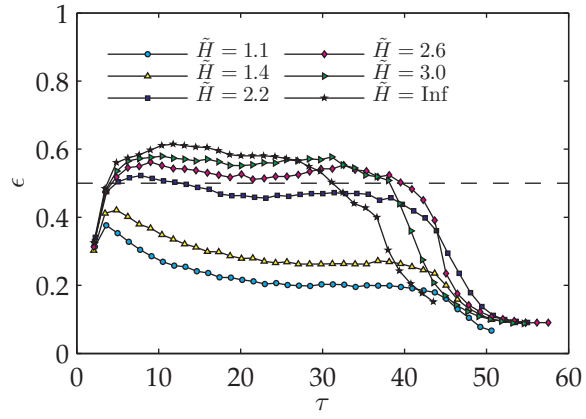

(c)

Figure 74: Measurements of the dimensionless crater depth Δ, width Ω and shape factor $\epsilon = \Delta/\Omega$ as a function of the dimensionless time τ for different dimensionless film thickness $\tilde{H}$. The dot line in (a) represents the value of the maximum crater depth in the deep pool case.

Classification

On the base of a literature review and of the performed study a new classification of the flow regimes for drop impacts onto liquid layers of finite thickness is suggested here. The classification cannot be only based on the ratio $\tilde{H}$ between the depth and the drop diameter, since impact velocity also influences the morphology of the impact. In other words, the classification has to be based on the relation between the depth of the liquid film and the kinetic energy of the impacting drop. In Figure 74a has been shown how the maximum depth of the crater, when it does not reach the bottom of the film, is similar to the maximum depth in a deep pool case. In addition, when this maximum depth is equal to the film thickness, there is the tuning phenomenon. Since the maximum depth of the crater in a deep pool case $\Delta_{max,deep}$ depends on the kinetic energy of the impacting drop, it is taken as parameter for the classification of the drop impacts onto film of finite thickness:

THIN FILMS: $\tilde{H} \lesssim \frac{1}{10}\Delta_{max,deep}$

The depth is so small that the impact phenomena are immediately strongly influenced by the pool bottom. The crater reaches soon the bottom wall and squashes on it, assuming an almost cylindrical shape. Its width increases in the early stage after the drop impact, than stagnates and successively reduces and there is no jet ejection. The formation of the crown is enhanced by the thin layer and it is the main feature of this class.

THICK FILMS: $\frac{1}{10}\Delta_{max,deep} < \tilde{H} \lesssim \frac{3}{2}\Delta_{max,deep}$

The impact phenomena experience the presence of the wall, but only a few time after the impact. The crater expansion is slowed and the crater is sooner perturbed by capillary waves. In the receding phase its shape tends to a cone from which an high speed jet is emitted.

DEEP POOLS: $\tilde{H} > \frac{3}{2}\Delta_{max,deep}$

The depth is so greater that the impact is not influenced by the bottom wall. The crater evolves with an almost hemispherical shape, which may be later perturbed by capillary waves. A thick jet is ejected from its center.

This classification is not rigorous and it have a meaning only for sufficiently high kinetic energy of the impacting drop. Obviously it has the disadvantage that, for given impact parameters, the reference parameter, i. e. the maximum crater depth in the deep pool case, is not known a priori. This problem will be face up in the next section, where a model to predict the maximum crater depth for a deep pool impact has been formulated

and a map of the maximum crater depth as a function of the impact parameters has been plotted.

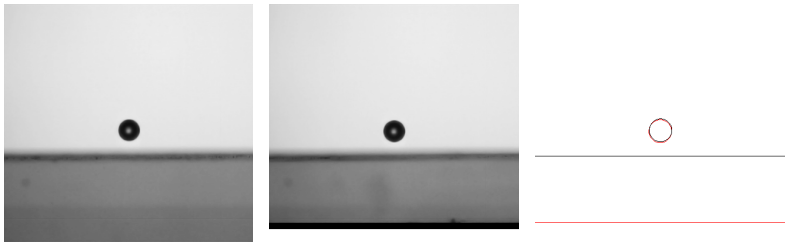

(a1) (b1) (c1)

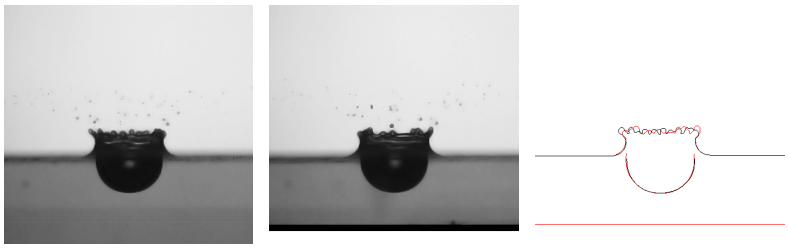

(a2) $\tau = 4.8$ (b2) $\tau = 4.8$ (c2) $\tau = 4.8$

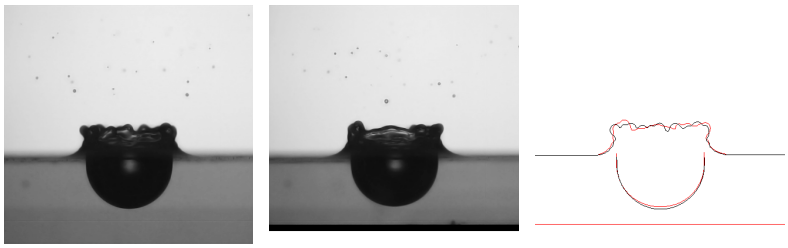

(a3) $\tau = 10.4$ (b3) $\tau = 10.4$ (c3) $\tau = 10.4$

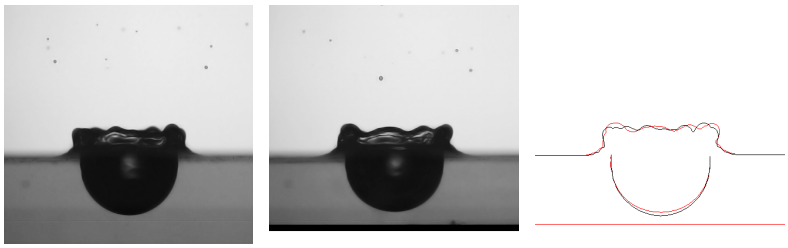

(a4) $\tau = 15.9$ (b4) $\tau = 15.9$ (c4) $\tau = 15.9$

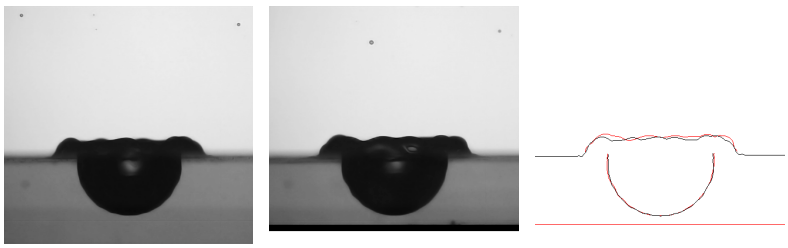

(a5) $\tau = 25.6$ (b5) $\tau = 25.6$ (c5) $\tau = 25.6$

Figure 75: Continue...

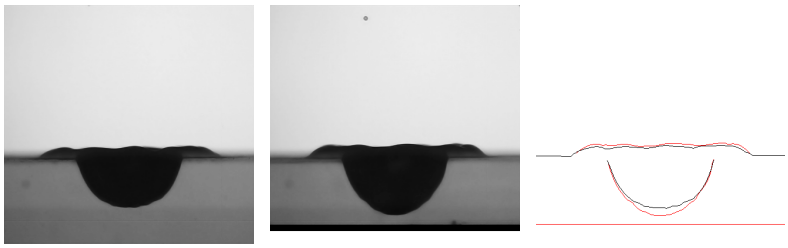

(a6) $\tau = 32.5$ (b6) $\tau = 32.5$ (c6) $\tau = 32.5$

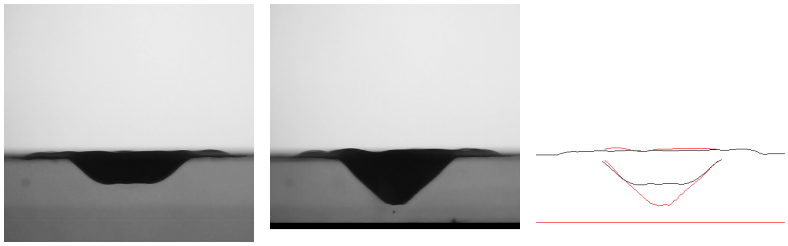

(a7) $\tau = 39.4$ (b7) $\tau = 39.4$ (c7) $\tau = 39.4$

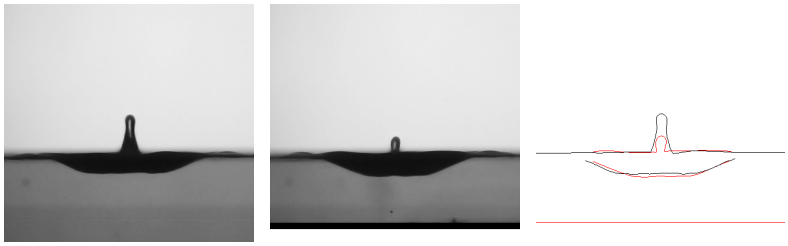

(a8) $\tau = 46.3$ (b8) $\tau = 46.3$ (c8) $\tau = 46.3$

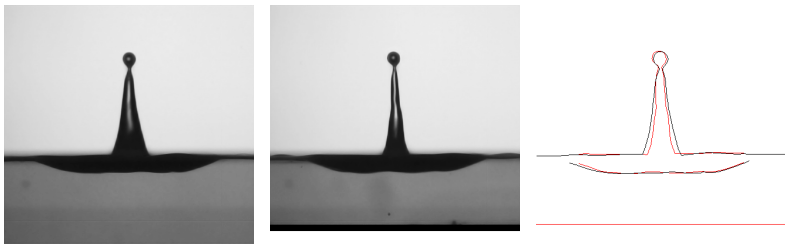

(a9) $\tau = 55.9$ (b9) $\tau = 55.9$ (c9) $\tau = 55.9$

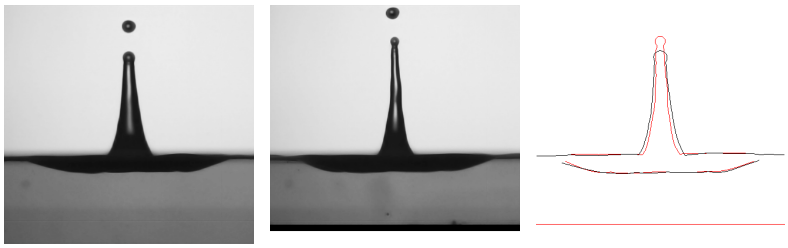

(a10) $\tau = 61.4$ (b10) $\tau = 61.4$ (c10) $\tau = 61.4$

Figure 75: Comparison between a drop impact onto a liquid layer of infinite (first column) and finite (second column) depth. In the second case the dimensionless pool depth is $\tilde{H} = 3.0$. Impact conditions are listed in Table 8.

6

DYNAMICS OF THE CRATER EVOLUTION

The temporal evolution of the crater formed by the impact of a drop onto a deep liquid pool has been experimentally and theoretically investigated. In the experimental part of this study the evolution of the crater has been observed using high-speed imaging and the geometry has been analyzed by image processing. Then a theoretical model has been developed which is aimed to predict the dynamics of the crater penetration for high Weber, Froude and Reynolds numbers. It is based on the assumption of an irrotational velocity field around the crater, associated with a moving and expanding sphere in an inviscid liquid. Such a velocity field is a good approximation near the crater bottom. The pressure field in the target liquid is obtained from the instationary Bernoulli equation, which accounts for the liquid velocity and acceleration, and gravity. The equations of motion of the crater are obtained from a balance of stresses at the crater bottom, accounting for surface tension and viscosity. The obtained system of ordinary differential equations has been solved numerically, using initial conditions obtained from experimental data and theoretical predictions. The model has been validated against experimental data for a wide range of impact parameters. The agreement is rather good. A map of the maximum crater depth as a function of the Weber and Froude number has been plotted.

6.1 REVIEW OF PREVIOUS STUDIES

Previous research fields

With the second world war phenomena of crater formation by the impact of an object on a semi-infinite target become to gain more attention, with the initial interest rose out to develop armors which could defeat projectiles (Byrnside and Torvick, 1971) or missiles that can resist to hypersonic impacts against rain droplets (Kinslow et al., 1972). Later, with the advent of space missions, the field extended to the study of impacts of micrometeorites on space vehicles. Meanwhile impact cratering in rocks had been of interest also to workers in the geosciences (Opik, 1937), with problems of scaling the results from small laboratory craters across more than 12 orders of magnitude (Gault and Moore, 1965). At high velocities inertial effects become dominant in comparison with the stresses associated with rheological or material properties. Under such conditions impact phenomena of metals

and rocks can be treated well are similar to the corresponding flows in liquids (Moore et al., 1962). For example, if a ductile metal sphere is fired against a solid target at increasingly higher velocities, a velocity is finally reached which results in a permanent deformation. If the impact velocity is increasing further such a sphere will flow radially during the impact as though it was liquid and the event is a special case of impact of a liquid drop against a solid. If the impact velocity is increased still further, liquefaction occurs not only of the impinging sphere but also of the solid target, like in case of impact of a liquid drop against a liquid (Engel, 1962).

Underwater noise of rain

Craters formed by drop impacts have been studied also because related to the underwater noise of rain, whose understanding permits the detection and characterization of rain over the oceans by remote acoustic sensors. In the mid-1970s, two factors were coming together to rekindle specific interest in the underwater noise of rain. One-as always with underwater noise studies-was the military need for a better understanding of the natural mechanisms of underwater noise, brought about by improvements in sound detection, signal processing, and the silencing of vessels. The other factor was the beginning of the use of acoustical techniques to probe phenomena of geophysical significance. Pumphrey et al. (Pumphrey et al., 1989, Pumphrey and Elmore, 1990, Prosperetti et al., 1989) made the decisive innovation with respect to earlier researches to photograph on the same frame both the physical event of drop impact and the trace of an oscilloscope driven by a hydrophone, showing that, in a restricted range of the impact parameters, small air bubble remain entrained in the liquid and this phenomenon is accompanied by a substantial acoustic emission, while all other stages of the process, including the impact itself, are relatively silent. They revealed that this primary bubble entrainment (and the relative typical sound emission) is not a random phenomenon as said by Franz (1959), but it always appears under well determined impact conditions. Oguz and Prosperetti (1990) performed a theoretical analysis to obtain the upper and lower limits of bubble entrapment and presented a comprehensive review and a numerical investigation of the phenomena related to this topic (Prosperetti and Oguz, 1993).

6.1.1 *Maximum crater depth*

Engel (1966) experimentally and analytically studied impacts of water drops on liquid pool in order to obtain information about the impact of micrometeorites on space vehicles. She built an impressive test system to get impacts of drops of $4-5\,\mathrm{mm}$ of

diameter falling from an height up to 19 m in reduced pressure conditions. She employed a suspension of white particles to show the flow of the target liquid and noted that the crater and the cylindrical wave together reach their maximum at about the same time and that there is no perceptible flow motion at about that time. Thanks to this observation, she developed an energy balance at that time, where kinetic energy terms where neglected. Assuming, as suggested by experimental observations, an hemispherical shape for the crater with center in the impacting point, Figure 76, she could obtain an analytical expression in the crater radius a_{cr}. She found a solution for the shape of the wave swell considering it to be formed by the fluid removed by the crater. Only the extension of the bubble surface was empirically estimated. Macklin and Metaxas (1976) carried out an experimental investigations of drop splashing on a deep pool and shallow films using water and solutions of ethanol and glycerol with water. In this way they obtained data for crater maximum depth with high viscosity and low surface tension respect to water. They performed an energy analysis similar to Engel, just adding some others terms, which they showed to be of negligible influence. They did not arbitrarily assume as Engel that only a fraction $c_{dr} = 0.5$ of the kinetic energy of the impacting drop is given to the target fluid, but they found that it should be in order to obtain a better agreement with experimental data. However this conclusion can be influenced from errors in the calculation of the energy terms and all later studies have assumed that all the kinetic energy of the impacting drop is given to the target fluid and that crater energy terms are the most important. Pumphrey and Elmore (1990) just compared the kinetic energy of the impacting drop with the gravity potential energy of the crater, founding the maximum crater depth proportional to $Fr^{1/4}$:

$$\Delta_{max} = c \cdot Fr^{1/4}, \tag{6.1}$$

where $c = 0.76$. Prosperetti and Oguz (1993) considered also the surface energy of the crater, but simplified the obtained equation assuming that $Bo^{-1} \ll Fr$, founding an equation similar to that of Pumphrey and Elmore, but with $c = 1.28$. Liow (2001) further proposed a different coefficient $c = 0.55$ performing a least square fitting of experimental data. Fedorchenko and Wang (2004) explained that Equation 6.1 is only a gravity asymptote and in general Bo cannot be neglected. All these proposed equations may be written in a common form starting from a general energy balance equation:

$$c_{dr}E_{dr} + U_{dr} + \sigma S_{dr} = U_{cr} + U_{sw} + \sigma\left(S_{cr} + S_{sw} + S_{cw}\right), \tag{6.2}$$

where E_{dr} and σS_{dr} are the kinetic and surface energy of the impacting drop, U_{dr}, U_{cr}, U_{sw} are the gravity potential energy of

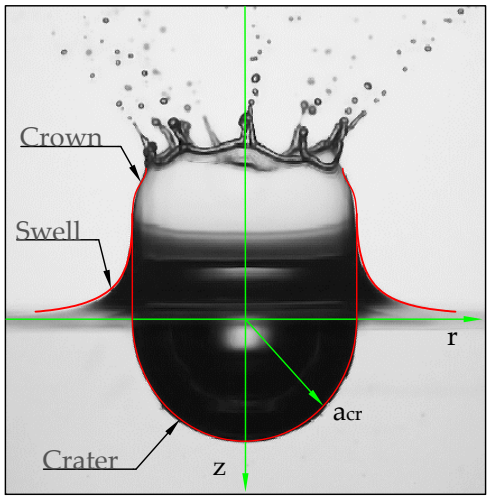

Figure 76: Sketch of the geometry assumed by Engel. The crater is hemispherical with center at the impact point. The part above the liquid surface is divided in two region: the liquid swell close to the surface and the cylindrical sheet (the crown) above. (Actually the profile of the crater highlighted in red is not exactly a portion of circle with center at the impact point, but it is an ellipse).

the drop, of the crater and of the wave swell and the last term in the *rhs* is the surface potential energy of the new net generated surface, where S_{cr}, S_{sw}, S_{cw} are the net-surfaces of the crater, of the wave swell and of the crown.

Following Engel approach the terms of Equation 6.2 may be analytically expressed as a function of the crater radius a_{cr}:

$$E_{dr} = \tfrac{1}{12}\pi\rho D^3 V^2\,, \tag{6.3a}$$
$$U_{dr} = \tfrac{1}{12}\pi g\rho D^4\,, \tag{6.3b}$$
$$\sigma S_{dr} = \pi\sigma D^2\,, \tag{6.3c}$$
$$U_{cr} = \tfrac{1}{4}\pi g\rho a_{cr}^4\,, \tag{6.3d}$$
$$U_{sw} = \tfrac{1}{36}\pi g\rho a_{cr}^4\,, \tag{6.3e}$$
$$\sigma S_{cr} = \pi\sigma a_{cr}^4\,, \tag{6.3f}$$
$$\sigma S_{sw} = 0.14\pi\sigma a_{cr}^2\,, \tag{6.3g}$$
$$\sigma S_{cw} \sim \pi\sigma a_{cr}^2\,, \tag{6.3h}$$

where proportionality have been used where an analytical expression has not been found and empirical data have to be used. Substituting Equation 6.3 in Equation 6.2, after non - dimensionalization, a general equation for the dimensionless maximum crater depth $\Delta_{max} = a_{cr,max}/D$ can be obtained:

$$\Delta_{max} = \sqrt{c_1 Bo^{-1} + \sqrt{c_2 Bo^{-2} + c_3 Bo^{-1} + c_{dr} c_4 Fr + c_5}}. \tag{6.4}$$

The values of the numerical coefficients c_1, c_2, c_3, c_4, c_5 depend on which term of Equation 6.2 is considered. The fraction c_{dr}

of the kinetic energy of the impacting drop that is given to the target liquid only affect the term with Fr of Equation 6.3. Considering all the terms but the last and $c_{dr} = 1$, the numerical coefficients take the (rounded) value of:

$$c_1 = -2.1\,, \tag{6.5a}$$
$$c_2 = +4.2\,, \tag{6.5b}$$
$$c_3 = +3.6\,, \tag{6.5c}$$
$$c_4 = +0.3\,, \tag{6.5d}$$
$$c_5 = +0.3\,. \tag{6.5e}$$

A comparison of the model against experimental data from the present work and from literature is shown in Figure 77, where also data from Brutin (2003), Cai (1988, 1989), Elmore et al. (2001), Olevson (1969) have been considered. The agreement is rather good, but, as expected, Engel data are well above the middle line, since the crown surface energy takes more importance for high speed impacts. Other energy sinks like those related to the gravity potential energy of the crown, to the viscous dissipations, to the secondary droplets, to the compression wave generated by the impact have been shown to be negligibly small for the range of the impact parameter considered, but for the kinetic energy of the cylindrical wave surrounding the crater, which, as pointed out by Olevson (1969), is moving outward before, during and after the crater reaches its maximum size. He also observed the crater to be a little more depth than wide and calculated almost the same energy terms of Engel assuming a prolate hemispherical shape for the crater. However he did not used them to obtain an expression for the maximum crater depth, but to partition the energy of the experimentally produced craters.

The gravity and capillary asymptotes may be found taking the limit of Equation 6.4 for $\sigma \to 0$ and $g \to 0$ respectively, obtaining two expressions similar to those suggested by Fedorchenko and Wang (2004):

$$\Delta_{\text{max,gravity}} = 0.74\,(1 + Fr)^{1/4}\,, \tag{6.6}$$
$$\Delta_{\text{max,capillary}} = (0.88 + 0.07We)^{1/2}\,. \tag{6.7}$$

Brutin (2003) has been the first to perform an analytical analysis of the crater evolution using a momentum balance approach. It modeled the crater as an expansion of a half-sphere and considered gravity and inertia contributes, obtaining:

$$\Delta_{\max} = \left(1 + \frac{5\sqrt{2}Bo^{\frac{5}{2}}}{24Bo + \frac{3}{2}Bo^2}Fr\right)^{\frac{1}{5}}\,, \tag{6.8}$$

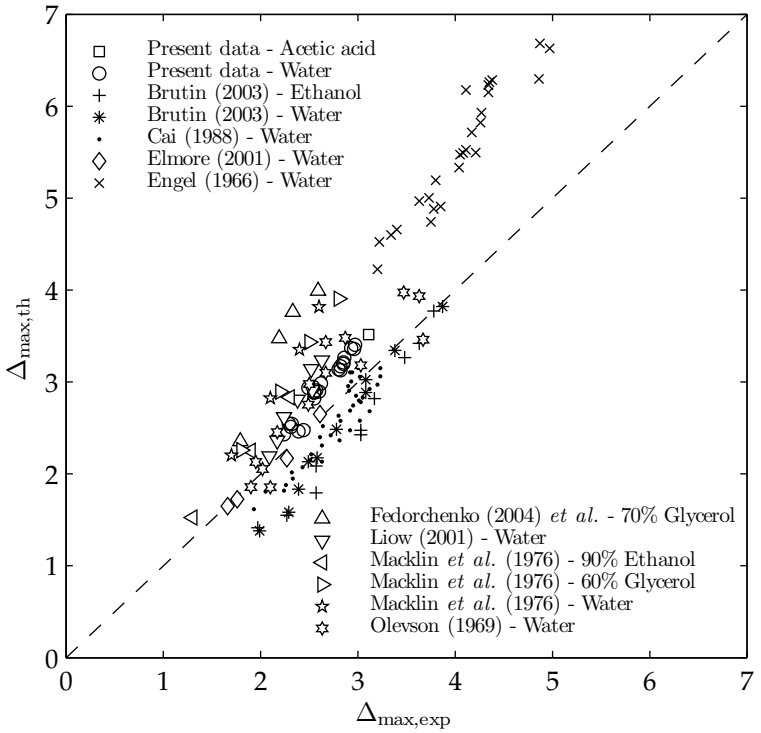

Figure 77: Maximum crater depth. Comparison of experimental data with predicted values from the energy balance of Equation 6.4 with the values of Equation 6.5.

with a good agreement with experimental data, but the variations in the Fr, now raised to $1/5$, are not accurately predicted.

6.1.2 *Crater evolution*

Engel (1967) obtained also an analytical expression for the crater evolution in time. She started from the approach she used for the crater's maximum depth and tried to obtained an explicit expression for the kinetic energy of the flow. From her experimental data she recognized a similarity between the flow around the expanding crater and the line of forces around one end of a bar magnet or with the stream lines produced by the movement of a solid sphere through a liquid. However, using potential theory, she only guessed by trials a velocity potential for the flow around the crater. In the end she found an expression including also viscous dissipation, which must be numerical integrated to give a solution in good agreement with her experimental data, but only for the growing phase:

$$\dot{\Delta} = \sqrt{\frac{0.12}{\Delta^3} - \frac{28.01}{We\,\Delta} - \frac{0.79\,\Delta}{Fr} - \frac{22.86}{Re}\int_0^\tau \Delta\dot{\Delta}^2 d\tau}\,. \tag{6.9}$$

The assumption of irrotational flow was confirmed later by Oguz and Prosperetti (1990), who pointed out that when the drop hits the pool surface, very little vorticity is generated by the impact. During the subsequent development of the crater, vorticity production at the free surface is minimal in view of the fact that Reynolds number is of order of thousands. Therefore, the flow can be assumed to be irrotational and can be considered as potential. Influence of viscosity on cratering processes may be relevant in other field, where it has been investigated, e. g. in Gault and Moore (1965).

The assumption of irrotational flow was used by Liow (2001), who proposed a scaling law for the time to reach the maximum crater depth, using an energetic approach and assuming the flow around the crater as the potential flow given by a point source. He stated that the choice has more physical meaning respect to that of Engel, but he didn't used it to obtain an expression for the crater evolution. The assumption is in fact well known in impact cratering studies (Holsapple and Schmidt, 1987, Merzhievsky, 1997).

Fedorchenko and Wang (2004) presented a theoretical model for the cavity submergence in the very early stage after drop impact, giving a constant velocity of penetration which is half of the velocity of the impacting drop:

$$\Delta = \tfrac{1}{2}\tau\,, \tag{6.10}$$

a confirmation of a well-known result from the penetration mechanics (Birkhoff et al., 1948, Yarin et al., 1995).

Berberovic et al. (2009) used the same potential flow assumed by Liow (2001), but with a new approach based on a momentum balance. They found a completely analytical solution for the crater penetration, but only for the first stage of the growing phase:

$$\Delta = 2^{-\frac{4}{5}}\,(5\tau - 6)^{\frac{2}{5}}\,. \tag{6.11}$$

This model does not predict the crater maximum depth since the surface tension and the gravity are not taken into account. This model has been the base of the model developed in the present study. It has been extended in order to include gravity, capillary and viscous effects.

6.2 EXPERIMENTAL OBSERVATIONS AND MEASUREMENTS

Several experiments were performed with water, varying both diameter and velocity of the impacting drop. Acetic acid was

Case	Fluid	D (mm)	V (m/s)	We	Fr	Bo	Re
a	w.	2.2	2.4	171	262	0.57	6385
b	w.	1.8	3.0	229	491	0.48	6768
c	w.	2.3	3.6	408	570	0.60	10119
d	w.	2.8	4.2	688	619	0.75	14624
e	a. a.	2.9	4.4	2190	694	1.24	12687

Table 10: List of impact parameters for five selected cases (w. is for water and a.a. is for acetic acid).

also used in order to reach higher Weber numbers. For each impact condition several acquisitions were performed and repeatability was checked. About 25 different events were analyzed but results of only 5 selected cases are presented here in Table 10. Cases *a* and *c* are respectively in the primary and secondary entrapment region, but this does not influence the present investigation.

Early stage after the drop impact

In the early stage after the drop impact the target fluid deforms under the effect of the impacting drop, which is quickly changing from a spherical shape to a thin sheet. In this stage the flat bottom of the crater in the recorded picture, see Figure 78a, is different from the shape of the crater of the target fluid, as evidenced in Figure 78b, which represents an impact of a dyed drop. It can be noticed how the real bottom of the crater of the target fluid is more hemispherical and filled by the liquid of the impacting drop. As the thickness of the flow of the impacting drop reduces, the detected crater, is practically the same as the shape of the target fluid. In the last phase of the receding a jet may be generated and ejected from the crater bottom. Also in this case the detected images do not exactly represent the shape of the crater of the target fluid, but only its horizontal projection.

Measurements

Crater depth was measured detecting the impact point O and the lower point C on the symmetry axis (see Figure 79). Crater width was measured detecting the top left and right points A and B, a little below the water level because capillary waves generated by the impact perturb their horizontal projection. Figure 80 and Figure 81 show the evolution in time of the dimensionless crater depth Δ and width Ω scaled by the drop diameter. On the curves of the depth, it can be seen how the influence of capillary waves is delayed in time and smaller with increasing We and Fr numbers, up to the case *e*, where the effect does not appear at all. The width exhibits the influence of the crown, causing slowing down of the expansion of the crater in the cases *a*, *b* with even

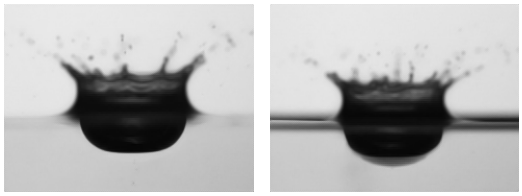

(a) $\tau = 1.90$ (b) $\tau = 3.02$

Figure 78: Difference between the impact of a water drop (a) and the impact of a dyed water drop (b). In (b) the fluid of the pool can be distinguished from the fluid of the impacting drop. At the early stage of the impact, the shape of the crater in the target fluid is more spherical of what would appear in the normal recorded images, which are only a horizontal projection of the liquid-air interface.

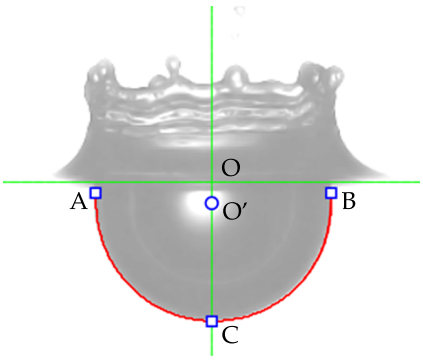

Figure 79: Detection of the crater and of its characteristics points. O is the impact point, A, B and C are the top left, right and bottom points, which may be fitted by a circle having center in O′.

a transitory reduction of the width in the cases c, d, while in the case e the width increase smoothly.

Due to a different behavior of depth and width evolution, the shape factor $\epsilon = \Delta/\Omega$ of the crater is not constant, but varies in time, as showed in Figure 82. There is however a central region where eccentricity seems to have an almost constant value, meaning that depth and width are increasing at a similar velocity. Figure 83 shows a superposition of the crater profiles in different time steps of the growing phase for the case d of Table 10, where the radial coordinate x and the vertical coordinate z are non-dimensionalized with the crater depth Δ and width Ω, obtaining the dimensionless coordinates ξ and ζ. The similarity of the shape means that not only depth and width, but all the crater points are growing at a same rate during this expansion stage.

Crater shape

From Figure 82 it is clear that the projection of the crater is not a perfect semi-circle with its center at the impact point, as considered in all the previous analytical models. Looking for a simple representation of the crater shape, this may lead to at least two interpretations. The first is that it may better be represented by a semi-oval rather than a semi-circle. The second is that it may still be represented as a portion of a circle, but with center non coincident with the impact point. This representation may be preferable from the point a view of an analytical investigation since a circle can be completely represented, in an suitable reference system, by only one parameter, while an oval needs at least two parameters. The validity of the second approach has been checked experimentally. After edge detection, the points forming the crater profile were interpolated with a circle and its center was tracked on the images. Two methods have been used. The former is the simple fitting of the circle passing through the three points A, B, C of Figure 79. The latter is a best fit interpolation of all the points of the crater profile with a circle, using a method by Pratt (1987). Both methods yield a very similar radius and position of the center. Using this interpretation, from Figure 82 it is evident how the center goes from above to below the target surface and then again below. Thus, for sufficiently high Weber and Froude numbers, if the crater shape is represented as a portion of a sphere, its center is not continuously located at the impact point. It is also clear that the growing phase can be represented as an expanding sphere, while the receding phase cannot be represented by a regressing sphere, but as an always expanding sphere, since the width does not reverse its behavior as the depth.

Crater curvature

It has been shown that if the crater shape is represented by an hemisphere, its center is not located at the impacting point. To check if the shape is effectively spherical, measurements of local

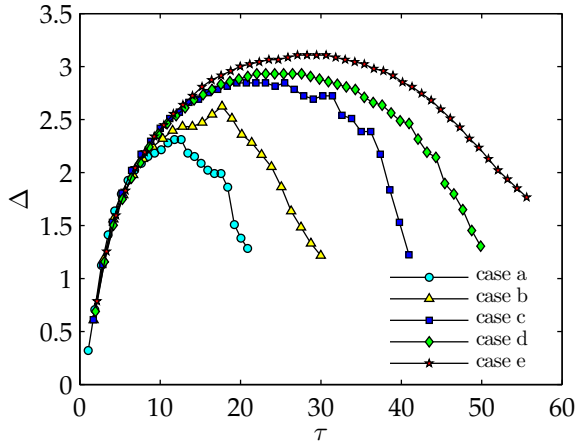

Figure 80: Measurements of the dimensionless crater depth Δ as a function of the dimensionless time τ.

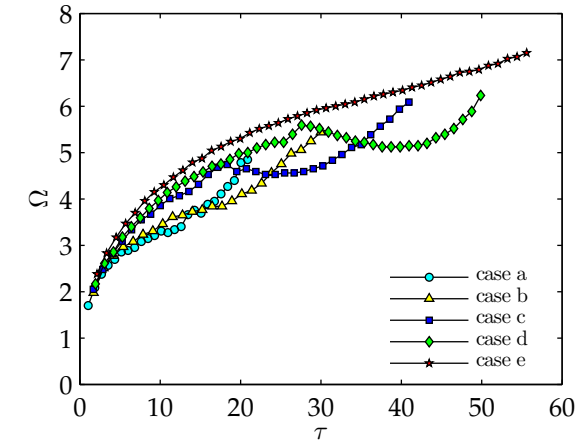

Figure 81: Measurements of the dimensionless crater width Ω as a function of the dimensionless time τ.

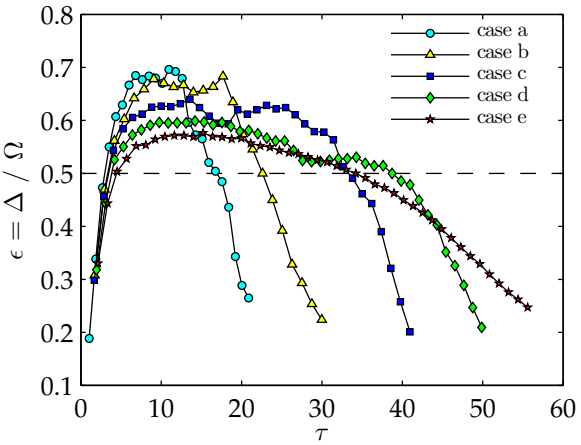

Figure 82: Measurements of the crater shape factor $\epsilon = \Delta/\Omega$ as a function of the dimensionless time τ.

curvature has been performed. Since the crater edge is known in a discrete form, the curvature has been measured on each point of the crater with the Pratt method, taking approximately 41 pixels (about 1/8 of the total) for each measurement. Obviously this measurement cannot be applied to the first points of the crater close to the water surface. Results at three selected time instants for the case *d* of Table 10 are showed in Figure 84. The ordinate is the local measured radius non-dimensionalized using the global radius calculated fitting the three representative points. The abscissa is the vertical z-position of the point where the measurement is performed, non-dimensionalized with the crater depth. The left and right sides refer to the left and right side of the crater respect to the impact point. At time $\tau = 5.26$ the crater seems to have a flat bottom; however the profile detected in the pictures refers to the position of the liquid-air interface, which does not coincide to the crater profile of the target fluid in the early stage after the impact, when the thickness of the impacting drop is not negligible (as explained little above). At time $\tau = 7.49$ and $\tau = 11.94$ the drop is more flatten and the measured shape of the crater is very close to a spherical shape in the central region. On the external sides the curvature begins to increase, meaning that the wall of the crater tends to become vertical close to the water surface, down to about the 30 % of the crater depth. The same general behavior has been detected in the other cases, but for lower impact conditions it is not possible to perform this measurement for the entire growing phase since capillary waves start earlier to deform the crater profile.

Stagnation line

A last interesting feature, already recognized by Cole (2007), is the existence of a stagnation circle during the last stage of the receding phase. As shown in Figure 85, while the width keeps increasing and the depth decreasing, there is a line (a circle) that does not move.

Similarity with a moving expanding sphere

The experimental investigation has evidenced the shape of the crater to be similar to a portion of a sphere for sufficiently high Weber, Froude and Reynolds numbers, specially around the crater bottom. Its center is not located at the impact point, but varies in time from above to below to above the target surface. In the end the crater seems to behave like a portion of a moving and expanding sphere.

6.3 THEORETICAL MODEL FOR CRATER EVOLUTION

Two stages of drop impact

In the present study two stages of drop impact are considered. The first stage, $t \lesssim 2D/V$, is characterized by the initial drop deformation and crater formation. The crater evolution is governed by the flows in the liquid pool and in the deforming drop and

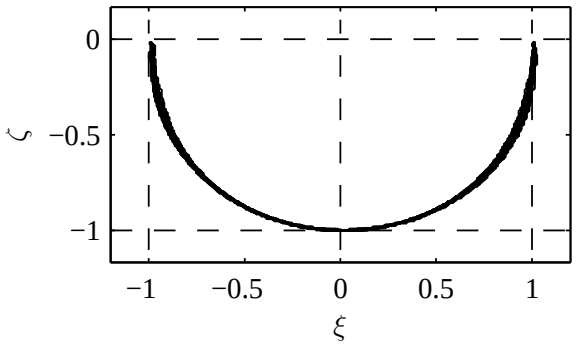

Figure 83: Superposition of the crater profiles in the dimensionless time interval 6.36-21.96 for the case *d* of Table 10.

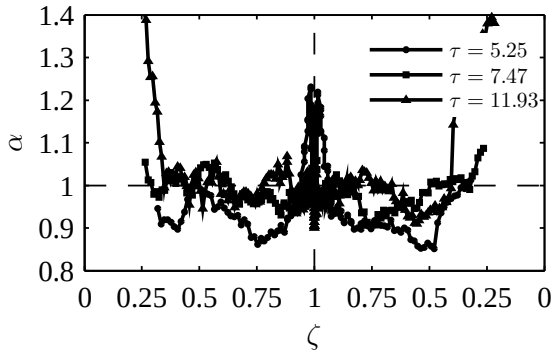

Figure 84: Local curvature in the crater for the case *d* of Table 10..

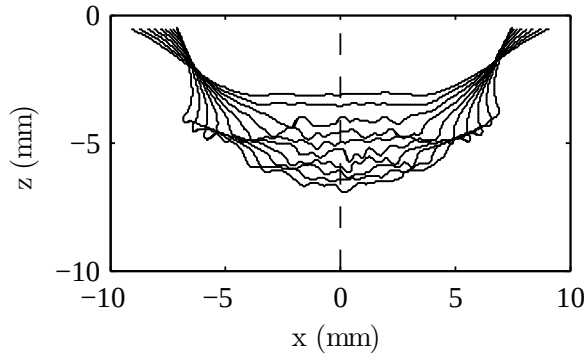

Figure 85: Crater profile in the dimensionless time interval 42.02-55.40 for the case *d* of Table 10. The profiles of the receding crater all have two common points, which locate a stagnation line.

by the stresses associated with these flows. In the second stage, $t \gtrsim D/V$, the drop is almost completely deformed, forming a thin liquid layer on the crater surface. The stresses in the drop region are small. Therefore the crater surface can be considered as a free interface. During this stage the inertial effects of the flow in the liquid pool are balanced by the surface tension and gravity.

6.3.1 *Flow field in the liquid pool*

The shape of the crater (or in the initial stage the drop/target liquid interface) can be well approximated as a portion of a sphere, at least close to the crater bottom. During the initial growing phase its center moves downward along the symmetry axis, than it is almost fixed a little below the surface and successively it moves upwards during the receding phase. In potential flow theory the flow around a moving sphere is well known and its similarity to the flow field around the crater was already recognized by Engel (1966) in her experimental investigation and can be checked in the PIV measurements of Cole (2007) or in some numerical simulations (Morton et al., 2000). Generally, in the absence of gravity, a spherically symmetric flow and stress fields can be found which satisfy the boundary conditions at the crater surface far from the free surface of the reservoir. The hydrostatic stresses associated with gravity destroy the spherical symmetry even at the bottom of the crater. Therefore, the gravity effects cannot be accounted for using the simple flow associated with the expansion of a spherical cavity with fixed center. In the present study the crater shape is approximated by a moving and expanding sphere.

Reference frame

Consider a reference frame fixed at the impact point O with the x-axis lying on the unperturbed liquid surface and the z-axis (impact axis) directed normal to it, as in Figure 86. Consider also a moving spherical coordinate system $\{r, \theta, \varphi\}$ with the origin at the center O' of the spherical cavity, where r is the radial coordinate and θ is the zenith angle. The radius of the crater in the relative spherical reference system is denoted by $a_{cr}(t)$ and the z position of its center on the symmetry axis by $z_{cc}(t)$.

Flow potential

A relative irrotational flow around the cavity in the moving coordinate system satisfying the Laplace equation

$$\Delta\phi = 0, \tag{6.12}$$

can be obtained as a superposition of a uniform flow and flows generated by a source and doublet located at the center O' (Lamb,

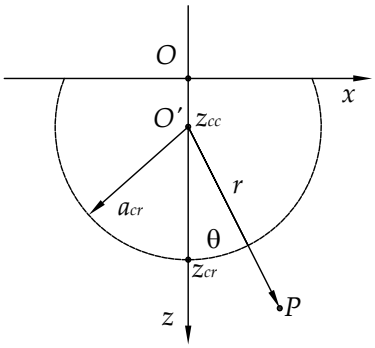

Figure 86: Sketch of the cavity and definition of the fixed and moving reference frames.

1932, Batchelor, 1967, White, 2002):

$$\phi = -Ur\cos\theta - \frac{m}{r} - \lambda\frac{\cos\theta}{r^2}, \tag{6.13}$$

where ϕ is the flow potential and U, m, λ are time-dependent parameters characterizing the strength of the three elementary flows. They can be related to the position of the center z_{cc} and to the radius a_{cr} of the moving expanding sphere, representing the crater, as follows:

$$U(t) = \dot{z}_{cc}(t), \tag{6.14a}$$
$$m(t) = a_{cr}^2(t)\,\dot{a}_{cr}(t), \tag{6.14b}$$
$$\lambda(t) = \tfrac{1}{2}U(t)\,a_{cr}^3(t). \tag{6.14c}$$

The velocity components of the relative velocity field $\boldsymbol{u} = \boldsymbol{\nabla}\phi$ are obtained in the following form:

$$u_r = \dot{a}_{cr}\frac{a_{cr}^2}{r^2} - \left(1 - \frac{a_{cr}^3}{r^3}\right)\dot{z}_{cc}\cos\theta, \tag{6.15a}$$
$$u_\theta = \left(1 + \frac{a_{cr}^3}{2r^3}\right)\dot{z}_{cc}\sin\theta. \tag{6.15b}$$

This velocity field satisfies the kinematic boundary conditions at the crater surface $r = a_{\mathrm{cr}}$ and far from the cavity at $r \to \infty$. A similar velocity field (without expansion) was already used in studies about the rising of bubbles (Davies and Taylor, 1950, Joseph, 2003).

Bernoulli equation and pressure distribution

Pressure can be now determined using Bernoulli equation, which has to include an additional term accounting for the acceleration of the moving coordinate system:

$$\frac{\partial\phi}{\partial t} + \frac{1}{2}|\boldsymbol{\nabla}\phi|^2 + \frac{p}{\rho} = f(t) + gz - \dot{U}r\cos\theta, \tag{6.16a}$$
$$z = z_{cc} + r\cos\theta. \tag{6.16b}$$

Here f is a function depending only on time which has to be determined from the boundary conditions. Since the pressure

field far from the cavity, $r \to \infty$, is determined by the hydrostatic pressure, $p \to \rho g z$, equation Equation 6.16 yields

$$f(t) = \frac{1}{2} U^2. \tag{6.17}$$

The pressure distribution $p_{cr}(\theta, t)$ in the liquid at the crater surface, $r = a_{cr}$, can now be obtained from the pressure field Equation 6.16 with the help of Equation 6.13 and Equation 6.17:

$$\begin{aligned} \frac{p_{cr}}{\rho} = \frac{U^2}{2}\left(1 - \frac{9}{4}\sin^2\theta\right) + g(z_{cc} + a_{cr}\cos\theta) + \\ + \frac{a_{cr}\dot{U}}{2}\cos\theta + \frac{3\dot{a}_{cr}^2}{2} + a_{cr}\ddot{a}_{cr} + \frac{3}{2}\dot{a}_{cr} U \cos\theta\,. \end{aligned} \tag{6.18}$$

The expression for the pressure (Equation 6.18) contains two unknown functions, a_{cr} and z_{cc}, which have to be determined from the dynamic boundary conditions at the crater surface accounting for the capillary and viscous forces.

6.3.2 *Initial stage of drop deformation*

Drop and target liquid flows

After the drop impacts on the liquid layer, two different flows can be distinguished: one in the target fluid and one in the deforming impacting drop. During the first instants both strongly interact, but the second quickly becomes less important on the overall phenomenon, as the drop flattens on the growing crater.

Early velocity of penetration

The velocity of penetration of the drop/target interface at the time period $t \lesssim 2D/V$, during which the drop deforms, is approximately half of the impact velocity. This result is well-known from the penetration mechanics (Birkhoff et al., 1948, Yarin et al., 1995) and was already used for the description of drop impact (Fedorchenko and Wang, 2004, Berberovic et al., 2009).

In this study the quasi-stationary model of initial drop penetration is modified to account for the flow associated with the cavity expansion. The distribution of the stresses on the drop/outer liquid interface is not known. However, the pressure in the deforming drop at the impact axis, $\theta = 0$, can be easily estimated from the Bernoulli equation for steady flows, whereas the pressure in the outer liquid can be evaluated using Equation 6.18 neglecting the small gravity terms and the terms associated with acceleration:

$$\begin{aligned} \frac{p_{cr}(\theta = 0)}{\rho} &= \frac{U^2}{2} + \frac{3\dot{a}_{cr}(\dot{a}_{cr} + U)}{2} \\ &= \frac{(V - U - \dot{a}_{cr})^2}{2}, \end{aligned} \tag{6.19}$$

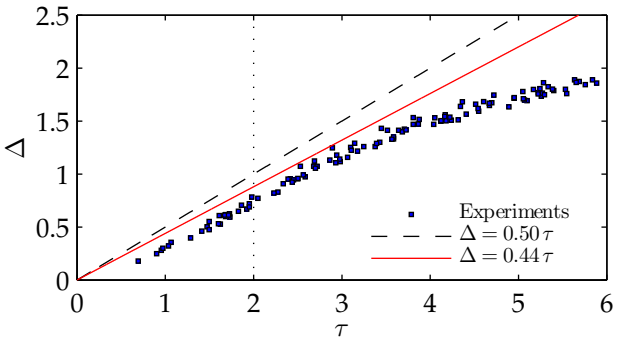

Figure 87: Experimental and theoretical values for the dimensionless crater depth Δ at the initial stage for various impact parameters. Lines represent the theoretical curves, markers indicate the experimental values.

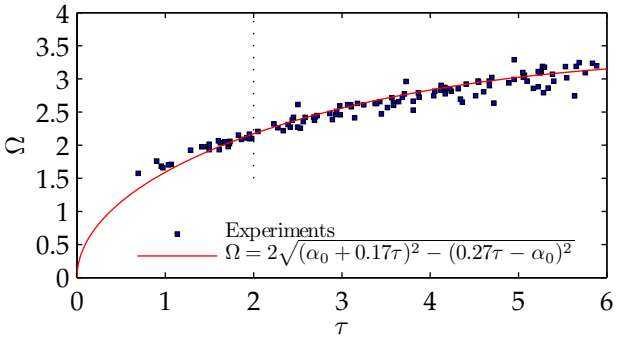

Figure 88: Experimental and interpolated values for the dimensionless crater depth Ω at the initial stage for various impact parameters. Lines represent the interpolated curves, markers indicate the experimental values. $\alpha_o = 0.77$ has been found with a least mean square method.

where $(U + \dot{a}_{cr})$ is the velocity of propagation of the cavity tip, and $(V - U - \dot{a}_{cr})$ is the velocity of drop deformation.

Another equation is obtained from the condition of vanishing pressure p_{cr} at the free cavity surface at $z = 0$. If the center of the sphere is located near to the liquid pool surface then this conditions yields

$$\frac{p_{cr}(\theta = \pi/2)}{\rho} = -\frac{5U^2}{8} + \frac{3\dot{a}_{cr}^2}{2} = 0. \tag{6.20}$$

The roots of the system Equation 6.19 - Equation 6.20 give the two components of the velocity of penetration of the crater:

$$U = \frac{-6 - \sqrt{15} + 3\sqrt{9 + 2\sqrt{15}}}{5 + \sqrt{15}} V \approx 0.27V\,, \tag{6.21}$$

$$\dot{a}_{cr} = \frac{1}{2}\sqrt{\frac{5}{3}} U \approx 0.17V, \tag{6.22}$$

the first is due to the rigid translation of the sphere, the second to its expansion. The penetration velocity is therefore:

$$\dot{\Delta} = U + \dot{a}_{cr} \approx 0.44\,V\,, \tag{6.23}$$

which is very close to the experimental data, presented in Figure 87 in dimensionless form using the drop initial diameter D as the length scale and the impact velocity V as the velocity scale. The dimensionless crater radius and the axial coordinate of the center of the sphere and the penetration depth of the crater are denoted as:

$$\alpha = a_{cr}/D\,, \tag{6.24}$$

$$\zeta = z_{cc}/D\,, \tag{6.25}$$

$$\Delta = \zeta + \alpha. \tag{6.26}$$

Noting that $\Delta = 0$ at $\tau = 0$ these dimensionless parameters can be estimated in the following form:

$$\dot{\alpha} \approx 0.17\,, \tag{6.27a}$$

$$\alpha \approx \alpha_0 + 0.17\,\tau\,, \tag{6.27b}$$

$$\dot{\zeta} \approx 0.27\,, \tag{6.27c}$$

$$\zeta \approx -\alpha_0 + 0.27\,\tau\,, \tag{6.27d}$$

where α_0 is a constant associated with the initial cavity radius. It can be estimated by a fitting of the dimensionless width Ω of the crater, using the following geometrical condition:

$$\Omega = 2\sqrt{\alpha^2 - \zeta^2} \approx 2\sqrt{(\alpha_0 + 0.17\tau)^2 - (0.27\tau - \alpha_0)^2}. \tag{6.28}$$

In Figure 88 the experimental data for Ω are compared with the estimation Equation 6.28, showing rather good agreement in the range $2 < \tau < 4$, where the constant $\alpha_0 = 0.77$ is obtained by fitting. It is obvious that the parameters of Equation 6.27 do not depend on the impact parameters of the drop if the Reynolds, Weber and Froude numbers are high.

6.3.3 *Crater expansion and receding*

6.3.3.1 *Inviscid flow*

Balance of stresses on the crater bottom

At large times the pressure gradient in the thin drop spreading on the expanding crater is negligibly small. The Young-Laplace equation applied to the crater surface

$$p_{cr} + \frac{2\sigma}{a_{cr}} = 0\,, \tag{6.29}$$

cannot be satisfied exactly over the entire cavity surface. On the other hand expression (Equation 6.18) can be linearized near the cavity bottom, $\theta \approx 0$. The dynamic boundary condition can then be written in the form:

$$\begin{aligned} 0 = &-\frac{7U^2}{4} + gz_{cc} + \frac{3\dot{a}_{cr}^2}{2} + a_{cr}\ddot{a}_{cr} + \frac{2\sigma}{\rho a_{cr}} \\ &+ \left[\frac{9U^2}{4} + ga_{cr} + \frac{a_{cr}\dot{U}}{2} + \frac{3\dot{a}_{cr}U}{2}\right]\cos\theta \\ &+ O(U^2\theta^4). \end{aligned} \tag{6.30}$$

It should be noted that at large times $U \ll \dot{a}_{cr}$ since in all the considered cases the Froude number is small, therefore the last term in Equation 6.30 is negligibly small in comparison with other terms. Condition Equation 6.30 yields the system of ordinary differential equations for $a_{cr}(t)$ and $z_{cc}(t)$ which can be written in a dimensionless form:

Governing equations

$$\ddot{\alpha} = -\frac{3}{2}\frac{\dot{\alpha}^2}{\alpha} - \frac{2}{\alpha^2 We} - \frac{1}{Fr}\frac{\zeta}{\alpha} + \frac{7}{4}\frac{\dot{\zeta}^2}{\alpha}\,, \tag{6.31}$$

$$\ddot{\zeta} = -3\frac{\dot{\alpha}\dot{\zeta}}{\alpha} - \frac{9}{2}\frac{\dot{\zeta}^2}{\alpha} - \frac{2}{Fr}\,. \tag{6.32}$$

Equation 6.32 may be connected to a Riccati equation in ζ using α as a time-dependent parameter. It has the following analytical solution:

$$\begin{aligned} \zeta(\tau) = &\frac{2}{9}\log\left[\cos\left(\frac{3(-\tau + 2Fr\alpha c_1)\sqrt{4\alpha^2 - Fr\dot{\alpha}^2}}{2\alpha\sqrt{Fr}}\right)\right] \\ &- \frac{\tau\dot{\alpha}}{3\alpha} + c_2\,, \end{aligned} \tag{6.33}$$

where c_1 and c_2 are two constants. However, after the substitution of Equation 6.33 in Equation 6.31, an analytical solution has not been found. For this reason the evolution of the crater has been evaluated by numerical integration of the system Equation 6.31-Equation 6.32 subject the initial conditions Equation 6.27.

6.3.3.2 *Effect of viscosity*

At high Reynolds number flows the viscosity effects lead to the appearance of the viscous boundary layer near the crater free surface. This thin viscous flow ensures the shear stress free surface of the crater. On the other hand, since the layer is thin the jump of the normal stresses through this layer is negligibly small. The Young-Laplace equation which accounts for the viscous stresses can be rewritten as

$$p_{cr} + \frac{2\sigma}{a_{cr}} - 2\mu\frac{\partial u_r}{\partial r} = 0 \quad \text{at} \quad r = a_{\text{cr}} \text{ and } \theta = 0\,, \tag{6.34}$$

where the radial velocity of the outer flow u_r is defined in Equation 6.15. The modified equation for the crater expansion is:

$$\ddot{\alpha} = -\frac{3}{2}\frac{\dot{\alpha}^2}{\alpha} - \frac{2}{\alpha^2 We} - \frac{1}{Fr}\frac{\zeta}{\alpha} + \frac{7}{4}\frac{\dot{\zeta}^2}{\alpha} - \frac{4\dot{\alpha}}{\alpha^2 Re}, \tag{6.35}$$

$$\ddot{\zeta} = -3\frac{\dot{\alpha}\dot{\zeta}}{\alpha} - \frac{9}{2}\frac{\dot{\zeta}^2}{\alpha} - \frac{2}{Fr} - \frac{12\dot{\zeta}}{\alpha^2 Re}. \tag{6.36}$$

It should be noted that results of computations of the crater depth using the systems Equation 6.31-Equation 6.32 and Equation 6.35-Equation 6.36 in the considered range of impact parameters are practically undistinguishable, which indicates the fact that the effect of viscosity is negligibly small.

6.4 RESULTS AND DISCUSSION

Fitted parameter

In order to validate the theoretical model for crater penetration at large times the system of differential equations is solved numerically, subject to the initial conditions described in Section 6.3.2. One fitted parameter is the time corresponding to the complete drop erosion in the crater. This time instant τ^* manifests the switch from the initial stage of drop deformation to the long-time stage of cavity expansion due to liquid inertia. It can be easily shown that the duration of the initial phase is comparable with $\tau \sim 2$. In our simulations the time instant $\tau^* = 2.3$ is

chosen, leading to the following initial conditions:

$$\alpha = 1.12\,, \tag{6.37a}$$
$$\dot{\alpha} = 0.17\,, \tag{6.37b}$$
$$\zeta = 0\,, \tag{6.37c}$$
$$\dot{\zeta} = 0.27\,. \tag{6.37d}$$

Model validation

A comparison between the model prediction and the experimental data is showed in Figure 89. The agreement is rather good. The difference between experimental data and predicted values increases at the last part of the receding phase. Some discrepancy between the predictions and the experiments can be explained by the influence of the crater shape by the propagating of the capillary waves (not considered in the theory) and by the crater deformation at the bottom part, leading to the formation of the central jet. Cases *a* and *b* have low impact velocity and capillary waves soon significantly deform the crater shape; however the model still predicts quite well the overall behavior, especially in the growing phase, when the crater shape is more spherical. Cases *c*, *d* and *e* have always more and for more time a spherical shape of the crater and the agreement of the model is better.

The validity of the presented model is extended to higher impact velocities, as is revealed in Figure 90, by a comparison with experimental data from Engel (1966), where also the predicted curves from the analytic models of Berberovic et al. (2009), Engel (1967) and Fedorchenko and Wang (2004) are shown. It is evident that the capability of the present model to predict also the maximum depth, the time of maximum depth and a general receding phase is also high.

Graphical superposition

Figure 91 shows a superposition of the crater predicted by the analytical model to the recorded images for the case *d* of Table 10. The agreement between the theoretical predictions and the experimental shape of the cavity is rather good at the bottom region of the crater ($\theta \ll 1$) where the model is valid. The difference between the model and the real images in (a)-(c) is not due to a poor accuracy of the model, but to what explained in Section 6.2 about the initial stage after the drop impact. During the following expansion phase, (d)-(g), the model predicts well the depth of the crater and the position of its center, as well as in the early receding phase (h)-(i). During the last receding phase the modeled crater radius and the position of its center do not agree very well with the experimental data, while the predicted crater depth is still predicted with a certain accuracy. This is because the assumed flow Equation 6.15 is a good approximation close to the crater bottom, but it degrades far away. In particular it cannot represent the modification of the flow field due to the crown.

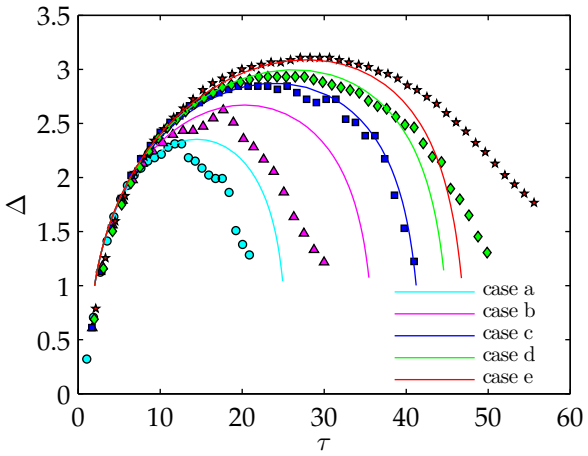

Figure 89: Comparison between experimental data (dots) and values predicted by the present model (lines) for the cases of Table 10. Cases *a* and *b* are below the range of validity of the model, since the capillary waves soon deform the sphericity of the crater.

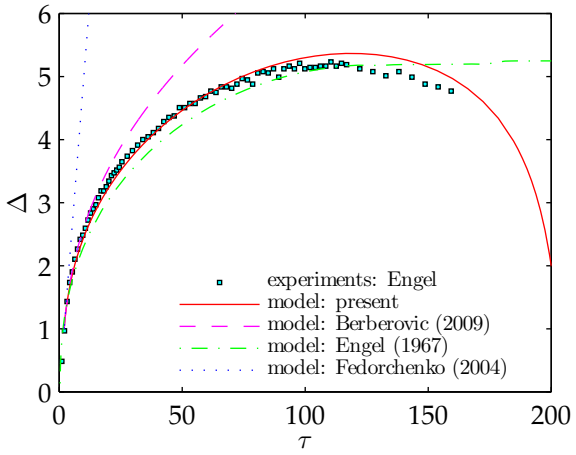

Figure 90: Comparison between the experimental data from Engel (1966) and values predicted by the present model and by the models of Berberovic et al. (2009), Engel (1966), Fedorchenko and Wang (2004).

In the model the z-position of the center rises sooner above the unperturbed liquid surface than in the real cases, where the fluid falling down from the crown slows down the upward receding motion of the crater bottom. In addition in the last stage of the receding phase the crater develop a jet at its center, which is also not accounted for in the model.

Maximum crater depth

The maximum crater depth and the time at which it is reached can be predicted by the model by numerically differentiating its solution. Figure 92 shows a good agreement of the predicted values with respect to the present experimental data and to the experimental data available in literature. In Figure 93 the results of the theoretical predictions of the dimensionless maximum crater depth are shown as a function of the Weber and Froude numbers. This map allows to predict the maximum crater depth for a deep pool impact and may be used to classify the depth of the target liquid layer, as explained in Section 5.3.

Map

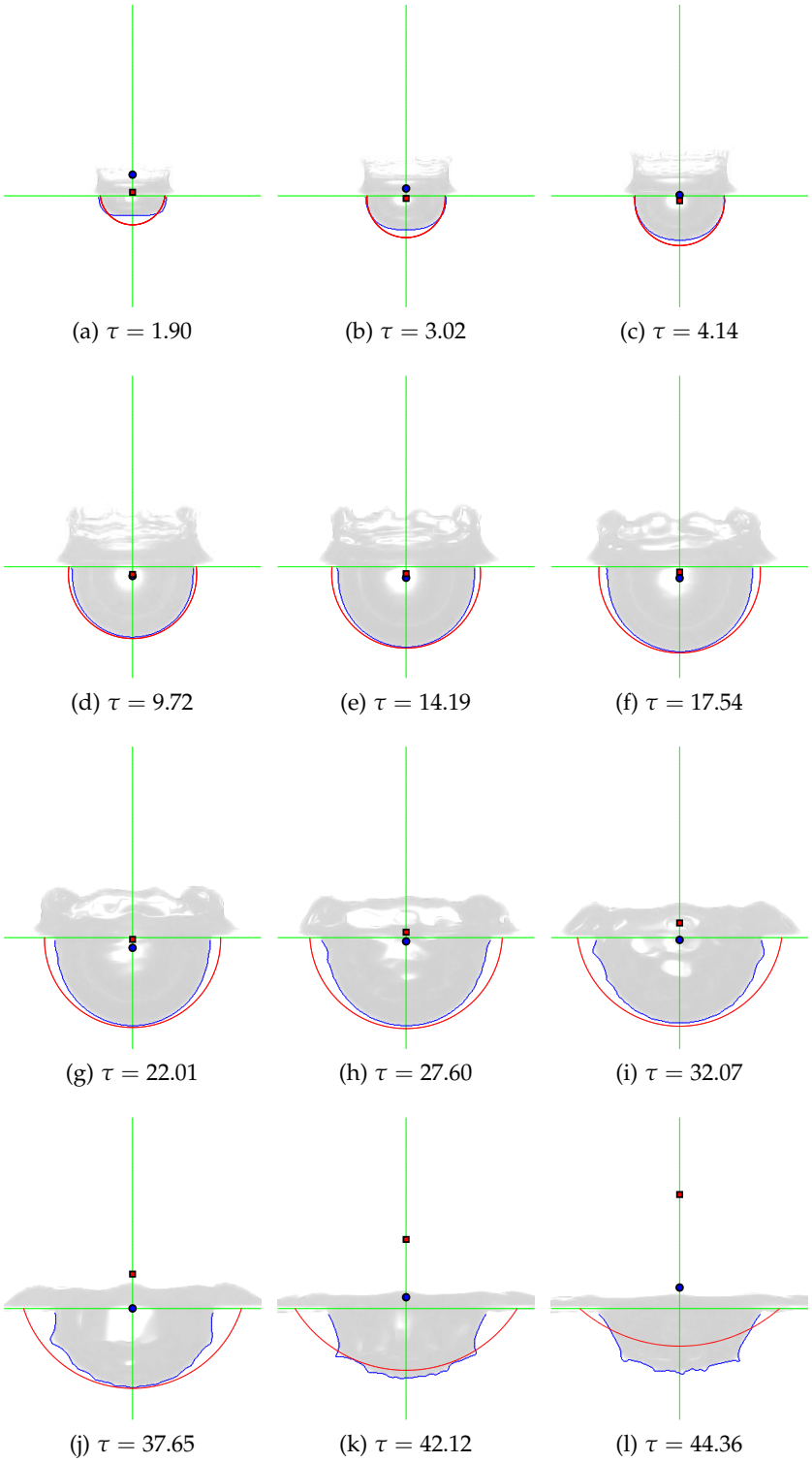

(a) $\tau = 1.90$ (b) $\tau = 3.02$ (c) $\tau = 4.14$

(d) $\tau = 9.72$ (e) $\tau = 14.19$ (f) $\tau = 17.54$

(g) $\tau = 22.01$ (h) $\tau = 27.60$ (i) $\tau = 32.07$

(j) $\tau = 37.65$ (k) $\tau = 42.12$ (l) $\tau = 44.36$

Figure 91: Superposition of the result of the proposed analytical model to the recorded images. The round point represent the center of the circle fitting the points A, B, C sketched in Figure 79. The square point represent the center of the modeled crater. Luminosity of the images has been increased for visualization reasons.

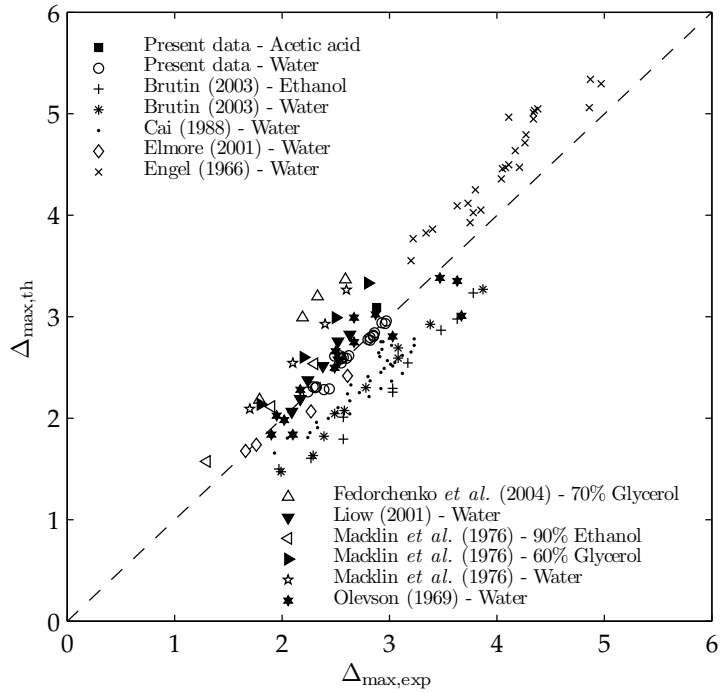

Figure 92: Maximum crater depth. Comparison of experimental data with predicted values from the presented model Equation 6.31.

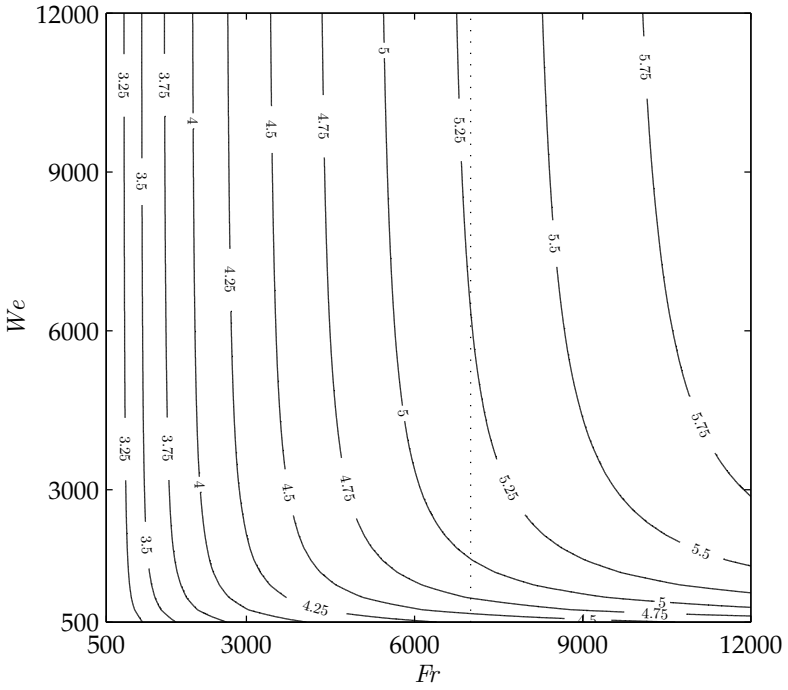

Figure 93: Predicted dimensionless maximum crater depth as a function of the impact parameters. The values of the maximum crater depth are indicated on the isolines. The values on the left side of the dot line have been validated in Figure 92, the values on the right side are extrapolations.

7

CONCLUSIONS

7.1 SUMMARY OF THE STUDY AND OF THE RESULTS

Experimental setup

An experimental setup for the high-speed-imaging investigation of interface phenomena have been developed. Particular attention has been paid in many details, in order to record images sharp enough to allow automate image processing. A MATLAB procedure have been written for the automatic digital image processing of drop impact sequences, which is able to measure impact parameters and crater features.

Single drop impacts onto a deep pool

Single drop impacts onto a deep pool have been studied in relation with the extensive existing literature. A new classification of the flow regimes has been suggested and a new "trampoline" regime has been detected and described. The formation of a dome above the target surface, typical of high speed impacts, has been obtained with unprecedented low impact parameters. The phenomenon has been observed to be favorite by the sphericity of the impacting drops, while it does not take place if the drop is oblate (with the present impact parameters).

Double drop impacts onto a deep pool

Double drop impacts onto a deep pool have been for the first time observed and described. The phenomena arising are characterized by several kinds of interaction, which have been described and discussed. The two craters or the two jets ejected from the craters may merge each other. New complex hollow shapes may be originated and a new mechanism of bubble entrapment has been reported. The crater merging seems to be energy consuming and if it takes place in the early growing phase of the craters, it prevents the formation of jets from the two original craters and the final crater only originates a slow large bump. If the crater merging takes place later, the two original craters have time to eject a jet from their center. The two jets are initially not vertical, but convergent or divergent.

Test case

The new symmetry of the velocity field generated by a simultaneous double drop impact has been accurately described also because of its importance in numerical studies. A drop impact represents a unsteady free surface flow governed by inertial, gravitational, viscous and surface tension effects. A simultaneous double drop impact has the additional complexity to have a three-dimensional velocity field, in comparison with the axial symmetric velocity field generated by a single drop impact. Mo-

reover a simultaneous double drop impact has the advantage to have two planes of symmetry, which allow a reduction of the computational time of a related numerical simulation. For this reason a case of double drop impact has been chosen as a challenging test case and has been recorded from four different points of view, in a way to give an accurate description of the evolution of the impact.

Single drop impacts onto a thick film

The influence of the film thickness has been investigated in comparison with single drop impacts onto a deep pool, with particular attention on the crater evolution. The presence of the wall reduces the velocity of penetration of the crater, but it does not significatively change the maximum depth, which is only reached later. For this reason the maximum crater depth of a deep pool impact has been chosen as reference parameter for the classification of the target liquid layers in thin films, thick films and deep pools. This choice has the advantage to account for the kinetic energy of the impacting drop instead of only its diameter as usual. The disadvantage is that the maximum crater depth of the deep pool impact is not known a priori, however it can be predicted using the new model developed in the present study.

Dynamics of the crater evolution

An experimental and analytical investigation of the crater formed by the impact of a drop onto a deep liquid pool at sufficiently high Weber, Froude and Reynolds numbers has been presented. The evolution of the crater for different impact parameters has been intensively studied and measured. Image processing has shown the shape of the crater to be similar to a portion of a sphere in the region far from the unperturbed water level, where the edge becomes almost vertical. Potential flow theory has been used to model the flow around the crater as the field given by a moving expanding sphere, whose equations of motion have been obtained through a balance of stresses at the crater interface and include the effects of inertia, gravity, surface tension and viscosity. Agreement with experimental data from the present study and from literature is rather good for the crater depth. The proposed approach can be potentially used for the description of multiple drop impacts, drop impacts onto a liquid layer of finite thickness, as well as for the description of the convective heat transfer in the cases of non-isothermal drop impacts. A map of the maximum crater depth as a function of the Froude and Weber numbers has been produced, which can be used to classify the depth of the liquid targets of single drop impacts, as explained in the previous paragraph.

The field of drop impacts is so wide and with so many connections that, even if a great number of studies are already present in literature, there are still some aspects that would need further investigations.

Physical mechanisms

Possible future studies could focus on some physical mechanism not completely clear yet. One could be the very early stage of drop impact onto a deep pool, with two possible targets: the prompt splashing and the creation of the crater. A detailed description of the setting up of the prompt splashing would be necessary to understand and to describe mathematically the instability mechanism. A detailed description of the first phase of creation of the crater and of the evolution of the impacting drop would be necessary to formulate completely analytical initial conditions for the analytical model on the evolution of the crater developed in the present study.

Extension of the analytical model

The analytical model could also be extended to include the influence of a finite thickness of the target liquid layer or to include the interaction of multiple drop impacts. The presence of a wall can be modeled with a superposition of two identic but symmetric potential, as shown in Figure 94, where the expression Equation 6.13 has been used, with arbitrary values of the parameters. Obviously, due to the potential theory, the no slip boundary condition on the wall is in this way respected only at the stagnation point on the symmetry axis. The superposition adds however some complications to the model, since the direct correspondence between the potential and the shape of the virtual object, whose movement causes the velocity field given by the potential, is lost, as represented in Figure 95. In other words the Equation 6.14 are not known a priori. Moreover the similarity of the shape of the crater with a sphere could be no more always valid and additional degrees of freedom may be required.

Further investigations on the double drop impacts may allow to draw a regime map, to find the limit of crater merging or to understand its mechanism, including that of the bubble entrapment described in Section 4.3. Other suggestions for possible studies derive from some experimental observations of the present study. Figure 96 shows the crater during the very early stage of ejection of a jet from its bottom. The case is related to a single drop impact onto a thick film, but a similar behavior has been observed also for impacts onto a deep pool. It has been highlighted the first hint of the jet. The formation of the jet with relative inversion of the shape of the crater does not seem to depend from capillary effects. They probably sustain the ejection in a later time, due to the high curvature which is produced.

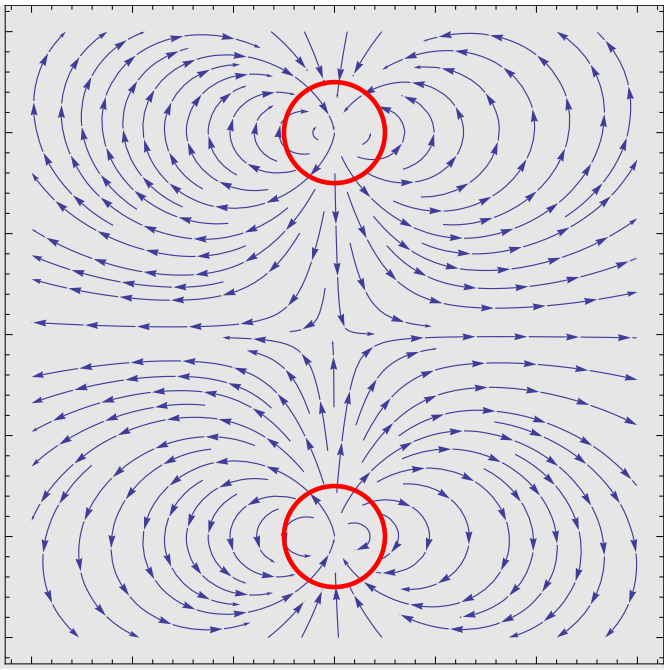

Figure 94: Velocity field generated by the superposition of two symmetric potentials of the type given in Equation 6.13, with arbitrary values of the parameters. The two circles are only indicative, since, due to the superposition, the correspondence between the expression of the potential and the flow generated by a moving expanding sphere is lost.

However the mechanism should be further investigate and clarified. Figure 97 shows the collapsing phase of a jet produced by the crater. During the last phase, when the top of the crater has reached the target liquid surface, a small droplet is ejected vertically with a great velocity. Probably during the downfall of the jet a droplet is pinched out at its top and it impacts onto the pool with subsequent ejection of a small droplet, but a further investigation would be necessary to clarify the phenomenon.

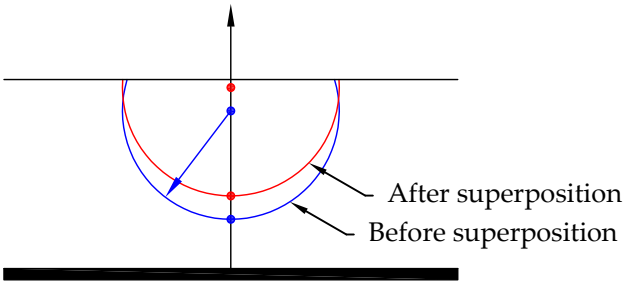

Figure 95: Sketch of the effect of a superposition of two symmetric potentials of the type given in Equation 6.13. The crater surfaces before and after the superposition do not coincide.

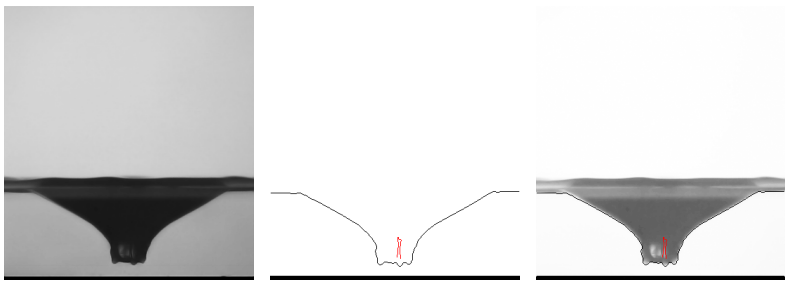

(a) (b) (c)

Figure 96: Very early stage of jet ejection. The case refers to a single impact onto a thick film in the tuning regime, but a similar mechanism has been observed for drop impacts onto a deep pool.

(a) $\tau = 72.38$ (b) $\tau = 83.34$ (c) $\tau = 91.31$

(d) $\tau = 94.30$ (e) $\tau = 100.28$ (f) $\tau = 106.25$

Figure 97: Micro drop fast ejection from a falling Worthington jet. (Water, $D = 2.2\,\mathrm{mm}$, $V = 2.8\,\mathrm{m/s}$, $We = 232$, $Fr = 350$, $Re = 7601$, $\tilde{H} = 1.8$).

BIBLIOGRAPHY

Wonder and charm of the splash. *The New York Times*, 1908. (Cited on page 4.)

A. Antowiak, N. Bremond, S. Le Dizès, and E. Villermaux. Short-term dynamics of a density interface following an impact. *J. Fluid Mech.*, 577:241–250, 2007. (Cited on page 60.)

H. Aryafar and H.P. Kavehpour. Drop coalescence through planar surfaces. *Phys. Fluids*, 18, 2006. (Cited on page 46.)

G.K. Batchelor. *An introduction to fluid dynamics*. Cambridge university press, 1967. (Cited on page 129.)

E. Berberovic, N.P. Van Hinsberg, S. Jakirlic, I.V. Roisman, and C. Tropea. Drop impact onto a liquid layer of finite thickness: Dynamics of the cavity evolution. *Phys. Rev. E*, 79(3):036306, 2009. (Cited on pages 101, 121, 130, 135, and 136.)

R. Bergmann, D. Van Der Meer, S. Gekle, A. Van Der Bos, and D. Lohse. Controlled impact of a disk on a water surface: cavity dynamics. *Journal of Fluid Mechanics*, 633, 2009. (Cited on page 60.)

G. Birkhoff, D.P. MacDougall, E.M. Pugh, and G.J. Taylor. Explosives with lined cavities. *Appl. Phys.*, 19:563, 1948. (Cited on pages 121 and 130.)

D.C. Blanchard and A.H.Woodcock. Bubble formation and modification in the sea and its meteorological significance. *Tellus*, 9(2), 1957. (Cited on page 48.)

F. Blanchette and T. Bigioni. Partial coalescence of drops at liquid interfaces. *Nature Physics*, 2, 2006. (Cited on page 46.)

C.V. Boys. Drops and splahes. *Nature*, 78(2035), 1908. (Cited on page 4.)

M.P. Brenner. Jets from a singular surface. *Nature*, 403, 2000. (Cited on page 53.)

D. Brutin. Drop impingement on a deep liquid surface: study of a crater's sinking dynamics. *C. R. Mecanique*, 331:61–67, 2003. (Cited on page 119.)

J.W.M. Bush. Surface tension module. *MIT Department of Mathematics*. (Cited on page 20.)

N.C. Byrnside and P.J. Torvick. The effect of projectile strength on crater formation. Technical report, AFML-TR-70-309, 1971. (Cited on page 115.)

Y.K. Cai. Collision of water drop on water. *Acta Mech. Sin.*, 4(4), 1988. (Cited on page 119.)

Y.K. Cai. Phenomena of a liquid drop falling to a liquid surface. *Exp. Fluids*, 7:388–394, 1989. (Cited on page 119.)

S. Chandrasekhar. *Hydrodynamic and hydromagnetic stability*. Dover Publications, 1981. (Cited on page 14.)

D.S. Chapman and P.R. Critchlow. Formation of vortex rings from falling drops. *J. Fluid Mech.*, 29:177–185, 1967. (Cited on pages 49 and 51.)

G.E. Charles and S.G. Mason. The coalescence of liquid drops with flat liquid/liquid interfaces. *J. Colloid Sci.*, 15:236–267, 1960a. (Cited on page 45.)

G.E. Charles and S.G. Mason. The mechanism of partial coalescence of liquid drops at liquid/liquid interfaces. *J. Colloid Sci.*, 15(2):105–122, 1960b. (Cited on page 45.)

D. Cole. *The splashing morphology of liquid-liquid impacts*. PhD thesis, James Cook University, 2007. (Cited on pages 44, 53, 60, 126, and 128.)

J. Conrad. Depth of field in depht. Large Format Photography, 2004. (Cited on page 26.)

G.E. Cossali, A. Coghe, and M. Marengo. The impact of a single drop on a wetted solid surface. *Experiments in Fluids*, 22, 1997. (Cited on page 55.)

G.E. Cossali, M. Marengo, and M. Santini. Multiple drop impact on heated surface. In *9th International Conference Liquid Atomization and Spray Systems ICLASS 2003, Sorrento, Italy*, 2003. (Cited on pages 71 and 79.)

G.E. Cossali, M. Marengo, and M. Santini. Drop array impacts on heated surfaces: secondary atomization characteristics. In *19th Annual Conference on Liquid Atomization and Spray Systems ILASS-Europe 2004, Nottingham, UK*, 2004a. (Cited on pages 71 and 79.)

G.E. Cossali, M. Marengo, and M. Santini. Impact of single and multiple drop array on liquid film. In *19th Annual Conference on Liquid Atomization and Spray Systems ILASS-Europe 2004, Nottingham, UK*, 2004b. (Cited on pages 71 and 79.)

G.E. Cossali, M. Marengo, and M. Santini. Effects of wall effusivity on secondary droplet atomisation from single and multiple drop impact onto heated surfaces. In *20th Annual Conference on Liquid Atomization and Spray Systems ILASS-Europe 2005, Orléans, France*, 2005. (Cited on pages 71 and 79.)

G.E. Cossali, M. Marengo, and M. Santini. Splashing characteristics of multiple and single drop impacts onto a thin liquid film. In *6th International Conference on Multiphase Flow, Leipzig, Germany*, 2007. (Cited on pages 71 and 79.)

C. Craeye and P. Schlussel. Rainfall on the sea: surface renewals and wave damping. *Boundary-Layer Meteorology*, 89:349–355, 1998. (Cited on page 5.)

R.W. Cresswell. Drop-formed vortex rings - the generation of vorticity. *Phys. Fluids*, 7(6), 1995. (Cited on page 49.)

R.M. Davies and G.I. Taylor. The mechanics of large bubbles rising through liquids in tubes. *Proc. R. Soc. Lond. A*, 200:375–390, 1950. (Cited on page 129.)

R.D. Deegan, P. Brunet, and J. Eggers. Complexities of splashing. *Nonlinearity 21 (2008) C1-C11*, 21:C1–C11, 2008. (Cited on page 55.)

Q. Deng, A.V. Anilkumar, and T.G. Wang. The role of viscosity and surface tension in bubble entrapment during drop impact onto a deep liquid pool. *J. Fluid Mech.*, 578:119–138, 2007. (Cited on pages 51 and 53.)

Q. Deng, A.V. Anilkumar, and T.G. Wang. The phenomenon of bubble entrapment during capsule formation. *Journal of Colloid and Interface Science*, 333:523–532, 2009. (Cited on page 5.)

P. Di Marco and R. Di Gaetano. Experimental investigation on the interaction between a rising gas bubble and a free surface. In *XXVI Congresso Nazionale UIT sulla trasmissione del calore*, 2008. (Cited on page 21.)

A.N. Dingle and Y. Lee. Terminal fallspeeds of raindrops. *J. App. Met.*, 11, 1972. (Cited on page 59.)

F. Durst. Penetration length and diameter development of vortex rings generated by impacting water drops. *Experiments in Fluids*, 21(2), 1996. (Cited on page 49.)

H.E. Edgerton and J.R. Killian. *Flash! Seeing the Unseen by Ultra-High-Speed Photography*. Branford, 1954. (Cited on page 4.)

W.D. Ellison. Studies of raindrop erosion. *Agricultural Engineering*, 25:131–136, 1944. (Cited on page 5.)

P.A. Elmore, G.L. Chahine, and H.N. Oguz. Cavity and flow measurements of reproducible bubble entrainment following drop impacts. *Exp. Fluids*, 31:664–673, 2001. (Cited on pages 7, 51, and 119.)

O.G. Engel. Collisions of liquid drops with liquids. Technical report, U.S. Nat. Bur. Standards, 1962. (Cited on page 116.)

O.G. Engel. Crater depth in fluid impacts. *J. Appl. Phys.*, 37(4): 1798–1808, 1966. (Cited on pages 59, 116, 117, 118, 119, 128, 135, and 136.)

O.G. Engel. Initial pressure, initial flow velocity and time dependence of crater depth in fluid impacts. *J. Appl. Phys.*, 38(10): 3935–3940, 1967. (Cited on pages 120, 121, and 135.)

L. Esmailizadeh and R. Mesler. Bubble entrainment with drops. *J. Colloid Interface Sci.*, 110:561–574, 1986. (Cited on page 48.)

A.I. Fedorchenko and A.B. Wang. On some common features of drop impact on liquid surfaces. *Phys. Fluids*, 16(5):1349–1365, 2004. (Cited on pages 44, 53, 101, 117, 119, 121, 130, 135, and 136.)

B. Fitt and M. Shaw. Transports of blight. *New Scientist*, 12:25–27, 1989. (Cited on page 5.)

G.J. Franz. Splashes as source of sound in liquids. *J. Acoust. Soc. Am.*, 31:1080–1096, 1959. (Cited on pages 50, 59, and 116.)

D.E. Gault and H.J. Moore. Scaling relationship for microscale to megascale impact craters. *Proc. 7th Hypervelocity Impact Symp.*, 1965. (Cited on pages 5, 115, and 121.)

H. Ghadiri. Crater formation in soils by raindrop impacts. *Earth Surf. Process. Landforms*, 29:77–89, 2004. (Cited on page 5.)

T. Gilet and J.W. Bush. The fluid trampoline: droplets bouncing on a soap film. *Journal Of Fluid Mechanics*, 625:167–203, 2009. (Cited on pages 46 and 60.)

T. Gilet, K. Mulleners, J.P. Lecomte, N. Vandewalle, and S. Dorbolo. Critical parameters for the partial coalescence of a droplet. *Phys. Review E*, 75, 2007. (Cited on page 46.)

R.C. Gonzalez. *Digital Image Processing Using MATLAB*. Prentice Hall, 2003. (Cited on page 36.)

R. Gunn and G.D. Kinzer. The terminal velocity of fall for water droplets in stagnant air. *J. Meteor.*, 6:243–248, 1949. (Cited on page 59.)

W. Hall, C. Maxwell, and P.V. Hobbs. Splashing of drops on shallow liquids. *Science*, 160(3830), 1968. (Cited on page 99.)

J. Hallett and L.R. Christensen. Splash and penetration of drops in water. *J. de Rech. Atmos*, 18(4):225–242, 1984. (Cited on pages 51, 59, and 60.)

P.V. Hobbs and T. Osheroff. Splashing of drops on shallow liquids. *Science*, 158(3805):1184–1186, 1967. (Cited on page 99.)

B. Holfeld, F. Maier, M. Izzo, and S. Dinardo. Spatial high-speed-imaging of projectile impacts into fluids in microgravity. *Microgravity Science and Technology*, 1-2(73–77), 2008. (Cited on page 60.)

K.A. Holsapple and R.M. Schmidt. Point source solutions and coupling parameters in cratering mechanics. *J. Geoph. Res.*, 92 (B7):6350–6376, 1987. (Cited on page 121.)

E.M. Honey and H.P. Kavehpour. Astonishing life of a coalescing drop on a free surface. *Phys. Rew. E*, 73, 2006. (Cited on page 46.)

O.W. Jayaratne and B.J. Mason. The coalescence and bouncing of water drops at an air/water interface. *Proceedings of the Royal Society of London. Series A, Mathematical and Physical Sciences*, 280(1383):545–565, 1964. (Cited on pages 46 and 60.)

D.C. Jenkins. An experimental method for studying the high speed impact of a liquid drop on a liquid surface. *Ingenieur-Archiv*, 36(4):280–284, 1967. (Cited on page 60.)

D.D. Joseph. Rise velocity of a spherical bubble. *J. Fluid Mech.*, 488:213–223, 2003. (Cited on page 129.)

R. Kinslow, V. Sahai, and J. Peddieson Jr. Preliminary investigation of high-velocity liquid impact damage. Technical report, 1972. (Cited on page 115.)

H. Lamb. *Hydrodynamics*. Dover Pubblications, 1932. (Cited on page 128.)

J.D. Laws. Measurement of the fall velocity of water drops and raindrops. *Trans. Amer. Geophys. Union*, 22(709–721), 1941. (Cited on page 59.)

E.R. Lee. *Microdrop generation*. CRC Press, 2002. (Cited on page 14.)

G. Leneweit, R. Koehler, K.G. Roesner, and G. Schäfer. Regimes of drop morphology in oblique impact on deep fluids. *J. Fluid Mech.*, 543:303–331, 2005. (Cited on page 60.)

J.L. Liow. Splash formation by spherical drops. *J. Fluid Mech.*, 427:73–105, 2001. (Cited on pages 44, 51, 53, 57, 117, and 121.)

J.L. Liow, W.H.R. Dickinson, M.J. Allan, and N.B. Gray. Study of slopping and splashing in a cylindrical bath with top-submerged injection. *Metallurgical and Materials Transactions B*, 26(B):887–889, 1994. (Cited on page 5.)

M.S. Longuet-Higgins. An analytic model of sound production by raindrops. *J. Fluid Mech.*, 214:395–410, 1990. (Cited on page 51.)

W.C. Macklin and P.V. Hobbs. Subsurface phenomena and the splashing of drops on shallow liquids. *Science*, 166(3901):3963–3970, 1969. (Cited on page 99.)

W.C. Macklin and G.J. Metaxas. Splashing of drops on liquid layers. *J. Appl. Phys.*, 47(9):3963–3970, 1976. (Cited on pages 100 and 117.)

L. Mahajan. The effect of the surrounding medium on the life of liquid drops floating on the same liquid surface. *Phil. Mag*, 10, 1930. (Cited on page 45.)

G. Mancino. Progettazione e realizzazione di un generatore di gocce multiple sincronizzate e studio morfologico dell'impatto su superficie calda. Master's thesis, Università degli studi di Bergamo, 2002. (Cited on page 16.)

S.L. Manzello and J.C. Yang. An experimental study of a water droplet impinging on a liquid surface. *Experiments in Fluids*, 32(5):580–589, 2002. (Cited on pages 5, 60, and 100.)

J.E. Field M.B. Lesser. The impact of compressible liquids. *Annu. Rev. Fluid Mech.*, 15:97–122, 1983. (Cited on page 43.)

V. Mehdi-Nejad, J. Mostaghimi, and S. Chandra. Air bubble entrapment under a impacting droplet. *Physics of Fluid*, 15(1): 173–183, 2003. (Cited on page 5.)

L.A. Merzhievsky. Crater formation in a plastic target under hypervelocity impact. *Int. J. Impact Eng.*, 20:557–568, 1997. (Cited on page 121.)

H.J. Moore, D.E. Gault, and R.W. MacCormack. Fluid impact craters and hypervelocity - high velocity impact experiments in metals and rocks. Technical report, U.S. Depart. of the Int. Geol. Surv., 1962. (Cited on page 116.)

B.R. Morton and R.W. Cresswell. Raindrops in the sea 1: Generation of vorticity and vortex ring production. In MR Davis and GJ Walker, editors, *11th Australasian fluid mechanics conference*, volume 1–2, pages 611–614, 1992. (Cited on page 5.)

D. Morton, M. Rudman, and J.M. Liow. An investigation of the flow regimes resulting from splashing drops. *Phys. Fluids*, 12 (4), 2000. (Cited on pages 44, 51, and 128.)

C.K. Mutchler and L.M. Hansen. Splash of a waterdrop at terminal velocity. *Science*, 169:1311–1312, 1970. (Cited on page 59.)

G.P. Neitzel and P. Dell'Aversana. Noncoalescence and nonwetting behavior of liquids. *Annu. Rev. Fluid Mech.*, 34:267–289, 2002. (Cited on page 45.)

H.N. Oguz and A. Prosperetti. Surface-tension effects in the contact of liquid surfaces. *J. Fluid Mech.*, 203:149–171, 1989. (Cited on page 49.)

H.N. Oguz and A. Prosperetti. Bubble entrainment by the impact of drops on liquid surfaces. *J. Fluid Mech.*, 219:143–179, 1990. (Cited on pages 50, 116, and 121.)

T. Okawa, T. Shiraishi, and T. Mori. Effect of impingement angle on the outcome of single water drop impact onto a plane water surface. *Exp. Fluids*, pages 331–339, 2008. (Cited on page 60.)

K.L.R. Olevson. Energy balances for transient water craters. *US Geol. Surv. Res.*, pages D189–D194, 1969. (Cited on page 119.)

E.J. Opik. Researches on the physical theory of meteor phenomena: I. theory of the formation of meteor craters. *Publ. Astron. Obs. Tartu*, 1937. (Cited on page 115.)

B. Peck and L. Sigurdson. The three-dimensional vortex structure of an impacting water drop. *Phys. Fluids*, 6(1), 1994. (Cited on page 48.)

D.H. Peregrine. *J. Fluid Mech.*, 106(59), 1981. (Cited on page 55.)

P. Pikhitsa and A. Tsargorodskaya. Possible mechanism for multistage coalescence of a floating droplet on the air/liquid interface. *Colloids and Surfaces A*, 167:287–291, 2000. (Cited on page 46.)

V. Pratt. Direct least-squares fitting of algebraic surfaces. *ACM SIGGRAPH Comput. Graph.*, 21(4):145–152, 1987. (Cited on pages 124 and 126.)

W.K. Pratt. *Digital image processing*. John Wiley & Sons, 1991. (Cited on page 36.)

A. Prosperetti and H.N. Oguz. The impact of drops on liquid surfaces and the underwater noise of rain. *Annu. Rev. Fluid Mech.*, 25:577–602, 1993. (Cited on pages 5, 43, 50, 116, and 117.)

A. Prosperetti, H.C. Pumprey, and L.A. Crum. The underwater noise of rain. *J. Geophys. Res.*, 94:3255–3259, 1989. (Cited on page 116.)

H.C. Pumphrey and P.A. Elmore. The entrainment of bubbles by drop impacts. *J. Fluid Mech.*, 220:539–527, 1990. (Cited on pages 57, 116, and 117.)

H.C. Pumphrey and A.J. Walton. Experimental study of the sound emitted by water drops impacting on a water surface. *European Journal of Physics*, 1988. (Cited on page 50.)

H.C. Pumphrey, L.A. Crum, and L. Bjorno. Underwater sound produced by individual drop impacts and rainfall. *J. Acoust. Soc. Am.*, 85:1518–1526, 1989. (Cited on pages 50 and 116.)

Lord Rayleigh. In *Proc. R. Soc. London*, volume 29, 1879. (Cited on page 45.)

Lord Rayleigh. Further observations upon liquid jets. In *Proc. R. Soc. London*, volume 34, 1882. (Cited on page 45.)

Lord Rayleigh. On the tension of recently formed liquid surfaces. *Proc. R. Soc. Lond.*, 47:281–287, 1890. (Cited on page 60.)

M. Rein. Phenomena of liquid drop impact on solid and liquid surfaces. *Fluid Dyn. Res.*, 12:61–93, 1993. (Cited on page 43.)

M. Rein. The transitional regime between coalescing and splashing drops. *J. Fluid Mech.*, 306:145–165, 1996. (Cited on pages 44, 51, and 53.)

O. Reynolds. On the action of rain to calm the sea. In *Proc. Manchester Literary and Philosophical Society*, volume 14, pages 72–74, 1875. (Cited on pages 2 and 5.)

O. Reynolds. On the floating of drops on the surface of water depending only on the purity of the surface. In *Proc. Manchester Literary and Philosophical Society*, volume 21, pages 1–2, 1881. (Cited on pages 2 and 45.)

F. Rodriguez and R. Mesler. Some drops don't splash. *J. Colloid Interface Sci.*, 106(2):347–352, 1985. (Cited on pages 44 and 53.)

W.B. Rogers. On the formation of rotating rings by air and liquids under certain conditions of discharge. *Amer. J. Sci.*, Second Ser 26::246–258, 1858. (Cited on page 49.)

I.V. Roisman. Inertia dominated drop collisions. II. an analytical solution of the navier-stokes equations for a spreading viscous film. *Physics of fluid*, 2009. (Cited on page 8.)

I.V. Roisman and C. Tropea. Impact of a drop onto a wetted wall: description of crown formation and propagation. *J. Fluid Mech.*, 472:373–397, 2002. (Cited on pages 55 and 101.)

I.V. Roisman, B. Prunet-Foch, C. Tropea, and M. Vignes-Adler. Multiple drop impact onto a dry solid substrate. *Journal of Colloid and Interface Science*, 256(2):396–410, 2002. (Cited on page 71.)

I.V. Roisman, N.P. Van Hinsberg, and C. Tropea. Propagation of a kinematic instability in a liquid layer: Capillary and gravity effects. *Physical Review E*, 77(4):1–7, 2008. (Cited on page 101.)

K. Shariff and A. Leonard. Vortex rings. *Annu. Rev. Fluid Mech.*, 24:235–279, 1992. (Cited on page 49.)

J. Shin and T.A. McMahon. The tuning of a splash. *Physics of Fluids A*, 2(8):1312–1317, 1990. (Cited on pages 57, 100, 102, and 108.)

J. Sigler and R. Mesler. The behavior of the gas film formed upon drop impact with a liquid surface. *Journal of Colloid and Interface Science*, 134(2):459–474, 1990. (Cited on page 49.)

S. Sikalo and E.N. Ganic. Phenomena of droplet-surface interactions. *Experimental Thermal and Fluid Science*, 31:97–110, 2006. (Cited on page 43.)

D. Sivakumar and C. Tropea. Splashing impact of a spray onto a liquid film. *Phys Fluids*, 14(12):L85–L88, 2002. (Cited on page 5.)

D.E. Snyder. Characteristics of sound radiation from large raindrops. Master's thesis, Naval Postgraduate School, Monterey, California, 1990. (Cited on page 59.)

A.F. Spilhaus. Raindrop size, shape and falling speed. *J. Meteor.*, 5:108–110, 1948. (Cited on page 59.)

J.J. Thomson and H.F. Newall. On the formation of vortex rings by drops falling into liquids and some allied phenomena. In *Proc. R. Soc. London*, volume 39, pages 417–436, 1885. (Cited on pages 2, 45, and 49.)

S.T. Thoroddsen. The ejecta sheet generated by the impact of a drop. *J. Fluid Mech.*, 451:373–381, 2002. (Cited on page 55.)

S.T. Thoroddsen and K. Takehara. The coalescence cascade of a drop. *Phys. Fluids*, 12(6), 2000. (Cited on pages 45 and 46.)

S.T. Thoroddsen, T.G. Etoh, and K. Takehara. Air entrapment under an impacting drop. *J. Fluid Mech.*, 478:125–134, 2003. (Cited on page 49.)

S.T. Thoroddsen, T.G. Etoh, and K. Takehara. High-speed imaging of drops and bubbles. *Annu. Rev. Fluid Mech.*, 40:257–285, 2008. (Cited on pages 24 and 43.)

Y. Tomita, T. Saito, and S. Ganbara. Surface breakup and air bubble formation by drop impact in the irregular entrainment region. *J. Fluid Mech.*, 588:131–152, 2007. (Cited on page 57.)

M.F. Trujillo and C.F. Lee. Modeling crown formation due to the splashing of a droplet. *Phys. Fluids*, 13, 2001. (Cited on page 55.)

E. Villermaux and B. Bossa. Single-drop fragmentation determines size distribution of raindrops. *Nature Physics*, 5:697–702, 2009. (Cited on pages 15 and 59.)

R.L. Vander Wal, G.M. Berger, and S.D. Mozes. Droplets splashing upon films of the same fluid of various depths. *Experiments in Fluids*, 40:33–52, 2006. (Cited on pages 100 and 101.)

D.A. Weiss and A.L. Yarin. Single drop impact onto liquid films: neck distortion, jetting, tiny bubble entrainment, and crown formation. *J. Fluid Mech.*, 385:229–254, 1999. (Cited on page 55.)

F.M. White. *Fluid Mechanics*. McGraw-Hill, 2002. (Cited on page 129.)

A.M. Worthington. On impact with a liquid surface. *Proceedings of the Royal Society of London*, 34:217–230, 1883. (Cited on page 2.)

A.M. Worthington. *A study of splashes*. Green and Co., 1908. (Cited on pages 4, 53, and 59.)

A.M. Worthington and R.S. Cole. Impact with a liquid surface, studied by the aid of instantaneous photography. *Philosophical Transactions of the Royal Society of London. Series A, Containing Papers of a Mathematical or Physical Character*, 189:137–148, 1897. (Cited on page 4.)

A.M. Worthington and R.S. Cole. Impact with a liquid surface, studied by the aid of instantaneous photography. paper ii. *Philosophical Transactions of the Royal Society of London. Series A, Containing Papers of a Mathematical or Physical Character*, 194: 175–199, 1900. (Cited on page 4.)

X.Chen, S.Mandre, and J.J. Feng. Partial coalescence between a drop and a liquidliquid interface. *Phys. Fluids*, 18(051705), 2006. (Cited on page 46.)

A.L. Yarin. Drop impact dynamics: splashing, spreading, receding, bouncing... *Annu. Rev. Fluid Mech.*, 38:159–192, 2006. (Cited on pages 43 and 55.)

A.L. Yarin and D.A. Weiss. Impact of drops on solid surfaces: self-similar capillary waves, and splashing as a new type of kinematic discontinuity. *Journal of Fluid Mechanics*, 283:141–173, 1995. (Cited on pages 8, 14, 55, and 101.)

A.L. Yarin, M.B. Rubin, and I.V. Roisman. Penetration of a rigid projectile into an elastic-plastic target of finite thickness. *Int. J. Impact Eng.*, 16:801–831, 1995. (Cited on pages 121 and 130.)

B.W. Zeff, B. Kleber, J. Fineberg, and D.P. Lathrop. Singularity dynamics in curvature collapse and jet eruption on a fluid surface. *Nature*, 403, 2000. (Cited on page 53.)

X. Zhang and O.A. Basaranb. An experimental study of dynamics of drop formation. *Phys. Fluids*, 7(5), 1995. (Cited on page 13.)